AUG 12 2004

REPORT DOCUMENTATION PAGE

Form Approved
OMB No. 0704-0188

1. AGENCY USE ONLY *(Leave blank)*	2. REPORT DATE	3. REPORT TYPE AND DATES COVERED
	11.Aug.04	DISSERTATION

4. TITLE AND SUBTITLE
RESPONSE OF THE IONOSPHERE AND THERMOSPHERE TO EXTREME
SOLAR CONDITIONS

5. FUNDING NUMBERS

6. AUTHOR(S)
MAJ SMITHTRO CHRISTOPHER G

7. PERFORMING ORGANIZATION NAME(S) AND ADDRESS(ES)
UTAH STATE UNIVERSITY

**8. PERFORMING ORGANIZATION
REPORT NUMBER**

CI04-583

9. SPONSORING/MONITORING AGENCY NAME(S) AND ADDRESS(ES)
THE DEPARTMENT OF THE AIR FORCE
AFIT/CIA, BLDG 125
2950 P STREET
WPAFB OH 45433

**10. SPONSORING/MONITORING
AGENCY REPORT NUMBER**

11. SUPPLEMENTARY NOTES

12a. DISTRIBUTION AVAILABILITY STATEMENT
Unlimited distribution
In Accordance With AFI 35-205/AFIT Sup 1

DISTRIBUTION STATEMENT A
Approved for Public Release
Distribution Unlimited

12b. DISTRIBUTION CODE

13. ABSTRACT *(Maximum 200 words)*

20040820 040

14. SUBJECT TERMS

15. NUMBER OF PAGES
132

16. PRICE CODE

17. SECURITY CLASSIFICATION OF REPORT	18. SECURITY CLASSIFICATION OF THIS PAGE	19. SECURITY CLASSIFICATION OF ABSTRACT	20. LIMITATION OF ABSTRACT

ABSTRACT

Response of the Ionosphere and Thermosphere

to Extreme Solar Conditions

by

Christopher G. Smithtro, Doctor of Philosophy

Utah State University, 2004

Major Professor: Dr. Jan J. Sojka
Department: Physics

From the sunspot record, we know the Sun underwent an extended period of extremely low activity from 1640-1710 A.D., known as the Maunder Minimum. Conversely, astronomers have observed "Sun-like" stars that exhibit much higher levels of activity. To explore the impact of such extreme solar input, we built a one-dimensional physical model of the coupled thermosphere and ionosphere. Results from this global average model were found to be in good agreement with other empirical models, as well as previous physical models. Extrapolating the solar irradiance to assumed Maunder Minimum levels, we found the ionosphere undergoes a dramatic change, in which NO^+ comes to dominate over O^+ in the F-region. Increasing the solar flux to exceptionally high levels revealed a plateau in the peak electron density, although the total electron content continued to rise.

(132 pages)

ACKNOWLEDGMENTS

Christopher G. Smithtro

CONTENTS

LIST OF TABLES

LIST OF FIGURES

CHAPTER 1

INTRODUCTION

1.1. Motivation

Our Sun exhibits a regular pattern of activity known as the solar cycle. This approximately 11-year cycle corresponds to a reversal in the Sun's dipole magnetic field. Sunspots, the only direct manifestation of this cycle visible to the naked eye, result from a concentrated eruption of magnetic flux through the solar photosphere. The increasing number of sunspots over the course of the cycle thus heralds the global restructuring of the Sun's dipole field.

Breaking through the photosphere, the emerging magnetic field lines reach high into the chromosphere and corona, confining plasma and affecting the local emission characteristics. As a consequence, the flux of ultraviolet photons, which originate primarily in the solar atmosphere, undergoes significant modulation over the course of the solar cycle. Other phenomena, such as the flux of 10.7 cm radio waves and the frequency of solar flares, are also related to the magnetic topology, and thus follow the same cyclic modulation. Contemporary observations and measurements of this variability define a range of normal solar activity.

An examination of the historical sunspot record reveals an extended period, between 1645 and 1715 A.D., during which time virtually no sunspots were observed. This period is now known as the Maunder Minimum. Independent evidence from studies of cosmogenic isotopes [*Eddy*, 1976; *Webber and Higbie*, 2003] and Sun-like stars [*Baliunas and Jastrow*, 1990; *Lean et al.*, 2001; *White et al.*, 1992] suggests solar activity during this period was markedly lower than contemporary levels. *Eddy* [1976] also used the cosmogenic isotope record to argue for a period of exceptionally high solar activity during the 12th and 13th centuries. Although the sunspot record during this era is too unreliable to provide supporting evidence, a survey of Sun-like stars confirms significantly higher levels of activity from our own Sun are indeed plausible [*Radick*,

2003; *Radick et al.*, 1998]. Together, the available evidence suggests the level of solar activity we have come to define as normal represents merely a subset of a much wider possible range.

It is important to point out although the Sun's ultraviolet emission undergoes strong modulation as a function of the activity level, energy output as a whole remains essentially constant. Photon flux in the ultraviolet wavelengths makes up a negligible fraction of the total energy output. Thus, at Earth, it is the thermosphere and ionosphere that show a strong solar cycle modulation, because this is where most of the highly-variable photons are absorbed. On the other hand, the lower atmosphere shows little or no solar cycle dependence.

The goal of this dissertation is to describe the response of the ionosphere and thermosphere to plausible extremes in the ultraviolet flux. What is needed to accurately investigate this question is a physical model of the ionosphere and thermosphere that realistically responds to a wide range of input solar irradiance.

1.2. Method

Over the past 50 years, physical models of the coupled thermosphere and ionosphere have evolved from simple analytic approximations into massive, 3-D general circulation models. However, simpler models still have their place. Because they require far less computer time, 1-D models can eliminate many of the parameterizations necessary to speed the 3-D versions, and are easily run on modern desktop computers. In fact, they continue to serve as test-beds for quickly comparing chemical schemes and the effects of updated rate coefficients [*Sharma and Roble*, 2001].

In this work, we will use a 1-D model to represent the global average thermosphere/ionosphere system. Averaging the photoabsorption rate over the entire globe, the effective solar irradiance is roughly 50% of the incident flux. The average solar heating is balanced by radiative cooling and other thermal processes contained within the single vertical

profile. The resulting temperature profile, in conjunction with the associated photodissociation and photoionization rates, then determines the structure of an idealized neutral thermosphere and coupled ionosphere. *Roble et al.* [1987] showed such an approach can be used to accurately represent the global behavior of the upper atmosphere under normal solar conditions.

The global average model obviously neglects horizontal structure. Instead, it represents a climatological view of the total system. An understanding of the model's strengths and weaknesses is therefore crucial. The situation is analogous to empirical models of the thermosphere and ionosphere. These empirical models are useless when it comes to predicting high-resolution variability due to space weather, but ideal for generating climatology at a given location. In the same manner, a global average model cannot answer questions involving horizontal or diurnal structure, but does provide a physically realistic picture of how an idealized atmosphere responds to solar input. Sophisticated 3-D models provide a more complete picture, but are much more complex, have exponentially greater computational requirements, and are more difficult to interpret. The work we present here is speculative, involving hypothetical solar spectra that have never been measured. Full 3-D general circulation models are therefore not warranted, whereas 1-D global average models are ideally suited to the task.

Building on the pioneering work of Roble and others [*Roble*, 1995; *Roble and Emery*, 1983; *Roble et al.*, 1987], we build a new Global Average Ionosphere/Thermosphere (GAIT) model that describes the average state of the atmosphere, from the mesopause to upper thermospheric heights. The model self-consistently solves the coupled continuity and momentum equations for 12 neutral and 7 ion species. Energy equations are solved for the neutral, ion, and electron gas temperatures. The globally averaged solar irradiance is used to specify the various photodissociation and photoionization rates, which, along with the relevant chemical reactions, determine the heat input and thus drives the solution.

The primary goal of this effort is to create a model that can be used to explore the upper atmosphere's behavior, in response to irradiance inputs outside the normal solar cycle variation. Toward this end, the GAIT model is largely independent of a specific solar irradiance representation. For example, rather than using volume heating rates parameterized by a solar proxy, we directly account for the photons between 3-360 nm using a solar irradiance model. The GAIT model also includes an approximate treatment of photoelectrons, rather than relying on simple scale factors of secondary ionization or parameterizations of the thermal electron volume heating rate.

Chapter 2 of this dissertation gives an introduction to the coupled thermosphere/ionosphere system, with particular emphasis on the global energy budget. In Chapter 3 we go on to describe the GAIT model in detail, introducing the model equations, as well as the component processes that fuel the energy budget. The next chapter compares representative output from the GAIT model to the *Roble et al.* [1987] work, as well as the Mass Spectrometer Incoherent Scatter (MSIS-90) empirical model [*Hedin*, 1991]. Chapter 5 examines the model's sensitivity to uncertainties in key reaction rates and inputs that directly affect the global energy budget. Leveraging the GAIT model's sensitivity to the input solar spectrum, we also explore its response to four different solar irradiance models.

Chapters 6 and 7 represent the real meat of this dissertation; they explore the response of the coupled thermosphere and ionosphere to extreme solar input. In Chapter 6 we justify a reconstructed Maunder Minimum spectrum, and consider the impact as solar flux levels approach this assumed lower limit. We will find the ionosphere undergoes an interesting transition at solar flux levels not much lower than normal solar minimum. Chapter 7 deals with the opposite case, extremely high solar flux levels. The input solar irradiance is increased by an amount equal to six times the normal cycle variation. In this case, the resulting ionosphere deviates significantly from what might be expected by simple extrapolation.

CHAPTER 2

BACKGROUND

Above the well-mixed homosphere, where gravity begins to separate the neutral species by mass, lies the thermosphere. The thermosphere extends from roughly 95 to 500 km, depending on the stage of the solar cycle; above ~500 km collisions are so few neutrals begin to behave like ballistic particles, defining the transition to the exosphere [*Schunk and Nagy*, 2000]. At the base of the thermosphere, known as the mesopause, temperatures are approximately 180 K, the coldest in the atmosphere. Above this level, the neutral gas temperature rises quickly with altitude and becomes constant as thermal conduction dominates over local sources and sinks. Concentrations of N_2 and O_2, the major constituents of the homosphere, continue to drop exponentially with altitude in the thermosphere, characterized primarily by a diffusive equilibrium profile. However, photodissociation of the molecular species is also important, resulting in significant amounts of atomic oxygen and nitrogen. Above 120 km, atomic oxygen also roughly follows a diffusive equilibrium profile, and given its lower mass, quickly becomes the dominant neutral species. The altitude structure of the neutral thermosphere therefore depends primarily on the constituent scale heights, which goes as the neutral gas temperature.

Within the thermosphere also lies a plasma environment called the ionosphere, which is dominated by molecular ions at low altitudes and atomic ions at higher altitudes. The ionosphere is often viewed as being superimposed on and separate from the underlying neutral thermosphere; in fact, it is central to the thermospheric heat budget. Above approximately 250 km, elastic collisions between neutrals and ions act as the dominant neutral heat source. And nitric oxide, which originates primarily through ionic chemistry, in turn becomes an important source of cooling in the middle thermosphere.

The inherent coupling between the thermosphere and ionosphere is obvious. The ionosphere is formed when energetic photons ionize the underlying neutral constituents. The structure of these same neutral species is intimately related to the neutral gas temperature. Yet the neutral gas energy budget depends on the interaction with the ionosphere. Therefore, in order to develop a self-consistent model of the thermosphere/ionosphere system, we must consider all of the coupled processes as well as various minor species important to the energy budget.

For convenience, when describing the solar input irradiance we roughly divide the ultraviolet spectral range into those wavelengths able to ionize the major neutral species (N_2, O_2, and O), and longer wavelengths that primarily dissociate O_2 and other minor molecular species. We label the ionizing wavelengths, 3-105 nm, as the EUV, and everything longward of 105 nm as simply UV. The hydrogen Lyman-alpha line at 121.6 nm is in fact able to ionize NO, but is more important for its role in O_2 photolysis.

Figure 1 shows a simplified schematic of solar energy flow in the thermosphere. The width of the arrows serves to indicate the relative amount of energy following each path; note however total energy in the UV vastly outweighs the EUV. Other heat sources such as particle precipitation, electric fields, and gravity waves are secondary to the primary solar input, and therefore neglected in the figure. For clarity, the schematic also simplifies a number of energy pathways, such as the redistribution of energy from thermal electrons to the neutrals via the ion gas. Yet overall, it provides a fairly good representation of the solar energy flow.

In the EUV, most of the absorbed photons result in ionization of the neutral; the excess energy going to the fast photoelectron. Assuming an average EUV photon energy of 30 eV, roughly 15 eV goes to production of the ion and the other 15 eV to the resulting photoelectron [*Roble*, 1995]. As indicated in Figure 1, photoelectrons lose energy through either Coulomb collisions with the ambient electron gas or inelastic collisions with neutrals. The Coulomb collisions result in about 1 eV of heating for electron gas, which is in turn transferred through
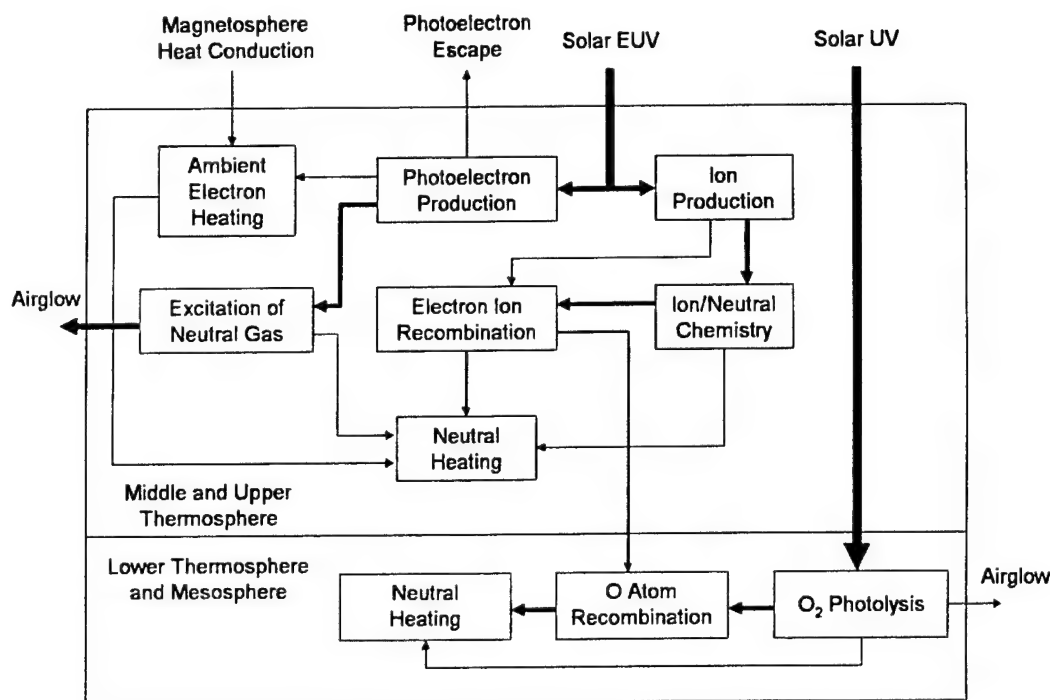
Figure 1. A simplified schematic illustrating the primary flow of solar energy in the thermosphere; adapted from *Stolarski* [1976] and *Roble* [1995]. The width of the arrows gives an indication to the relative amounts of energy involved.

collisions to the neutral gas. Inelastic collisions between photoelectrons and neutrals can result in additional ionization, recycling energy back through the schematic, or excite internal energy levels in the neutral. Some of this internal energy is converted into neutral gas heat through quenching collisions, however, most is radiated as airglow.

On the ion side of the schematic, energy is redistributed through a series of ion-neutral chemical reactions. During this process, the exothermic reactions transfer heat to the neutral gas, resulting in roughly 10 eV of total heating. In addition, every ion created ultimately results in the dissociation of O_2 into two O atoms [*Stolarski*, 1976]. So, of the initial 15 eV chemical energy in the ions, 10 eV goes directly to the neutral gas, while the remaining 5 eV is stored in the chemical energy of the O atoms. The O atoms must diffuse down to low altitudes, roughly 90 to 100 km, in order to undergo three-body recombination and release the final 5.12 eV of heat to the neutral

gas. Thus, virtually all of the energy that goes into forming the ion ultimately ends up as neutral heat; most in the middle thermosphere where the ion is formed, but some in the lower thermosphere and mesosphere where O recombines. In the photoelectron channel, however, only about 5% of the initial 15 eV goes to neutral heating [*Roble* 1995; *Stolarski*, 1976].

The path of energy for UV photons is much simpler. Given low photoabsorption cross sections, UV photons penetrate deep into the thermosphere. In fact, longward of 175 nm, the majority of photons pass through to the mesosphere. Dissociation of O_2 requires only 5.12 eV; sufficiently energetic photons can also excite the resulting atomic oxygen to the ^1D state, requiring an additional 1.97 eV. As indicated in Figure 1, the remaining energy goes directly to heating the neutral gas. As was the case in the EUV, some of the dissociation energy is recovered through three-body recombination of O. Quenching collisions with $O(^1D)$ add to the neutral heat, with the remainder lost via airglow. For wavelengths longer than 200 nm the photoabsorption cross sections are so small we can neglect dissociation of O_2 in the thermosphere; however, photolysis of ozone, O_3, continues to add a small contribution to the net heating rate up to about 360 nm.

Each branch of the energy flow schematic results in the production of excited states. Failure to account for the resulting airglow and chemiluminescent emission results in overestimation of the net heating rate [*Mlynczak and Solomon*, 1993]. For this reason thermospheric models must account for a number of metastable species such as $O(^1D)$, $O_2(^1\Delta_g)$, $O_2(^1\Sigma_g)$, which are produced during dissociation of O_2 and O_3.

Cooling in the thermosphere comes primarily from three radiative processes [*Gordiets et al.*, 1982; *Roble et al.*, 1987]. In the upper thermosphere 63 μm radiation from the fine structure of atomic oxygen constitutes the largest cooling mechanism [*Bates*, 1951]. In the lower thermosphere cooling by CO_2 at 15 μm dominates, accounting for over 80% of the total radiative energy loss. The 5.3 μm radiation from NO is important in the middle thermosphere (120-200

km) [*Kockarts*, 1980], especially at solar maximum when it contributes roughly 15% of the total radiative energy loss. A self-consistent calculation for the concentration of NO requires the inclusion of atomic nitrogen, both ground, $N(^4S)$, and metastable, $N(^2D)$, states, since reactions of N with O_2 act as the dominant source of NO.

This discussion has provided a general overview of the coupled thermosphere/ionosphere system, focusing particularly on the energy budget, which drives the entire system. In the next chapter we will describe the specific implementation of these processes in the GAIT model.

CHAPTER 3

GAIT MODEL DESCRIPTION

The GAIT model self-consistently solves the one-dimensional neutral, ion, and electron

energy equations, as well as the continuity and momentum equations for both neutral and ion

species. The lower boundary is set to an altitude of 95 km, while the upper boundary is varied

with the solar cycle to capture the topside F-region ionosphere. Beginning with arbitrary initial

conditions, the coupled equations are integrated forward in time until the system reaches a steady-

state, in ~20 days of integration time.

3.1. Neutral Gas Energy Equation

The familiar time-dependent, one-dimensional heat conduction equation is modified to

approximate the effects of turbulent mixing [*Gordiets et al.*, 1982; *Johnson and Gottlieb*, 1970],

$$C_p n \frac{\partial T}{\partial t} - \frac{\partial}{\partial z}\left(C_p n K_{eddy}\left(\frac{\partial T}{\partial z} + \Gamma \right) + \lambda \frac{\partial T}{\partial z} \right) = Q - L, \tag{1}$$

where T and n identify the neutral gas temperature and density, Γ the adiabatic lapse rate (~10

K/km), K_{eddy} the eddy diffusion coefficient, and z the altitude. C_p and λ refer to the specific heat

and thermal conductivity, averaged for a multi-species gas. Q and L are the heating and cooling

terms described further in sections 3.5 and 3.6. Thermal conductivity values are given by *Schunk*

and Nagy [2000].

The temperature at the model's lower boundary (95 km) is fixed at 177 K, based on a global

average obtained from the empirical Mass Spectrometer and Incoherent Scatter (MSIS-90) model

[*Hedin*, 1991]. (Flags in the MSIS-90 model permit us to turn off diurnal, longitude, and seasonal

effects. The global average is then calculated using 10-point Gaussian Quadrature over latitude.)

The model's lower boundary was chosen to coincide with the mesopause height, because here the

MSIS-90 global average temperature varies by less than 1% over the course of the solar cycle,

allowing us to use a single fixed boundary condition. At the upper boundary, we assume

thermal conductivity dominates, leading to the condition $\frac{\partial T}{\partial z} = 0$.

No standard formulation for the shape or magnitude of the eddy diffusion coefficient exists,

and it remains essentially a free parameter used to match model with observations in the

mesosphere and lower thermosphere. *Rodrigo et al.* [1986] gives examples of nine different

coefficient profiles that have been used in the literature. For the GAIT model we choose the

parameterization of *Roble et al.* [1987],

$$K_{eddy}(Z) = K^{max}\text{Exp}[-7 - Z].\tag{2}$$

A maximum value of 100 m^2 s^{-1} was selected in order to best match the modeled neutral density

profiles to MSIS-90 global average results. The independent variable Z is a log pressure

coordinate defined by *Roble et al.* [1987] as

$$Z = \text{Log}_e[P_o / P],\tag{3}$$

where P is the pressure, and the reference pressure P_o is 50 μPa. Although the model is built with

altitude as the vertical coordinate, many important processes are better expressed in pressure

coordinates. We therefore make extensive use of Z and will frequently present model output on

the same pressure scale.

3.2. Ion and Electron Energy Equations

For the parallel ion and electron temperatures, an equation similar to (1) applies,

$$C_p n \frac{\partial T}{\partial t} - \sin^2 I \frac{\partial}{\partial z}\left(\lambda \frac{\partial T}{\partial z}\right) = Q - L.\tag{4}$$

Because T_i and T_e are locked to T_n at low altitudes, we can neglect the eddy diffusion term

included in (1). Calculation of the thermal conductivities for both the ion and electron equations

are described in *Rees and Roble* [1975] and *Schunk and Nagy* [2000]. The magnetic dip angle, I,

determines the degree of conductivity in the vertical direction, but the physical interpretation of

this parameter is not well defined in a one-dimensional global average. For example, at the equator the dip angle is zero, resulting in no vertical conductivity, but horizontal transport, which is not possible in this 1-D model, compensates. *Roble et al.* [1987] assumed $I = 90$ degrees, corresponding to a polar condition in which the field lines are vertical. The GAIT model adopts a value of $I = 75$ degrees (co-latitude ~30 degrees) to reflect some deviation from a perfect vertical, but the resulting difference between the two values is small, producing less than a 4% change to the neutral gas exospheric temperature and total electron content, which are considered key scalar measures of the overall solution.

Ambient thermal electrons are heated by collisions with photoelectrons; earlier models have relied on the parameterization of *Swartz and Nisbet* [1972] to calculate the electron volume heating rate as a function of the total ionization rate. In the GAIT model, we have incorporated an approximate photoelectron solution and calculate the volume heating rate self-consistently (section 3.8). Thermal electrons lose energy through elastic and inelastic collisions with ions and neutrals; the cooling rates are determined using the expressions given by *Schunk* [1988], *Schunk and Nagy* [2000], and *Rees and Roble* [1975]. The same elastic electron-ion collisions that cool the electron gas act as a heat source for the ions; ions are also heated via exothermic chemical reactions. Ions transfer this heat through elastic collisions to the neutral gas [*Rees and Roble*, 1975].

At the lower boundary, both the electron and ion temperatures are set equal to the neutral temperature. At the upper boundary, a downward heat flux along magnetic field lines connected to the plasmasphere and magnetosphere is required to obtain a reasonable electron temperature profile. In their earlier global average model, *Roble et al.* [1987] adopted a fixed heat flux boundary condition of 3×10^9 eV cm^{-2} s^{-1} for the electron gas. To approximate variation during the solar cycle, we initially used the *Titheridge* [1998] empirical model to create global average electron temperature profiles, and from these profiles we calculated a simple linear relationship

for the heat flux as a function of solar cycle. This parameterization results in heat fluxes of

4.4 and 7.2×10^9 eV cm^{-2} s^{-1} at solar minimum and maximum respectively. A different approach

is described in section 6.3. For the ions we assume a free upper boundary condition, $\frac{\partial^2 T_i}{\partial z^2} = 0$.

3.3. Momentum and Continuity Equations

The momentum equation for the neutral constituents follows from the development of

Chapman and Cowling [1952]. *Colegrove et al.* [1966] later included a term to approximate the

effects of eddy diffusion. The resulting one-dimensional equation for component i of a multi-

species gas, neglecting bulk motion, can be written as

$$\varphi_i = -D_i \left(\frac{\partial n_i}{\partial z} + \frac{n_i}{H_i} + (1 + \alpha_i) \frac{n_i}{T} \frac{\partial T}{\partial z} - n_i \sum_{j \neq i} \frac{\varphi_j}{ND_{ij}} \right) - K_{eddy} \left(\frac{\partial n_i}{\partial z} + \frac{n_i}{H_{mix}} + \frac{n_i}{T} \frac{\partial T}{\partial z} \right), \qquad (5)$$

where n_i, φ_i, and α_i identify the concentration, flux, and thermal diffusion factor of species i

respectively; T is the neutral gas temperature. The thermal diffusion factor is assumed to be zero

for all species except helium, for which it is set to -0.4 [*Colegrove et al.*, 1966]. H_i is the scale

height of species i, while H_{mix} is the scale height of the gas mixture. The diffusion coefficient D_i

is given by

$$D_i \equiv \left(\sum_{j \neq i} \frac{n_j}{ND_{ij}} \right)^{-1}. \qquad (6)$$

The mutual diffusion parameter ND_{ij} is a function of temperature as well as the colliding

species i and j; when available, experimental results are used [*Colegrove et al.*, 1966]. Otherwise

we rely on the hard sphere approximation, and estimates of the collision diameter given by *Lettau*

[1951]. When applying (5) and (6) to minor neutral species, the sum j is over just the three major

constituents.

The flux, φ_i, specified by the momentum equation above is substituted into the continuity

equation

$$\frac{\partial n_i}{\partial t} = P_i - L_i n_i - \frac{\partial \varphi_i}{\partial z}$$
(7)

to give a second order partial differential equation that can be solved discretely using finite differencing. P_i and L_i are the constituent-dependent production and loss terms, which include photoionization, photodissociation, and the chemical reactions listed in Tables 1 and 2 below.

Table 1. Neutral-Neutral Chemical Reactions Used in the GAIT Model.

Reaction	Reaction Rate and Reference	
$O + O + M \xrightarrow{k1} O_2 + M + 5.12\,eV$	$k_1 = 9.59 \times 10^{-34} \, Exp[480/T]$	(a)
$O + O_2 + M \xrightarrow{k2} O_3 + M + 1.10\,eV$	$k_2 = 6.0 \times 10^{-34} \, (300/T)^{2.4}$	(b)
	$k_3 = 1.8 \times 10^{-11} \, Exp[110/T]$	(b)
$O(^1D) + N_2 \xrightarrow{k3} O + N_2 + 1.97\,eV$	$k_4 = 2.46 \times 10^{-11} \, Exp[70/T]$	(b)/(f)
$O(^1D) + O_2 \xrightarrow{k4} O + O_2(^1\Sigma_g) + 0.34\,eV$	$k_5 = 7.35 \times 10^{-12} \, Exp[70/T]$	(b)/(f)
$O(^1D) + O_2 \xrightarrow{k5} O + O_2 + 1.97\,eV$	$k_6 = 3.6 \times 10^{-18} \, Exp[-220/T]$	(b)
	$k_7 = 2.2 \times 10^{-15}$	(c)
$O_2(^1\Delta_g) + O_2 \xrightarrow{k6} O_2 + O_2 + 0.98\,eV$	$A_8 = 2.58 \times 10^{-4} \, s^{-1}$	(c)
$O_2(^1\Sigma_g) + M \xrightarrow{k7} O_2(^1\Delta_g) + M + 0.65\,eV$	$A_9 = 0.085 \, s^{-1}$	(c)
$O_2(^1\Delta_g) \xrightarrow{A8} O_2 + h\nu$	$A_{10} = 8.33 \times 10^{-3} \, s^{-1}$	(d)
	$k_{11} = 8 \times 10^{-12} \, Exp[-2060/T]$	(b)
$O_2(^1\Sigma_g) \xrightarrow{A9} O_2 + h\nu$	$k_{12} = 5 \times 10^{-12}$	(a)
$O(^1D) \xrightarrow{A10} O + h\nu$	$k_{13} = 1.5 \times 10^{-11} \, Exp[-3600/T]$	(b)
$O + O_3 \xrightarrow{k11} 2O_2 + 4.06\,eV$	$k_{14} = 2.1 \times 10^{-11} \, Exp[100/T]$	(c)
	$k_{15} = 6.9 \times 10^{-13}$	(e)
$N(^2D) + O_2 \xrightarrow{k12} NO + O(^1D) + 1.84\,eV$	$k_{16} = 3.6 \times 10^{-10} \, (T_e/300)^{0.5}$	(a)
$N(^4S) + O_2 \xrightarrow{k13} NO + O + 1.4\,eV$	$k_{17} = 7 \times 10^{-11}$	(a)
$NO + N(^4S) \xrightarrow{k14} N_2 + O + 2.68\,eV$	$A_{18} = 1.06 \times 10^{-5} \, s^{-1}$	(a)
$N(^2D) + O \xrightarrow{k15} N(^4S) + O + 2.38\,eV$	(a) *Roble et al.* [1987] and references therein.	
$N(^2D) + e^- \xrightarrow{k16} N(^4S) + e^- + 2.38\,eV$	(b) *JPL* [2003]. (c) *Roble* [1995].	
$N(^2D) + NO \xrightarrow{k17} N_2 + O + 5.63\,eV$	(d) *Nee and Lee* [1997]. (e) *Fell et al.* [1990].	
$N(^2D) \xrightarrow{A18} N(^4S) + h\nu$	(f) *Mlynczak and Solomon* [1993].	

Table 2. Ion-Neutral Chemical Reactions Used in the GAIT Model.

Reaction	Reaction Rate and Reference
$O^+ + N_2 \xrightarrow{\gamma 1} NO^+ + N(^4S) + 1.10\,eV$	$\gamma_1 = (i)$ (a)
$O^+ + O_2 \xrightarrow{\gamma 2} O_2^+ + O + 1.55\,eV$	$\gamma_2 = (ii)$ (a)
$O^+ + NO \xrightarrow{\gamma 3} NO^+ + O + 4.36\,eV$	$\gamma_3 = (iii)$ (a)
$O^+ + CO_2 \xrightarrow{\gamma 4} O_2^+ + CO$	$\gamma_4 = 9.4 \times 10^{-10}$ (e)
$O_2^+ + NO \xrightarrow{\gamma 5} NO^+ + O_2 + 2.81\,eV$	$\gamma_5 = 4.6 \times 10^{-10}$ (a)
$O_2^+ + N(^4S) \xrightarrow{\gamma 6} NO^+ + O + 4.21\,eV$	$\gamma_6 = 1.5 \times 10^{-10}$ (b)
$O_2^+ + N_2 \xrightarrow{\gamma 7} NO^+ + NO + 0.93\,eV$	$\gamma_7 = 5 \times 10^{-16}$ (a)
$N_2^+ + O_2 \xrightarrow{\gamma 8} O_2^+ + N_2 + 3.53\,eV$	$\gamma_8 = 5 \times 10^{-11}(300/T_i)$ (a)
$N_2^+ + O \xrightarrow{\gamma 9} O^+ + N_2 + 1.96\,eV$	$\gamma_9 = \begin{cases} 1 \times 10^{-11}(300/T_i)^{0.23}; & T_i \leq 1500 \\ 3.62 \times 10^{-12}(T_i/300)^{0.41}; & T_i > 1500 \end{cases}$ (a)
$N_2^+ + O \xrightarrow{\gamma 10} NO^+ + N(^2D) + 0.7\,eV$	$\gamma_{10} = \begin{cases} 1.4 \times 10^{-10}(300/T_i)^{0.44}; & T_i \leq 1500 \\ 5.2 \times 10^{-11}(T_i/300)^{0.2}; & T_i > 1500 \end{cases}$ (a)
$N^+ + O_2 \xrightarrow{\gamma 11} O_2^+ + N(^2D) + 0.1\,eV$ $\rightarrow O_2^+ + N(^4S) + 2.49\,eV$	$\gamma_{11} = 3.07 \times 10^{-10}$; Yield $(0.66/0.33)$ (d)
$N^+ + O_2 \xrightarrow{\gamma 12} NO^+ + O + 6.67\,eV$	$\gamma_{12} = 2.32 \times 10^{-10}$ (b)
$N^+ + O \xrightarrow{\gamma 13} O^+ + N(^4S) + 0.93\,eV$	$\gamma_{13} = 1 \times 10^{-12}$ (e)
$O_2^+ + e^- \xrightarrow{\gamma 14} O(^3P) + O(^3P) + 6.99\,eV$ $\rightarrow O(^3P) + O(^1D) + 5.02\,eV$ $\rightarrow O(^1D) + O(^1D) + 3.06\,eV$	$\gamma_{14} = \begin{cases} 1.95 \times 10^{-7}(300/T_e)^{0.7}; & T_e \leq 1200 \\ 7.38 \times 10^{-8}(1200/T_e)^{0.56}; & T_e > 1200 \end{cases}$ (b) Yield $(0.22, 0.42, 0.36)$
$N_2^+ + e^- \xrightarrow{\gamma 15} N(^4S) + N(^2D) + 3.44\,eV$ $\rightarrow N(^4S) + N(^4S) + 5.82\,eV$	$\gamma_{15} = 2.2 \times 10^{-7}(300/T_e)^{0.39}$ (b)/(e) Yield $(0.9/0.1)$
$NO^+ + e^- \xrightarrow{\gamma 16} O + N(^2D) + 0.38\,eV$ $\rightarrow O + N(^4S) + 2.77\,eV$	$\gamma_{16} = 4.2 \times 10^{-7}(300/T_e)^{0.85}$ (c) Yield $(0.85/0.15)$

$$(i) = \begin{cases} 1.533 \times 10^{-12} - 5.92 \times 10^{-13}T_x + 8.6 \times 10^{-14}T_x^2 & 300 \leq T_i \leq 1700 \\ 2.73 \times 10^{-12} - 1.155 \times 10^{-12}T_x + 1.48 \times 10^{-13}T_x^2 & 1700 > T_i > 6000 \end{cases}$$

$$(ii) = 2.82 \times 10^{-11} - 7.74 \times 10^{-12}T_x + 1.073 \times 10^{-12}T_x^2 - 5.17 \times 10^{-14}T_x^3 + 9.65 \times 10^{-16}T_x$$

$$(iii) = \begin{cases} 8.36 \times 10^{-13} - 2.02 \times 10^{-13}T_x + 6.95 \times 10^{-14}T_x^2 & 320 \leq T_i \leq 1500 \\ 5.33 \times 10^{-13} - 1.64 \times 10^{-14}T_x + 4.72 \times 10^{-14}T_x^2 - 7.05 \times 10^{-15}T_x^3 & 1700 > T_i > 6000 \end{cases}$$

Where $T_x = T_i/300$

Table 2 continued. Ion-Neutral Chemical Reactions Used in the GAIT Model.

Reaction	Reaction Rate	Reference
$O^+(^2P) + N_2 \xrightarrow{\gamma 17} N_2^+ + O + 3.02\,eV$	$\gamma_{17} = 4.8 \times 10^{-10}$	(e)
$O^+(^2P) + N_2 \xrightarrow{\gamma 18} N^+ + NO + 0.70\,eV$	$\gamma_{18} = 1 \times 10^{-10}$	(e)
$O^+(^2P) + O \xrightarrow{\gamma 19} O^+(^4S) + O + 5.0\,eV$	$\gamma_{19} = 5 \times 10^{-11}$	(e)
$O^+(^2P) + e^- \xrightarrow{\gamma 20} O^+(^4S) + e^- + 5.0\,eV$	$\gamma_{20} = 4 \times 10^{-8}\,(300/T_e)^{1/2}$	(e)
$O^+(^2P) + e^- \xrightarrow{\gamma 21} O^+(^2D) + e^- + 1.69\,eV$	$\gamma_{21} = 1.5 \times 10^{-7}\,(300/T_e)^{1/2}$	(e)
$O^+(^2P) \xrightarrow{A22} O^+(^4S) + h\nu$	$A_{22} = 0.047\,s^{-1}$	(e)
$O^+(^2P) \xrightarrow{A23} O^+(^2D) + h\nu$	$A_{23} = 0.171\,s^{-1}$	(e)
$O^+(^2D) + N_2 \xrightarrow{\gamma 24} N_2^+ + O + 1.33\,eV$	$\gamma_{24} = 8 \times 10^{-10}$	(e)
$O^+(^2D) + O \xrightarrow{\gamma 25} O^+(^4S) + O + 3.31\,eV$	$\gamma_{25} = 1 \times 10^{-11}$	(e)
$O^+(^2D) + e^- \xrightarrow{\gamma 26} O^+(^4S) + e^- + 3.31\,eV$	$\gamma_{26} = 6.6 \times 10^{-8}\,(300/T_e)^{1/2}$	(e)
$O^+(^2D) + O_2 \xrightarrow{\gamma 27} O_2^+ + O + 4.87\,eV$	$\gamma_{27} = 7 \times 10^{-10}$	(e)

(a) *Schunk* [1988] and references therein.
(b) *Schunk and Nagy* [2000].
(c) *Vejby-Christensen et al.* [1998].
(d) *Rees* [1989].
(e) *Roble* [1995].

Tables 1 and 2 list the neutral-neutral and neutral-ion chemical reactions used in the GAIT model; exothermic reaction energies, reaction rates, and references are also given. The model's chemical scheme is primarily a subset of the relevant reactions listed by *Roble* [1995], updated to include new rate coefficients and quantum yields, with a few additions to the ion chemistry based on the work of *Schunk* [1988]. Note some of the reaction rates listed in Table 2 involve the ion temperature, T_i. This temperature dependence is in fact determined by the effective temperature, which is given by equation (57) of *Schunk* [1988]. However, for this work the effective temperature is well approximated by the ion temperature.

When solving the coupled continuity and momentum equations, diffusive equilibrium is imposed at the upper boundary; the lower boundary condition depends on the species. N_2 and O_2 concentrations are fixed at $2.28 \times 10^{13}\,cm^{-3}$ and $5.72 \times 10^{12}\,cm^{-3}$, based on globally averaged MSIS-90 results. As observed previously with the neutral temperature, these boundary conditions

vary on the order of 1% over the course of the solar cycle, reflecting stability of the pressure surface and mixing ratio at 95 km. The globally averaged atomic oxygen profile calculated by MSIS-90 peaks in the vicinity 95 km, and we therefore assume a lower boundary condition of $\frac{\partial[O]}{\partial z} = 0$ for the O density. Boundary conditions for the minor neutral species are described in section 3.7.

Of the ions, both $O^+(^4S)$ and N^+ are subject to transport. The rest are assumed to be in photochemical equilibrium. The ion momentum equation is similar to (5),

$$\varphi_i = -\sin^2 I D_a \left(\frac{\partial n_i}{\partial z} + \frac{n_i}{H_p} + \frac{n_i}{T_p} \frac{\partial T_p}{\partial z} \right), \tag{8}$$

where we have replaced the diffusion coefficient, scale height, and neutral temperature with equivalent plasma parameters [*Schunk*, 1988; *Schunk and Nagy* 2000]. We also neglect the eddy diffusion term in (5), because the ions are in photochemical equilibrium at the altitudes where eddy diffusion is important, and assume zero bulk flow for the neutral gas. Photochemical equilibrium is assumed as a lower boundary condition.

Production and loss terms for the ions include photoionization, secondary ionization by photoelectrons (section 3.8), and the chemical reactions listed in Table 2. Three of the photochemical ion species (NO^+, O_2^+, and N_2^+) are coupled nonlinearly through dissociative recombination reactions with electrons (γ_{14}, γ_{15}, and γ_{16} in Table 2). To facilitate a stable solution, the corresponding continuity equations are expanded in a Taylor's series using the method described by *Schunk* [1988].

3.4. Solar Irradiance

Roble et al. [1987] relied on measurements from the Atmospheric Explorer (AE) satellites to specify the solar irradiance [*Hinteregger et al.*, 1981; *Torr and Torr*, 1980; *Torr and Torr*, 1985]. Since that time, additional measurements and improved instrument calibration have resulted in

new solar irradiance models. The standard solar irradiance input for the GAIT model is based on the vacuum ultraviolet (VUV) model [*Woods and Rottman*, 2002]. The VUV model specifies the solar irradiance at 1-nm resolution from 0-420 nm, although the GAIT model uses only a subset of that range, 3 to 360 nm. For wavelengths longward of 119 nm, the VUV reference spectrum and solar cycle variability are derived from measurements made by the Upper Atmosphere Research Satellite (UARS). At wavelengths less than 119 nm, the reference spectrum is based on a sounding rocket flight [*Woods et al.*, 1998], while the solar cycle variability is derived from four years of measurements made on the AE-E satellite during the ascending phase of solar cycle 21.

In order to specify the solar irradiance in different phases of the solar cycle, we must adopt a solar activity proxy. A number of different proxies are in use today, including the 10.7 cm solar radio flux (F10.7), its 81-day centered average (<F10.7>), the Magnesium II core-to-wing ratio, and the composite Lyman-alpha index. Because the observed irradiance originates from the entire solar atmosphere, no single proxy is ideal for all wavelengths, and indeed most solar irradiance models employ at least two. The oldest proxies, F10.7 and <F10.7>, are still widely used; however, *Balan et al.* [1994a; 1994b] argued that for high levels of solar activity, the desired linear relationship between F10.7 and EUV irradiance breaks down. *Richards et al.* [1994] showed a similar breakdown, but found they could restore quasi-linearity over a wide range of solar activity by adopting a new proxy, P, defined as the average of the F10.7 and <F10.7> values,

$$P = (F10.7 + <F10.7>)/2. \tag{9}$$

The GAIT model adopts the P index, and assumes it is linear with respect to the solar irradiance over the entire solar cycle. The derived VUV solar minimum and maximum spectra correspond to two 27-day periods centered on 17 April 1996 and 1 February 1992, respectively.

To employ the VUV model, we first calculated the average P value centered on these dates

and then performed a simple linear interpolation. For a desired level of solar activity, the photon

flux in each wavelength bin is determined by multiplying the solar minimum value by a factor

that depends on the associated P index. Figure 2 details the VUV solar irradiance as it is used in

the GAIT model. The top panel shows the solar minimum (P = 70) photon flux, while the bottom

panel shows the multiplicative factor that must be applied to reach solar maximum (P = 230).

Note the shortest EUV wavelengths (less than 40 nm), which originate primarily in the solar
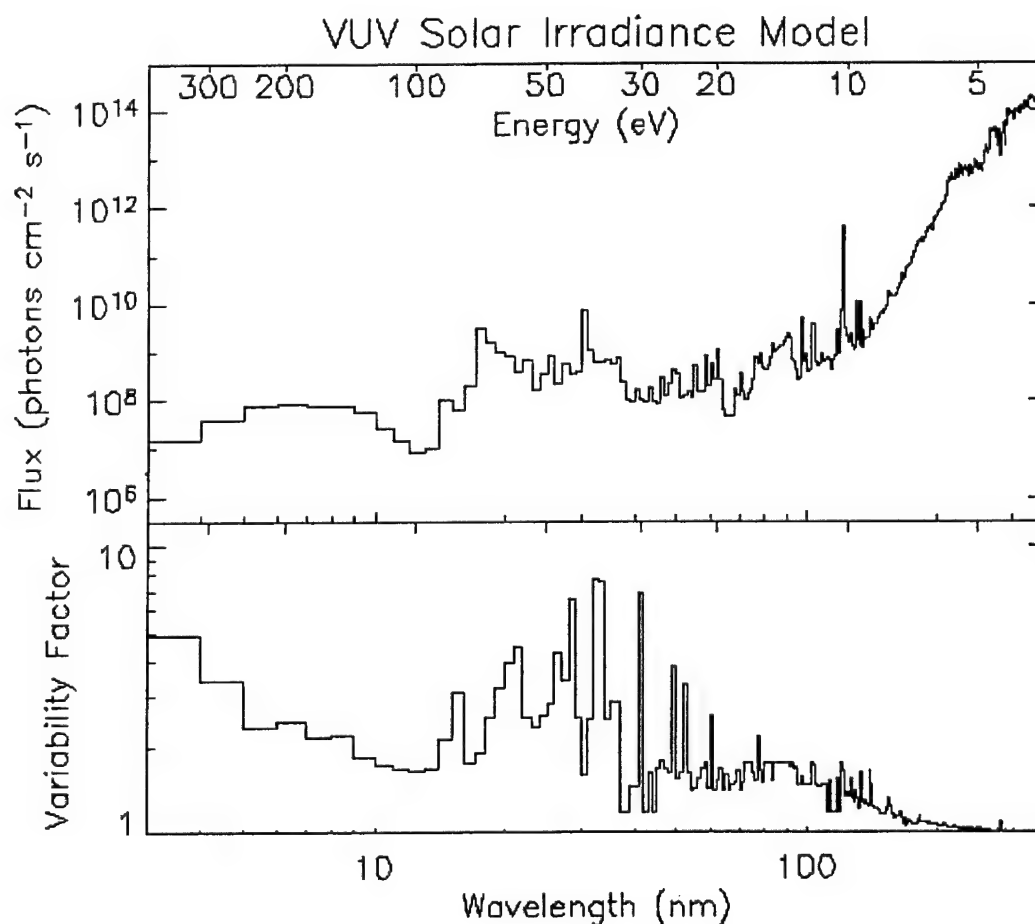
Figure 2. The standard solar input based on the VUV model of *Woods and Rottman* [2002]. The top panel shows the VUV solar minimum reference spectrum, while the bottom panel shows the multiplicative factor that must be applied to each wavelength bin in order to obtain a solar maximum spectrum.

corona, have the highest variability. The longer UV wavelengths originate lower in the

solar atmosphere and have correspondingly lower variability.

Once the input solar spectrum is specified, we are able to calculate effective photoabsorption

rates, which in turn lead to dissociation and ionization, driving the chemistry of the model. The

global average photoabsorption rate at altitude z, by species i, is given by the expression

$$\bar{J}_i(z) = \frac{1}{2} \int_{-1}^{1} d\mu \, n_i(z) \int_{\lambda} d\lambda \, I_\infty(\lambda) \sigma_i(\lambda) \text{Exp}[-\tau(\lambda, \mu, z)]. \tag{10}$$

Here n_i is the concentration and σ_i the absorption cross section of species i, I_∞ identifies the solar

flux at the top of the atmosphere, and τ the optical depth. The rigorous calculation of optical

depth in a spherical atmosphere involves a complicated dependence on the solar zenith angle and

z [Rees, 1989], but it is well approximated using the method of Smith and Smith [1972]. In the

above expression, the outer integration is over the cosine of the solar zenith angle μ. Although

the exact average involves integrating the zenith angle from 0 to 180 degrees, in practice there is

no contribution to the result past about 110 degrees. The GAIT model computes this outer

integral using Gaussian Quadrature. The inner integration is over λ, the incident wavelength,

which the model treats using a sum over the relevant bins.

3.5. Neutral Gas Heating

The global average heating rate, Q in equation (1), consists of a number of different

processes: (a) excess energy available after photodissociation, (b) heating from exothermic

neutral-neutral chemical reactions, including recombination of atomic oxygen and quenching of

excited species, (c) heating from exothermic ion-neutral chemical reactions, (d) collisions

between thermal electrons, ions, and neutrals, and (e) Joule heating. All but one of these

processes (Joule heating) begins with the absorption of solar photons described by equation (10).

In the solar EUV wavelengths, absorption of a photon results primarily in photoionization of

the neutral species, although dissociation and dissociative ionization also occur. Torr et al.

[1979] parameterized the flux from 5-105 nm into 37 wavelength bins and provided effective absorption and ionization cross sections. These flux averaged cross sections were updated by *Richards et al.* [1994] to include more recent measurements compiled by *Fennelly and Torr* [1992]. The GAIT model extends the coverage down to 3 nm using the Fennelly and Torr data.

Due to a window between the absorption bands of molecular oxygen, the strong H Lyman-alpha line at 121.6 nm is able to penetrate into the lower thermosphere and mesosphere. It does not have sufficient energy to ionize the major neutral species, but does ionize nitric oxide as well as dissociate molecular species such as O_2 and CO_2. The model includes the effects of H Lyman-alpha using cross-sections parameterized by *Nicolet* [1985].

Longward of the EUV, in the Schumann-Runge continuum (125-175 nm), the photons are absorbed primarily by O_2, resulting in dissociation into $O(^3P)$ and $O(^1D)$. The GAIT model uses 5-nm wide bins to represent the UV flux in this wavelength region. Flux averaged absorption cross sections were calculated from the data of *Strobel* [1978] and the quantum yield for production of $O(^1D)$ comes from *Nee and Lee* [1997] and *Lee and Nee* [2000].

Calculation of the O_2 photodissociation rate in the Schumann-Runge bands (175-195 nm) is complicated by a highly variable O_2 absorption cross section. Under these circumstances, the 1 to 5 nm wide flux averaged cross-sections we typically use are no longer physically representative, and the problem seemingly requires high-resolution integration over wavelength. A computationally efficient alternative is to transform the highly variable integrand into a smooth one using a cumulative distribution function. The algorithm and applicable coefficients used in the GAIT model have been described by *Minschwaner et al.* [1993a]. Subdivision of the Schumann-Runge band region is based on the location of the individual band heads, which results in 11 wavelength bins, varying from 0.8 to 2.2 nm wide. At these longer wavelengths the products of O_2 dissociation are all assumed to be in the ground state, $O(^3P)$.

Longward of 195 nm, absorption by O_2 is negligible, but photolysis of ozone in the Hartley (200-300 nm) and Huggins (300-350 nm) bands directly contributes roughly 2% of the total neutral gas heating rate, with some additional chemical heating through recombination of the dissociated products. The Hartley region is subdivided into 10-nm wide bins, while a single bin approximates the Huggins bands. Ozone photoabsorption cross sections and the quantum yield for excited state dissociation products are both from *JPL Publication 02-25* [2003].

Roble and Emery [1983] and *Roble et al.* [1987] showed the global average exospheric temperature was too small without the addition of a high-latitude heat source to account for Joule heating as well as auroral particle input. *Roble et al.* [1987] argued quiet geomagnetic conditions were well represented by a global Joule heating of 70 GW and an auroral particle input of 13 GW. After accounting for the heating efficiency, *Roble et al.* [1987] found the total heating due to auroral particles to be only 1 GW, as compared to 70 GW from Joule heating. For this reason direct auroral particle heating is not included in the GAIT model. To account for Joule heating, we assume the same simple expression given by *Roble et al.* [1987]

$$Q_{Joule} = \sigma_p E^2, \tag{11}$$

where σ_p is the Pedersen conductivity and E an imposed electric field that is assumed constant in height. To account for changes in σ_p, the applied electric field is updated at each integration step ensuring the total Joule heating rate remains fixed. Based on this approach, Joule heating accounts for 5 to 7% of the net heating over the course of the normal solar cycle.

3.6. Neutral Gas Cooling

The loss term, L, in equation (1) is composed of three infrared radiative cooling mechanisms: (a) 63 μm cooling due to the fine structure of atomic oxygen, (b) 5.3 μm cooling from the fundamental band of nitric oxide, and (c) cooling due to the 15 μm band of carbon dioxide.

In the simplest case, the energy loss rate for a given transition is expressed as

$$L(m \to l) = (E_m - E_l) A_{ml} n_m, \tag{12}$$

where L is the cooling rate, E_m-E_l the energy difference between the states m and l, A_{ml} the

radiational decay rate, and n_m the excited state population. If the collision frequency is large

relative to A_{ml}, the population is assumed to be in local thermodynamic equilibrium (LTE),

otherwise one must use detailed balance to derive a non-LTE expression for the excited state

population. Complications to this simple expression arise for a number of reasons; for example,

when the radiation is reabsorbed within the region of interest, or there are multiple interacting

transitions.

Bates [1951] was the first to demonstrate the importance of infrared cooling at 63 μm,

assuming both an LTE population distribution and an optically thin atmosphere. At low altitudes,

however, the atmosphere is optically thick to 63 μm. Separately *Craig and Gille* [1969] and

Kockarts and Peetermans [1970] developed equivalent algorithms to calculate a correction factor

that accounts for radiative transfer in an optically thick atmosphere. *Glenar et al.* [1978]

parameterized the full radiative transfer result to obtain a simple reduction factor that varies with

altitude. Comparisons using the GAIT model show the exospheric temperature resulting from the

full radiative transfer calculation differs by less than 1% from the Glenar parameterization over

the course of the normal solar cycle. For this reason, the results described here employ Glenar's

simple parameterized reduction factor.

A number of authors have questioned how well the fine structure of atomic oxygen is

represented by an LTE approximation. Analysis of a rocket measurement by *Grossmann and*

Offermann [1978] showed the 63 μm emissions to be much lower than expected at 120 km. For

this reason, as well as physical arguments by *Durrance and Thomas* [1979], *Roble et al.* [1987]

arbitrarily reduced the 63 μm cooling rate in their model by a factor of 2, in order to approximate

non-LTE effects. However, later measurements by *Grossmann and Vollmann* [1997] supported

an LTE population distribution up to approximately 180 km. In addition, *Sharma et al.* [1994]

provided theoretical arguments for an LTE distribution up to 400 km during solar minimum and 600 km during solar maximum. Given these new results, the GAIT model uses the LTE assumption, recognizing the 63 μm cooling rate is probably too large at high altitudes, especially at solar minimum. If instead we use the approach of *Roble et al.* [1987], and divide the 63 μm cooling rate by two, the resulting exospheric temperatures are 4% higher at solar minimum and 2% higher at maximum.

Emission at 5.3 μm from the fundamental band of nitric oxide is an important cooling mechanism, especially at solar maximum and in auroral regions. *Kockarts* [1980] showed that unlike the 63 μm fine structure, the fundamental NO emission is not in local thermodynamic equilibrium. The population of NO in the $v = 1$ vibrational level is calculated by detailed balance using the expression derived by *Kockarts* [1980]. Given the relative excitation rates, collisions between NO and O are the most important. Although past values for this crucial excitation rate have ranged from 3.3×10^{-12} cm^{3}s^{-1} [*Klein and Herron*, 1964] to 6.5×10^{-11} cm^{3}s^{-1} [*Fernando and Smith*, 1979], recent theoretical [*Duff and Sharma*, 1997] and experimental [*Dodd et al.*, 1999] work have narrowed the accepted range to 2.8 and $2.4 \times 10^{-11} \pm 0.5$ cm^3 s^{-1} respectively. The GAIT model adopts the higher of these two values. For comparison, a low value of 1.9×10^{-11}, which falls within the experimental uncertainty of the *Dodd et al.* [1999] result, leads to exospheric temperatures that are 1 and 4% higher at solar minimum and maximum respectively.

Cooling by CO_2 at 15 μm requires both a consideration of non-LTE effects as well as radiative transfer. In addition, closely spaced energy levels and differences between CO_2 isotopes makes it the most difficult of the three radiative processes to model. The parameterization of *Fomichev et al.* [1998], which is used in the GAIT model, takes into account all of these processes, using different algorithms for the LTE, non-LTE, and transition regions as appropriate. As was the case for the cooling by NO, there is uncertainty in the rate coefficient for excitation of

vibration by collisions between CO_2 and O. We use the rate suggested by *Sharma and Wintersteiner* [1990], and discuss the model's sensitivity to this rate further in Chapter 5.

3.7. Minor Neutral Constituents

The metastable states of atomic and molecular oxygen, $O(^1D)$, $O_2(^1\Delta_g)$, and $O_2(^1\Sigma_g)$ are assumed to be in photochemical equilibrium. These excited-state species are produced primarily during the dissociation of O_2 and O_3 by UV radiation; loss rates via quenching collisions and spontaneous emission are given in Table 1.

Ozone is included in the model for its minor role in neutral gas heating. Based on the results of *Allen et al.* [1984], we assume ozone to be in photochemical equilibrium. The sole production term is through recombination of O and O_2, while photolysis provides the dominant loss mechanism. For completeness, the reaction of ozone with atomic hydrogen, a secondary O_3 loss mechanism and source of chemical heat [*Mlynczak and Solomon*, 1993], is approximated using a static hydrogen concentration, but the net effect of this approximation on the neutral gas heating rate is negligible. Photolysis cross sections and quantum yields for excited state products are taken from *JPL* [2003].

The carbon dioxide concentration is of great importance given its role in cooling the neutral gas. Based on the work of *Trinks and Fricke* [1978], carbon dioxide is subject to vertical transport with no production terms and only two loss terms, photolysis and chemical reaction with $O^+(^4S)$. CO_2 photoabsorption cross sections used in the GAIT model are taken from *Yoshino et al.* [1996], *Shemansky* [1972], and *Nicolet* [1985]. Because global empirical models for the CO_2 concentration do not exist, the lower boundary condition is specified using a fit to experimental data provided by *Fomichev et al.* [1998] that corresponds to a mixing ratio of 360 ppm in the homosphere; by comparison, *Roble* [1995] specified 350 ppm for a global average boundary condition at 30 km. Although there is some uncertainty in the mixing ratio, the model results are relatively insensitive to it. Varying the homosphere mixing ratio from 300 to 400 ppm

results in a 3.5% change to the neutral exospheric temperature at solar minimum, and only 1% at solar maximum when cooling by NO becomes important.

In order to calculate the nitric oxide concentration, an important contributor to radiative cooling, we must also account for both ground state and metastable atomic nitrogen, $N(^4S)$ and $N(^2D)$. The concentrations of NO and $N(^4S)$ are modeled as minor species subject to transport, whereas photochemical equilibrium is assumed for $N(^2D)$. The production of $N(^2D)$ and $N(^4S)$ comes primarily through the neutral-ion chemistry listed in Table 2; however, dissociation of N_2 via EUV photons is also an important source of atomic nitrogen. We use the procedure of *Richards et al.* [1981] to account for this contribution and assume a 50% quantum yield for both the ground and metastable state products. The two major sources of nitric oxide involve reactions between atomic nitrogen, both $N(^2D)$ and $N(^4S)$, and molecular oxygen, listed in Table 1. Photolysis of NO in the Schumann-Runge bands is included using the method of *Minschwaner et al.* [1993b]. At the lower boundary, we use the approach of *Roble et al.* [1987]; $N(^4S)$ is assumed to be in photochemical equilibrium, while for NO we allow a small downward flux. *Roble et al.* [1987] chose this flux in order to create a peak in NO at roughly 105 km. Other than to generate a physically satisfying low-altitude profile for NO, the choice of downward flux is irrelevant. Cooling by CO_2 dominates at the model's lower boundary, and the choice of flux does not affect higher altitudes where cooling by NO is important.

Helium is included in the model as a passive tracer. Its vertical distribution is governed solely by diffusive transport, both eddy and molecular. The resulting vertical profile was used to help tune the eddy diffusion coefficient through comparison with the MSIS-90 model. At high altitudes He also contributes to the diffusion coefficient and thermal conductivity.

3.8. Photoelectrons

Photoelectrons provide the primary heat source for thermal electrons, as well as an important source of secondary ionization to the neutrals. Although a majority of the neutral excitation

results in airglow, energy that is assumed lost, a fraction heats the neutral gas as well. Photoelectron models exist, but are computationally cumbersome and therefore typically not included in coupled thermosphere/ionosphere models. The previous global average model of *Roble et al.* [1987] relied on a parameterization by *Swartz and Nisbet* [1972] to specify the thermal electron heating rate as a function of the total photoionization rate. Similarly, *Roble et al.* [1987] assumed secondary photoelectron impact ionization to be 30% of the primary photoionization rate. *Richards and Torr* [1988] calculated photoelectron ionization rate ratios as a function of both altitude and species. Above 150 km these rates were roughly 30%, in line with the earlier assumptions, but in the E-region the ratio increases dramatically. While reasonably accurate for normal solar conditions, all of these parameterizations are based on an assumed solar spectrum and therefore cannot reflect gross changes for extreme solar input or variability in the spectral weighting between various spectra.

Rather than rely on parameterizations to account for photoelectrons, the GAIT model includes an approximate solution for the photoelectron flux based on the work of *Richards and Torr* [1983]. This approach uses a local equilibrium approximation to calculate the photoelectron flux at each altitude. The treatment of cascading electrons is simplified by assuming only a limited set of energy losses available to each electron based on the average losses for that particular energy. For a given energy bin, *Richards and Torr* [1983] assumed a maximum of three energy loss channels that depended on the initial energy as well as the neutral collision partner. For example, 30 eV photoelectrons colliding with N_2 were allowed to lose either 11, 13, or 15 eV, based on the N_2 inelastic cross-sections. The GAIT model uses four loss channels that also depend on collision partner, but span the entire range of energies (0-400 eV). The excitation and ionization cross sections are based on the early parameterizations of *Green and Stolarski* [1972] and *Jackman et al.* [1977]; *Solomon et al.* [1988] updated the coefficients to include more recent measurements.

Using the local equilibrium approximation, *Richards and Torr* [1983] were able to show excellent agreement with a full calculation for altitudes below 250 km, and reasonable agreement with observations from the AE-E satellite. Above 300 km, transport effects become increasingly important and the approximation overestimates the photoelectron flux, especially at energies below 20 eV. For this reason, the GAIT model does not include photoelectron effects above a pressure coordinate of $Z = 3$ (300-400 km under normal solar conditions). This approach causes a small discontinuity in some of the minor neutral and ion constituents and an inflection in the electron temperature profile, but neither significantly affects the overall solution.

Richards and Torr [1983] cautioned that the photoelectron flux below 2 eV, which is responsible for most of thermal electron heating, may be too high at all altitudes due to transport effects. In fact, the electron heating rate calculated in the GAIT model is approximately 40% higher than the *Swartz and Nisbet* [1972] parameterization at the peak heating altitude. On the other hand, the ratios of photoelectron to primary ionization rates calculated by the GAIT model are remarkably similar to those calculated by *Richards and Torr* [1988] using a full photoelectron transport model. Figure 3 shows the ionization rate ratios calculated by the GAIT model for the three major neutral species during solar maximum ($P = 230$) conditions. The ratios for N_2 and O increase at low altitudes due to attenuation of the middle EUV wavelengths, which contribute to the primary photoionization rate but not the photoelectron flux. The O_2 ratio does not increase nearly as much because, unlike N_2 and O, it is also ionized by longer wavelength EUV photons which penetrate to low altitudes and offset the middle EUV attenuation. At 125 km the GAIT ratios are 0.26, 2.2, and 1.4 for O_2^+, N_2^+, and O^+ respectively, whereas *Richards and Torr* [1988] calculated ratios of approximately 0.2, 2.5, and 2.0. Because the GAIT approximation neglects transport, the high-altitude results most closely match the winter hemisphere calculations of *Richards and Torr* [1988], in which conjugate flux compensates for transport loss. In the summer, when there is no conjugate flux, the ratios decrease more quickly with altitude. At 400

Photoelectron Ionization Ratios
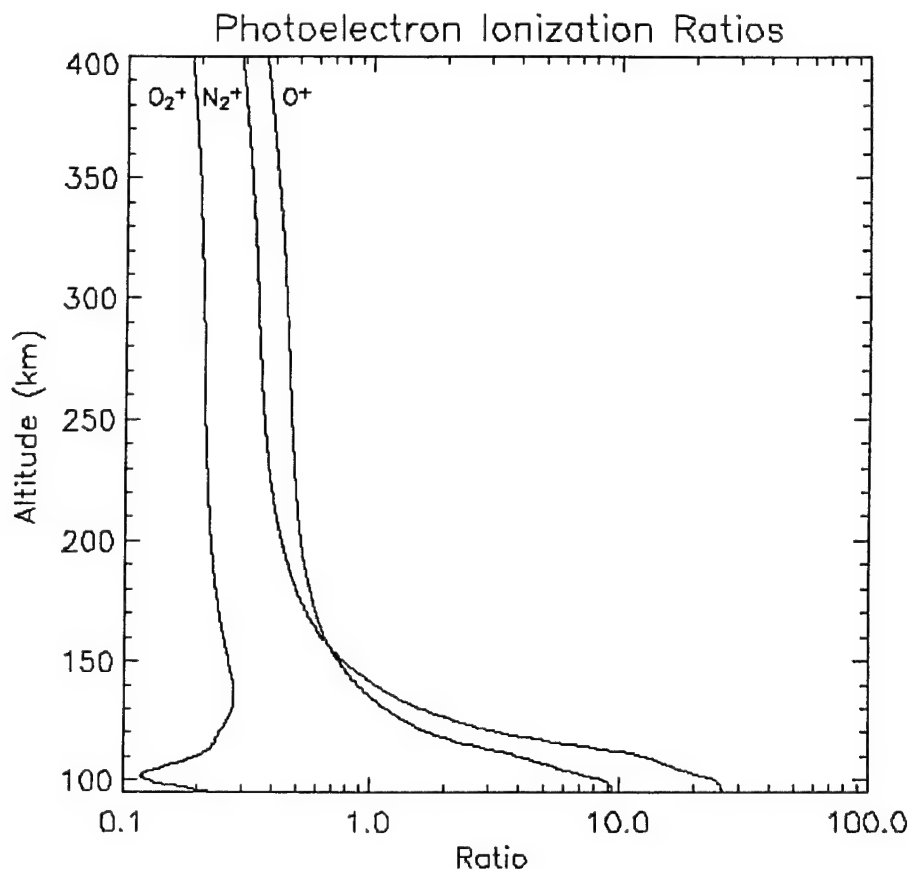
Figure 3. Secondary photoelectron to primary photon ionization rate ratios calculated using the GAIT model for solar maximum conditions (P = 230).

km the GAIT approximation gives ratios of 0.18 for O_2^+ and 0.29/0.36 for N_2^+/O^+, as compared to ~0.2 and ~0.3 from the *Richards and Torr* [1988] paper.

Although the local equilibrium approximation is not a perfect model for the photoelectron flux, it provides the GAIT model with the ability to respond physically to differences in the input solar spectrum that parameterizations cannot. Given the gross uncertainties in a global average representation of the thermosphere/ionosphere, the errors introduced by the *Richards and Torr* [1983] approximation are entirely acceptable.

CHAPTER 4

MODEL RESULTS AND VALIDATION

The GAIT model was run using the inputs described previously, for both solar maximum (P = 230) and minimum (P = 70), and assuming quiet geomagnetic conditions (Ap = 4). Other than changing the input solar irradiance, specified by the VUV model, all other input conditions remained fixed between the two runs. The upper boundary height was set to 700 km. The applied electric field associated with Joule heating was set such that it resulted in 70 GW of global heat input, as per the arguments of *Roble et al.* [1987]. This required an electric field of 7.7 mV/m at solar maximum and 11.0 mV/m at solar minimum.

Roble et al. [1987] described in detail the various heating and cooling rates, and their contribution to the global energy budget. In that paper, they found the relative contributions of CO_2 (15 μm), NO (5.3 μm), and O (63 μm) to the total infrared cooling to be 90, 6, and 4% respectively at solar minimum and 63, 33 and 4% at maximum. Since that time, a number of key reaction rates have changed, lending more importance to the CO_2 cooling at the expense of NO [*Sharma and Roble*, 2001]. Even so, using the GAIT model we obtained very similar numbers: CO_2 – 93%, NO – 2%, and O – 5% at solar minimum and 79, 16, and 5% respectively at maximum.

4.1. Neutral, Ion, and Electron Temperatures

Figure 4 shows the calculated neutral, ion, and electron gas temperature profiles for both solar minimum (top panel) and maximum (bottom panel), as well as the globally averaged neutral temperature profiles from the empirical MSIS-90 model. All of the profiles shown in this chapter are plotted using the pressure coordinate Z as the vertical axis in order to facilitate comparisons with the earlier global average model of *Roble et al.* [1987].
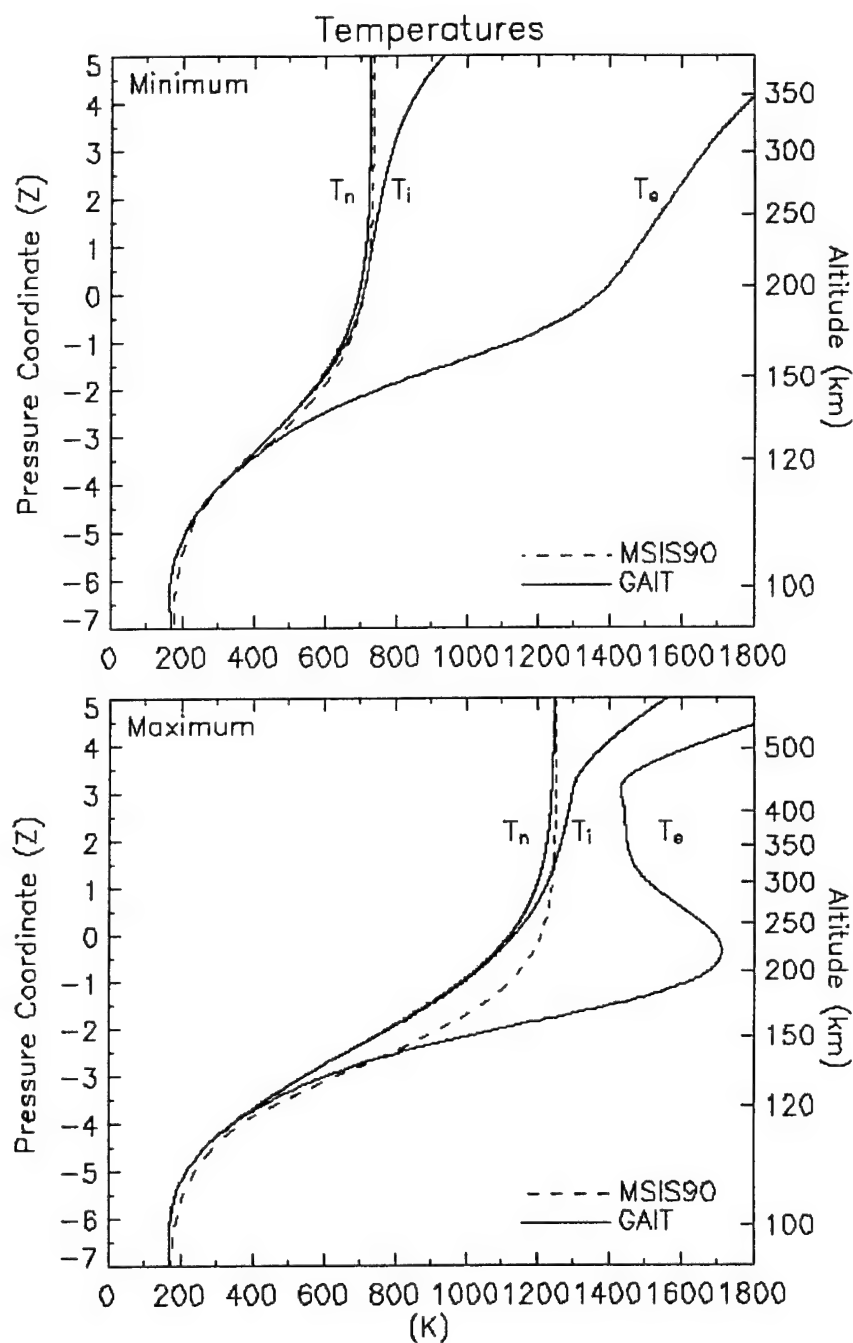
Figure 4. Global mean temperature profiles calculated using the GAIT model (solid lines) and MSIS-90 empirical model (dashed line). The three profiles correspond to neutral (T_n), ion (T_i), and electron (T_e) gases. The top panel is for solar minimum (P = 70) and the bottom panel for solar maximum (P = 230) assuming quiet geomagnetic conditions (Ap = 4).

At solar minimum, the GAIT model calculated an exospheric temperature of 728 K compared to an MSIS-90 value of 736 K. As Figure 4 demonstrates, the two solar minimum temperatures correlate extremely well over the entire profile. The solar minimum ion and electron temperature profiles are also very similar in both shape and magnitude to those of *Roble et al.* [1987]. At Z = 5 (~400 km) the electron temperature calculated by the GAIT model is 1920 K compared to approximately 1775 K calculated by *Roble et al.* [1987], but this is to be expected given the differences in electron heat flux at the top boundary. The parameterized heat flux described previously resulted in a value of 4.4×10^9 eV cm^{-2} s^{-1} at solar minimum versus the fixed value of 3×10^9 eV cm^{-2} s^{-1} used by *Roble et al.* [1987].

The GAIT model calculated a solar maximum exospheric temperature of 1250 K versus an MSIS-90 value of 1253 K; however, as the bottom panel of Figure 4 shows, the two temperature profiles do not track as closely as in the solar minimum case. At a pressure altitude of Z = –1.5 (~175 km) the MSIS-90 temperature is nearly 17% greater than the GAIT result. Comparison of the two profiles suggests excessive 5.3 μm NO cooling in the GAIT model at low altitudes, followed by excessive heating at high altitudes, possibly resulting from a high electron temperature. Better agreement with the MSIS-90 profile (a maximum difference of 11%) can be obtained by changing a disputed NO loss rate (reaction k_{14} in Table 1), using the photoelectron heating rate parameterization of *Swartz and Nisbet* [1972], and dividing the 63 μm O cooling rate by 2 (per *Roble et al.* [1987]). However, given the uncertainties inherent in comparing between global averages, we will continue to use the recommended reaction rate [*JPL*, 2003]. In section 5.1 we will investigate further the model's sensitivity to key inputs and reaction rates.

The calculated ion and electron temperature profiles at solar maximum are again similar to those of *Roble et al.* [1987]. A peak in the electron temperature at approximately 200 km corresponds to a maximum in photoelectron heating. The electron temperature at this local maximum is about 15% larger than the Roble value, reflecting the fact the photoelectron heating

rate calculated internally by the GAIT model is about 40% higher than the

parameterization used by *Roble et al.* [1987] (see section 3.8). Above this peak, the electron

temperature decreases to come within roughly 200 K of the neutral temperature. This reflects an

increased collisional coupling between electrons, ions, and neutrals at these altitudes, which is

greater at solar maximum than minimum due to the increased electron density. As was the case

for solar minimum, at the upper boundary the GAIT electron temperature is much higher than the

Roble et al. [1987] result, 2024 K versus ~1700 K, again due to the difference in the electron heat

flux boundary condition. The slope of the solar maximum electron temperature profiles shows a

small discontinuity at $Z = 3$, coinciding with where the photoelectron heating is turned off (see

section 3.8), while in the solar minimum case downward heat flux dominates, resulting in a

smooth profile.

4.2. Major Neutral Constituents

Global mean number densities for the three major neutral species are shown in Figure 5,

along with similar global means from the MSIS-90 model. Viewed on a log scale, the two

models appear to agree remarkably well over the entire altitude range, and at both solar minimum

and maximum. At solar minimum the largest difference between the GAIT and MSIS-90 results

are in O_2, which differ by 16% at $Z = 3.5$. The maximum difference in the N_2 and O profiles at

solar minimum are 9 and 5%. The close agreement between the atomic oxygen profiles is

especially good considering it uses a Neumann condition at the lower boundary rather than one

fixed to MSIS-90 (section 3.3). The agreement between the GAIT and MSIS-90 models is not

quite as good at solar maximum, which should be expected given the differences that exist in the

neutral temperature profile. The largest variation between the two models is again found in the

O_2 profile, which shows a 44% difference at $Z = -3$. The maximum differences in the N_2 and O

profiles are 21 and 16%, respectively, at roughly the same altitude.
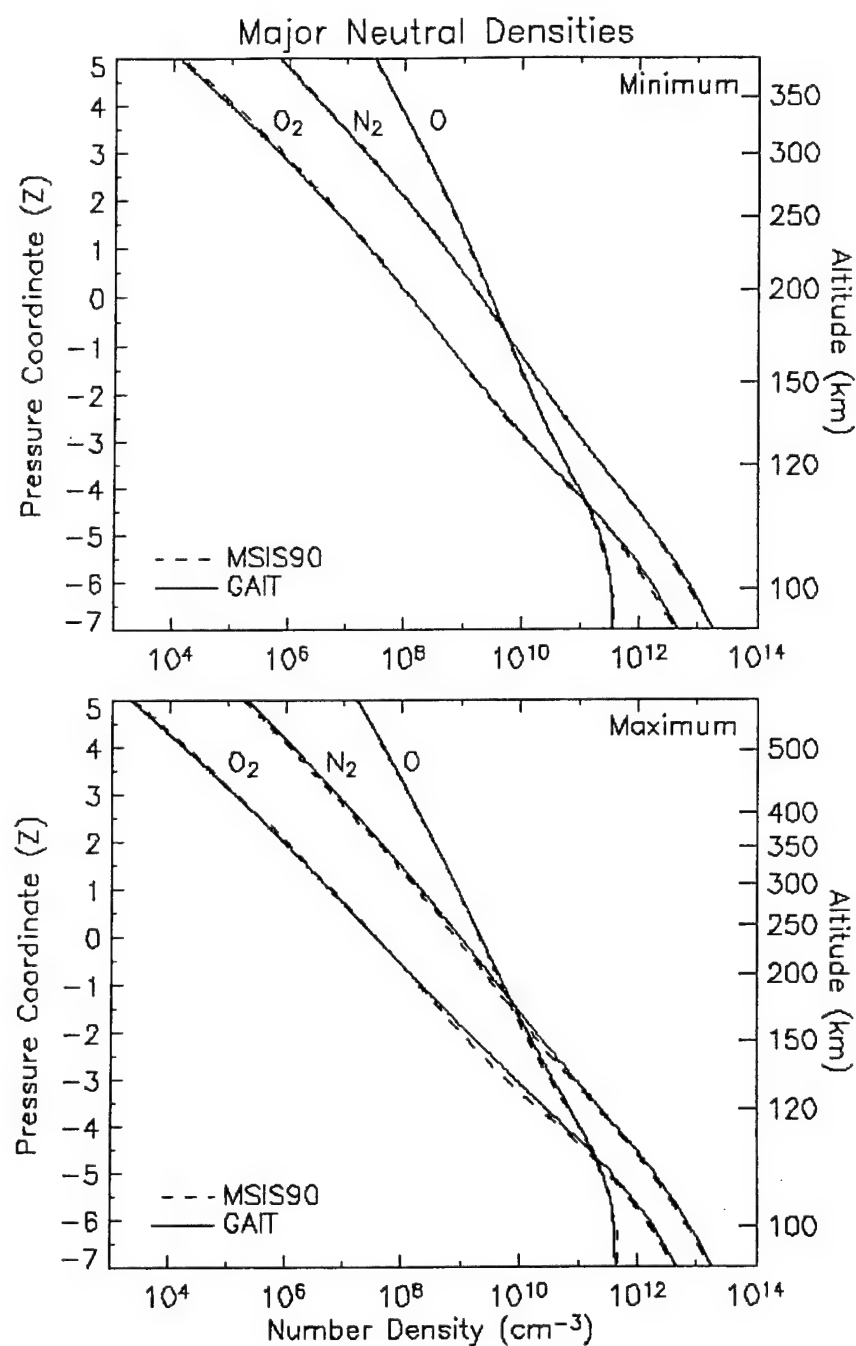
Figure 5. Global mean number density profiles for the three major neutral species (N_2, O_2, and O), calculated using the GAIT model (solid lines) and MSIS-90 empirical model (dashed lines). The top panel is for solar minimum (P = 70), and the bottom panel for solar maximum (P = 230) assuming quiet geomagnetic conditions (Ap = 4).

4.3. Ionospheric Constituents

Figure 6 shows the calculated global mean electron and ion density profiles for both solar minimum and maximum. A discontinuity in the NO^+ and N_2^+ concentrations at $Z = 3$ corresponds to where the photoelectron calculation stops (section 3.8), which reduces the effective ionization rate. A discontinuity also exists in the O_2^+ profile, but it is too small to be visible. Transport smoothes out any discontinuities in the O^+ and N^+ profiles. Fixed scale factors could be used to approximate secondary ionization above $Z = 3$, but the discontinuities are left in to both remind us of where the photoelectron calculation stops, as well as to indicate the magnitude of the effect they have on the total concentration. At solar minimum, eliminating the secondary ionization source decreases the N_2^+ and NO^+ densities by 27 and 21% respectively, while O_2^+ only decreases by 6%. The discontinuities at solar maximum are not visible in the figure, however, the N_2^+, NO^+, and O_2^+ concentrations decrease by 21, 5, and 6% respectively.

The results shown in Figure 6 are consistent with the previous global average results of *Roble et al.* [1987]. Some differences exist, particularly in the E-region concentrations of NO^+ and O_2^+ during solar maximum, where variability in solar soft x-rays and the impact of photoelectrons are important.

4.4. Minor Neutral Constituents

Finally, Figure 7 shows the calculated global mean densities for the odd nitrogen family, $N(^4S)$, $N(^2D)$, and NO, at both solar minimum and maximum. Once again, at $Z = 3$ the concentration of $N(^2D)$, which depends strongly on N_2^+, shows a discontinuity where secondary ionization by photoelectrons artificially stops. The primary sources of NO are the reaction of $N(^2D)$ with O_2 at low altitudes and $N(^4S)$ with O_2 at higher altitudes. The second of these reactions, k_{13} in Table 1, is highly dependent on temperature. As a result, the shape of the NO
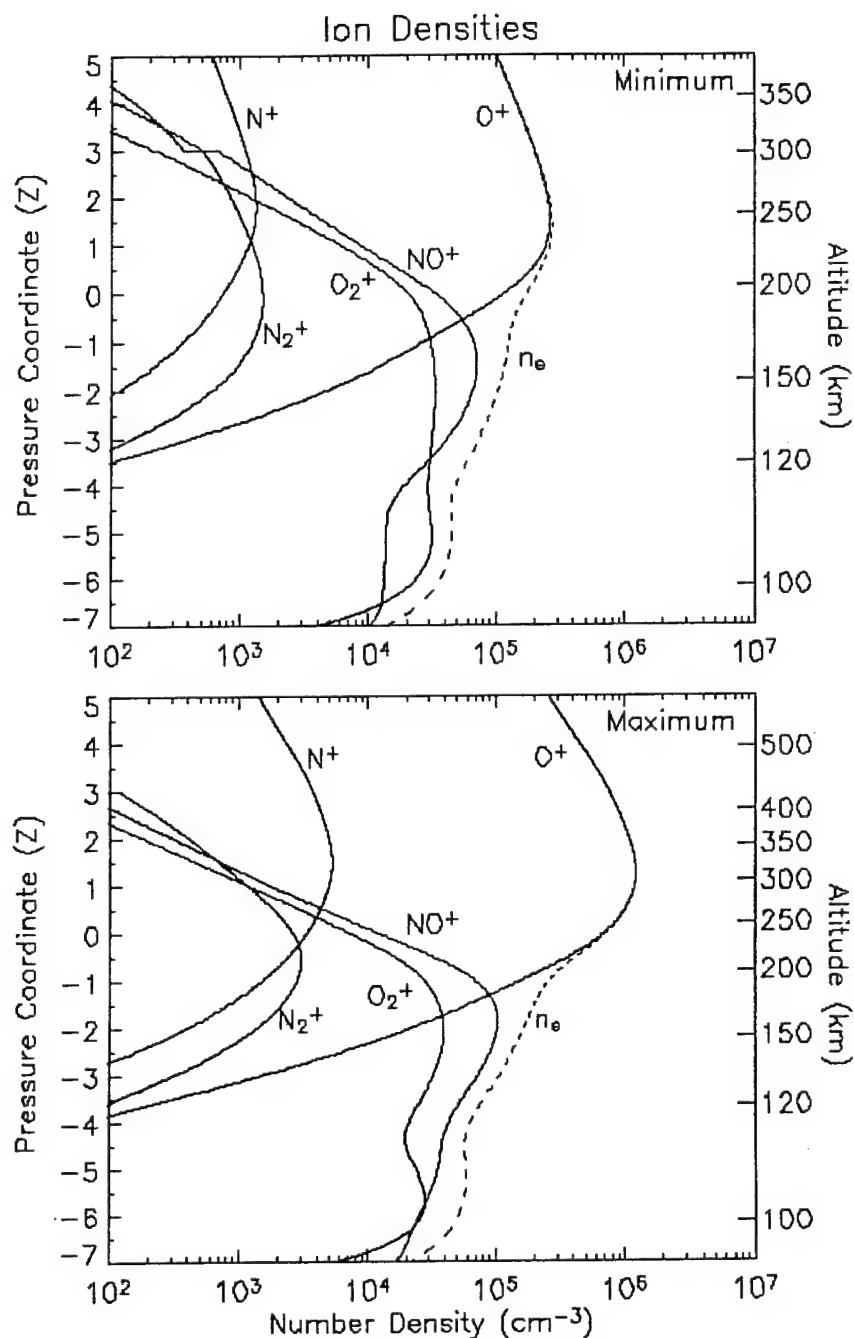
Figure 6. Global mean number density profiles for five ion species (O^+, NO^+, O_2^+, N^+, and N_2^+) and the electron density (n_e), calculated using the GAIT model. The top panel is for solar minimum ($P = 70$), and the bottom panel for solar maximum ($P = 230$) assuming quiet geomagnetic conditions ($Ap = 4$). The discontinuity observed in the NO^+ and N_2^+ profiles at $Z = 3$ corresponds to where the photoelectron calculation stops.
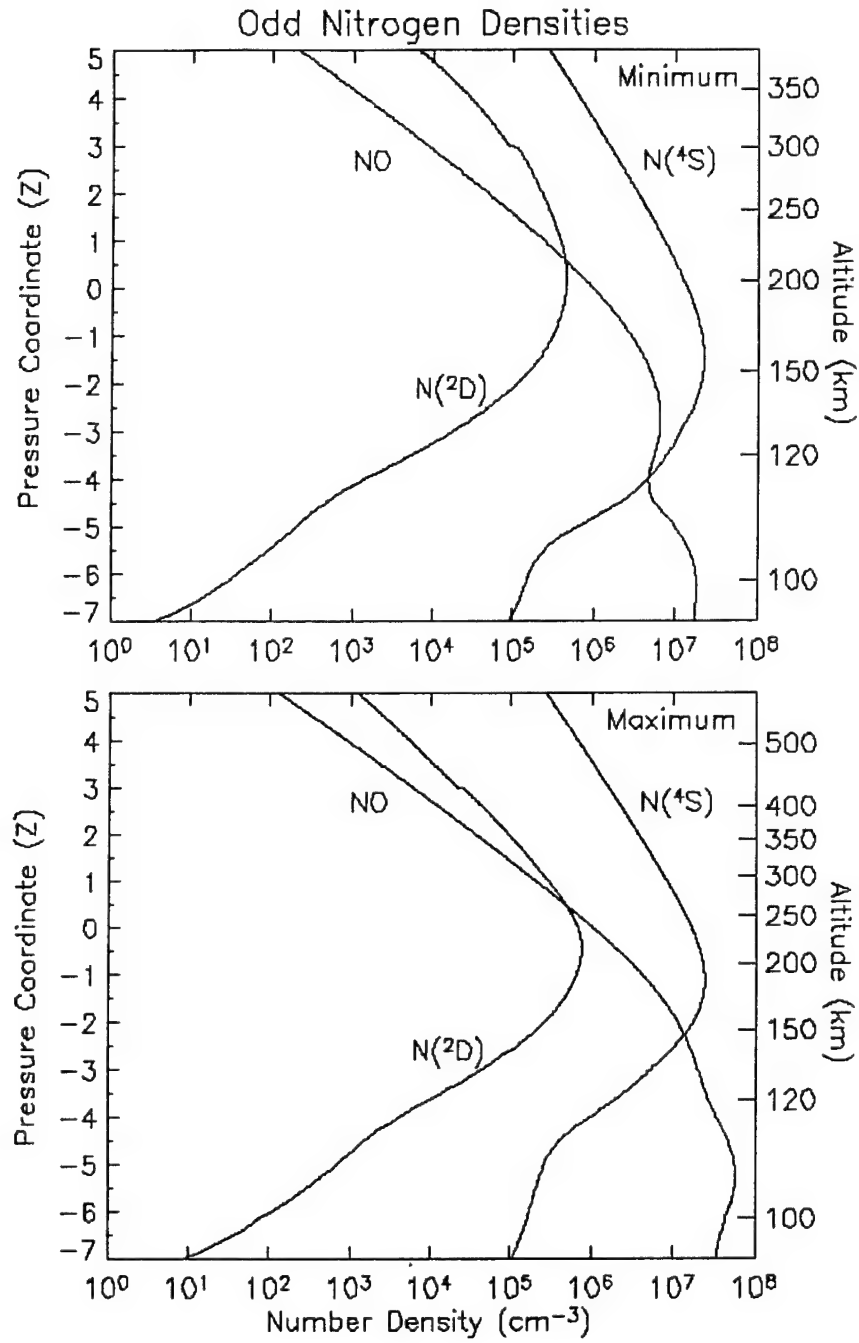
Figure 7. Global mean number density profiles for the odd nitrogen species (N(^{4}S), N(^{2}D), and NO), calculated using the GAIT model. The top panel is for solar minimum (P = 70), and the bottom panel for solar maximum (P = 230) assuming quiet geomagnetic conditions (Ap = 4). The discontinuity observed in the NO profile at Z = 3 corresponds to where the photoelectron calculation stops.

profile shows distinct differences between solar minimum and maximum at roughly Z = –4

(115 km). These changes relate directly to the neutral temperature; even a small increase in the

temperature at these altitudes, e.g. an additional 25 K caused by increasing the Joule heating rate

to 100 GW, removes the dip in NO at Z = –4.

4.5. Solar Cycle Variation of the Thermosphere and Ionosphere

Making use of the proxy, P, we can examine the response of the GAIT model across a range

of solar activity. Probably the best scalar indicator of the state of the thermosphere is the

exospheric temperature of the neutral gas. Figure 8 shows the calculated global mean exospheric

temperature ranging from solar minimum, P = 70, to solar maximum, P = 230, with global

average MSIS-90 results for comparison. We assumed quiet geomagnetic conditions (Ap = 4),

keeping the global Joule heating input fixed at 70 GW. The two models agree best at solar
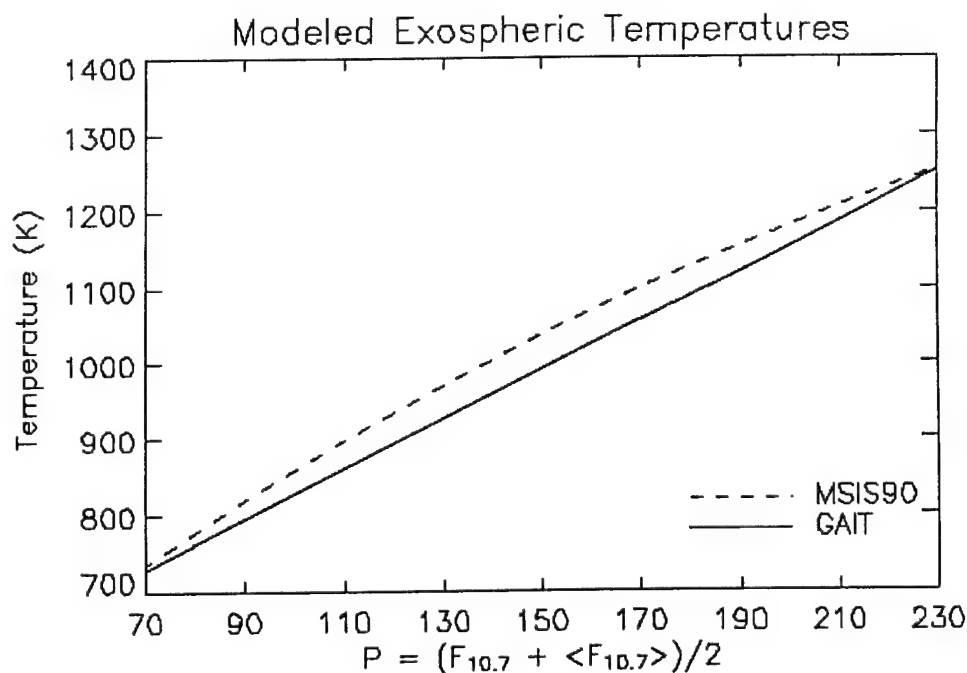
Figure 8. Model calculations of the global mean exospheric temperature as a function of the solar cycle, assuming quiet geomagnetic conditions (Ap = 4). The solid line corresponds to the GAIT model results and the dashed line to the MSIS-90 empirical model.

minimum and maximum, because these are the points we used to tune the GAIT model. In between, the MSIS-90 temperatures are higher, the greatest difference being 45 K or 4.6% at P = 150.

The exospheric temperatures calculated using the GAIT model shows a remarkable linearity across the normal range of solar activity (Figure 8). Since we have forced the solar irradiance, and hence the energy flux, to scale linearly as a function of P, the figure implies the GAIT exospheric temperature responds linearly with respect to the input energy over the range of normal solar cycle variation. On the other hand, the MSIS-90 exospheric temperatures are not linear with respect to P, showing instead a knee at roughly P = 150. Assuming the physical model is correct, and the thermosphere does respond linearly to the energy input, the MSIS-90 results imply the solar irradiance is not linear with P, in agreement with the work of *Balan et al.* [1994a; 1994b]. This suggests that to match the nonlinear MSIS-90 response better, we should adopt a nonlinear irradiance model. As we will discuss in section 5.1, sufficient uncertainties exist in key reaction rates and inputs that, should we modify the irradiance representation, we expect to be able to recalibrate the GAIT model to again match the empirical results.

In the ionosphere, the total electron content (TEC) is chosen as a similarly representative scalar quantity. Figure 9 displays the modeled global average TEC over the solar cycle. TEC depends, of course, on both the peak electron density (N_mF_2) as well as the slab thickness. N_mF_2 is found to increase nearly linearly over the course of the solar cycle. In pressure coordinates the slab thickness is approximately constant [*Rishbeth and Edwards*, 1989], which means it too increases linearly in absolute height, given a linear increase in neutral temperature. Convolving these two contributions results in a nonlinear, approximately quadratic increase to TEC. The actual variation of TEC deviates from this description slightly due to the nonlinear effect of T_e on N_mF_2 and slab thickness.
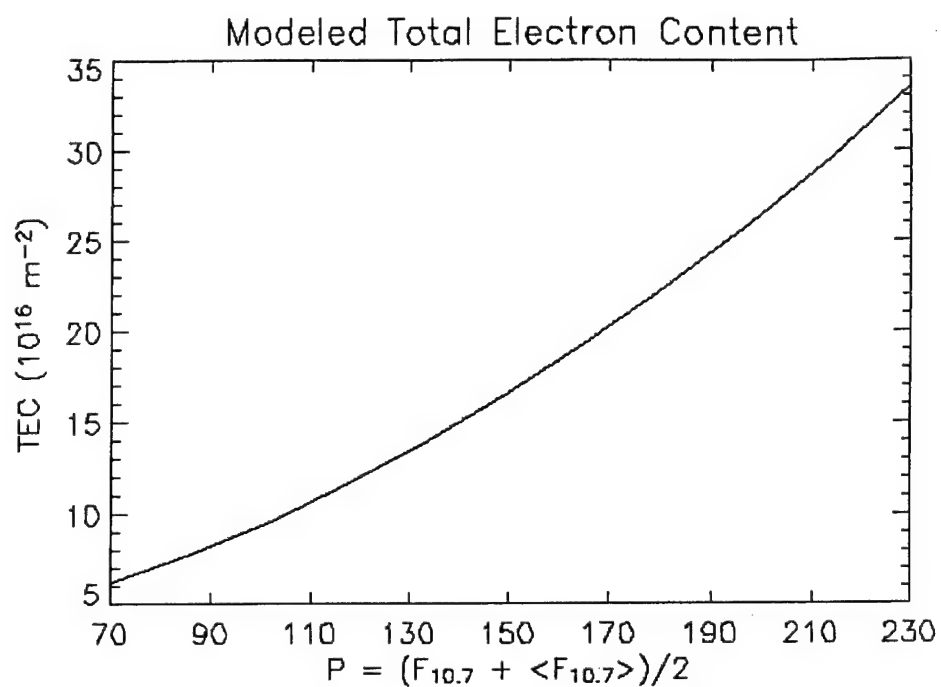
Figure 9. Model calculations of the total electron content as a function of the solar cycle, assuming quiet geomagnetic conditions (Ap = 4).

CHAPTER 5

MODEL SENSITIVITIES

5.1. Key Reaction Rates and Inputs

Gordiets et al. [1982] showed infrared radiative cooling by CO_2, NO, and O are the dominant sources of heat loss in the thermosphere. *Roble et al.* [1987] confirmed their relative importance by systematically removing each loss process and calculating the resulting increase in exospheric temperature. In the same vein, we now examine the GAIT model's sensitivity to these cooling processes by considering uncertainties in key reaction rates that drive them. We also examine other differences between the GAIT and earlier global average models [*Roble*, 1995; *Roble et al.*, 1987], such as the treatment of photoelectrons. Table 3 lists the percentage change that occurs to both the exospheric temperature and total electron content (TEC) as a result of these modifications. The reference values, using the standard inputs described previously, are listed as case (a).

5.1.1. CO_2 Cooling

Radiative cooling at 15 μm by CO_2 constitutes roughly 60% of the total heat loss in the thermosphere, therefore changes to this process can have a dramatic effect on the global average solution. The lower boundary condition for the CO_2 concentration is not well defined; but as described in section 3.7, the thermosphere is insensitive to fairly large changes in this parameter. More important to the resulting solution is the rate coefficient for excitation of bending vibration by collisions between CO_2 and O. The accepted rate has increased more than an order of magnitude in the past 20 years. *Dickinson* [1984] suggested a value of 2×10^{-13} cm^3 s^{-1}, while *Sharma and Wintersteiner* [1990] used satellite measurements to derive a room temperature value of 6×10^{-12} cm^3 s^{-1}. The only experimental results fall in the range of roughly 1×10^{-12} cm^3 s^{-1}

Table 3. Sensitivity of the Modeled Thermospheric Temperature and Total Electron Content to Changes in Key Reaction Rates and Inputs.

Case	% Difference from Reference			
	Exospheric Temperature (K)		Total Electron Content (10^{16} m^{-2})	
	Solar Minimum	Solar Maximum	Solar Minimum	Solar Maximum
(a) Reference Values	728	1250	6.2	33.4
(b) Reaction Rate for CO_2-O Excitation of Bending Vibration: $5.77 \times 10^{-14} \sqrt{T_n} \text{ cm}^3\text{s}^{-1}$	+11.9	+4.2	+23.2	+9.0
(c) Reaction Rate for $N(^4S)+NO$: $k_{14} = 3.4 \times 10^{-11} \text{ cm}^3\text{s}^{-1}$	+1.0	+3.4	+2.1	+2.7
(d) Reaction Rate for $N(^4S)+NO$: $k_{14} = 1.6 \times 10^{-10} \text{ Exp}[-460/T_n] \text{ cm}^3\text{s}^{-1}$	+2.9	+12.7	+3.7	+7.2
(e) Reaction Rate for $N(^4S)+O_2$: $k_{13} = 4.4 \times 10^{-12} \text{ Exp}[-3220/T_n] \text{ cm}^3\text{s}^{-1}$	+0.8	+6.0	+1.8	+2.7
(f) 40 GW of Global Joule Heating	−4.8	−3.3	−7.6	−4.2
(g) 100 GW of Global Joule Heating	+4.7	+3.1	+5.4	+2.1
(h) Electron Gas Heat Flux Boundary Condition: $3 \times 10^9 \text{ eV cm}^{-2} \text{ s}^{-1}$	−0.5	−1.8	−1.0	+2.4
(i) Secondary Ionization Scale Factor	−1.4	−2.9	−3.2	−8.3
(j) Parameterized Electron Gas Volume Heating	−1.3	−6.2	−3.4	−5.1

[*Pollock et al.*, 1993; *Shved et al.*, 1991]. Recently *Sharma and Roble* [2001] used a global mean model to argue for the Sharma and Wintersteiner value as a way to offset decreases to the total NO cooling rate caused by yet other updates to rate coefficients. The GAIT model uses the *Sharma and Wintersteiner* [1990] value as its standard rate; case (b) in Table 3 shows the sensitivity of the model to the experimental value for the CO_2-O excitation rate. At solar minimum the exospheric temperature increases by almost 12%, at solar maximum the percentage increase is less because cooling by NO is more effective.

5.1.2. NO Cooling

Emission at 5.3 μm by NO is an important thermospheric cooling mechanism, especially for high solar activity. The principal loss term for NO is the reaction $NO + N(^4S) \xrightarrow{k14} N_2 + O$; however, the temperature dependence of this reaction rate differs significantly in the literature [*Wennberg et al.*, 1994]. The GAIT model uses the value recommended by *JPL* [2003], $k_{14} = 2.1 \times 10^{-11} Exp[100/T_n] cm^3 s^{-1}$, but other recent nitric oxide models [*Bailey et al.*, 2002] use a constant value of 3.4×10^{-11} recommended by *Lee et al.* [1978], which is 16% larger than the JPL value at room temperature. At the other end of the spectrum, *Roble* [1995] used a value of $k_{14} = 1.6 \times 10^{-10} Exp[-460/T_n]$, which equals the *Lee et al.* [1978] value at room temperature, but has a completely different temperature dependence than the JPL value. Cases (c) and (d) in Table 3 examine the sensitivity of the GAIT model to these different reaction rates. In both examples, the changes lead to increased exospheric temperatures and TEC. As expected, the largest variation occurs at solar maximum with the *Roble* [1995] rate.

In the upper thermosphere, nitric oxide is produced via the reaction of $N(^4S) + O_2$. This reaction, k_{13} in Table 1, is highly temperature dependent, and for a given neutral temperature profile controls the crossover point between the NO and $N(^4S)$ concentrations (see Figure 7). The GAIT model uses the reaction rate most recently recommended by *JPL* [2003], but some nitric oxide models [*Bailey et al.*, 2002] are using the older recommendation of *Clark and Wayne* [1970], $k_{13} = 4.4 \times 10^{-12} Exp[-3220/T_n] cm^3 s^{-1}$. This rate results in smaller NO concentrations at all altitudes, hence less 5.3 μm cooling and greater exospheric temperatures. As shown in case (e) of Table 3, the impact is again largest at solar maximum.

5.1.3. Joule Heating

Roble et al. [1987] suggested a global Joule heat input of 70 GW was consistent with geomagnetic quiet conditions, and that is the value currently used in the GAIT model. To gauge

the impact of this term, we varied the total Joule heating between 40 and 100 GW. Cases (f) and (g) in Table 3 show the resulting change in the exospheric temperature is less than 5%, the biggest difference being at solar minimum when Joule heating is a larger fraction of the total heat input. While *Roble et al.* [1987] and *Roble and Emery* [1983] showed this auroral heat source is necessary to bring the global average temperatures in agreement with the empirical MSIS results, this sensitivity study emphasizes the Joule heating component in no way controls the solution.

5.1.4. Heat Flux Boundary Condition

The GAIT model uses a parameterization based on the electron temperature model of *Titheridge* [1998] to specify the heat flux boundary condition for the electron gas. This parameterization results in values of 4.4 and 7.2×10^9 eV cm^{-2} s^{-1} at solar minimum and maximum, respectively. The earlier model of *Roble et al.* [1987] used a fixed heat flux of 3×10^9 eV cm^{-2} s^{-1}. As shown in case (h), the sensitivity of the neutral gas exospheric temperature to this boundary condition is small, although the electron temperature is much more sensitive. At the upper boundary T_e decreases 10 and 23% at solar minimum and maximum using the lower fixed heat flux. As described previously, lower temperatures for the electron and hence ion gas are responsible for the observed increase in solar maximum TEC.

5.1.5. Secondary Ionization by Photoelectrons

Section 3.8 describes how the GAIT model uses an approximate method to calculate the secondary ionization caused by photoelectrons. The earlier global average models [*Roble*, 1995; *Roble et al.*, 1987] used a fixed-scale factor of 1.3 to approximate this effect. Case (i) in Table 3 demonstrates the resulting change to the GAIT output if we employ this simple scale factor. The exospheric temperature decreases by less than 3%, while the solar maximum TEC decreases about 8%.

5.1.6. Photoelectron Heating of Thermal Electrons

The approximate photoelectron calculation is also used to specify the thermal electron volume heating rate. As noted in section 3.8, the peak heating rate calculated by GAIT is roughly 40% higher than parameterized values used in the earlier global average models [*Roble*, 1995; *Roble et al.*, 1987], which results in higher electron temperatures. Case (j) in Table 3 shows the impact of using the parameterized heating rate is only 5 to 6% at solar maximum and less at solar minimum, when lower electron densities decrease the coupling between T_e and T_n.

Of all the examples shown in Table 3, none changed the exospheric temperature by more than 13%, or the TEC by more than 24%. We therefore assert the model is robust over the normal range of solar cycle variability, and the results determined primarily by the solar irradiance. For this reason, we next examine the model's sensitivity to uncertainty in the solar EUV irradiance.

5.2. Sensitivity to EUV Representation

While the GAIT model considers the solar irradiance from 3-360 nm, not all wavelengths are as well understood as others. As depicted in Figure 2, the solar cycle variability of wavelengths longer 120 nm is relatively small, especially when compared to the shorter EUV wavelengths. Extensive satellite measurements of these longer wavelengths have also established the absolute scale to the point that two different UV irradiance models [*Lean et al.*, 1997; *Woods and Rottman*, 2002] vary by less than 10% at all wavelengths (120-360 nm) over the course of the solar cycle, and in most cases by less than 5%. By contrast, models of the EUV irradiance (3-105 nm) differ significantly in both absolute scale and solar cycle variability. The GAIT results described so far have relied solely on the VUV representation of the solar flux. We now describe three other EUV irradiance models and compare the response of the GAIT model to each.

Richards et al. [1994] developed a widely used empirical model, EUVAC. The model's absolute scale is based on the F74113 reference spectrum, which was measured during a rocket flight on April 23, 1974, and the solar cycle irradiance variation is specified by AE-E satellite

observations. *Richards et al.* [1994] doubled the F74113 photon fluxes below 25 nm in order to improve agreement between observed and modeled photoelectron spectra, and recent observations from the Student Nitric Oxide Explorer (SNOE) support this increase [*Bailey et al.*, 2000]. EUVAC uses the P index as its solar activity proxy, and, as we have done with the VUV model, assumes a linear variation with P across the solar cycle.

The Solar2000 (S2000) model is the most recent in a series of iterations by *Tobiska et al.* [2000]. S2000 incorporates measurements made by multiple satellite and rocket measurements, including the AE-E observations, to specify both the reference spectrum and solar variability. The model is updated regularly to include the latest measurements, and the work here uses version 2.21. The daily F10.7 and a composite Lyman-α index are used as the principal solar activity proxies.

Whereas the previous models are empirical, *Warren et al.* [2001] have used a different approach to create the NRLEUV model. Measurements of the EUV emission from specific solar structures (quiet Sun, active regions, network, coronal holes) and the fractional solar disk coverage of these features is used to compute the EUV irradiance. The solar minimum irradiance, which establishes the absolute scale, is calculated by integrating the local quiet Sun emission over the entire disk. At other times, the irradiance is adjusted by including the presence of additional features. A parameterized version of the model uses F10.7, <F10.7>, and an index based on the Magnesium II core-to-wing ratio as proxies to solar activity.

Because the EUVAC model uses the P index as its solar activity proxy, it was easily incorporated into the GAIT model. In order to accommodate the NRLEUV and S2000 models, we modified them to use the P index. To do this, we first created representative solar minimum and maximum spectra for each by averaging 30 days of model output covering the months of September 1986 and November 1989. We then generated a simple linear fit using the average P index for these two months: September 1986, P = 70, and November 1989, P = 221. The

EUVAC and NRLEUV models do not extend below 5 nm, therefore the VUV model was used to fill the irradiance values between 3 and 5 nm.

Lean et al. [2003] conducted an extensive comparison between NRLEUV, EUVAC, and an earlier version of S2000 (v1.15). One of the main conclusions they reached was the NRLEUV model predicted overall lower irradiances and a smaller solar cycle variability in the EUV than the other empirical models. A comparison of the total EUV (3-105 nm) energy flux predicted by each of the four irradiance models is given in Figure 10. Since each irradiance model has been fit linearly between solar minimum and maximum, the total energy flux varies linearly with P as well. As expected from the *Lean et al.* [2003] results, the NRLEUV model
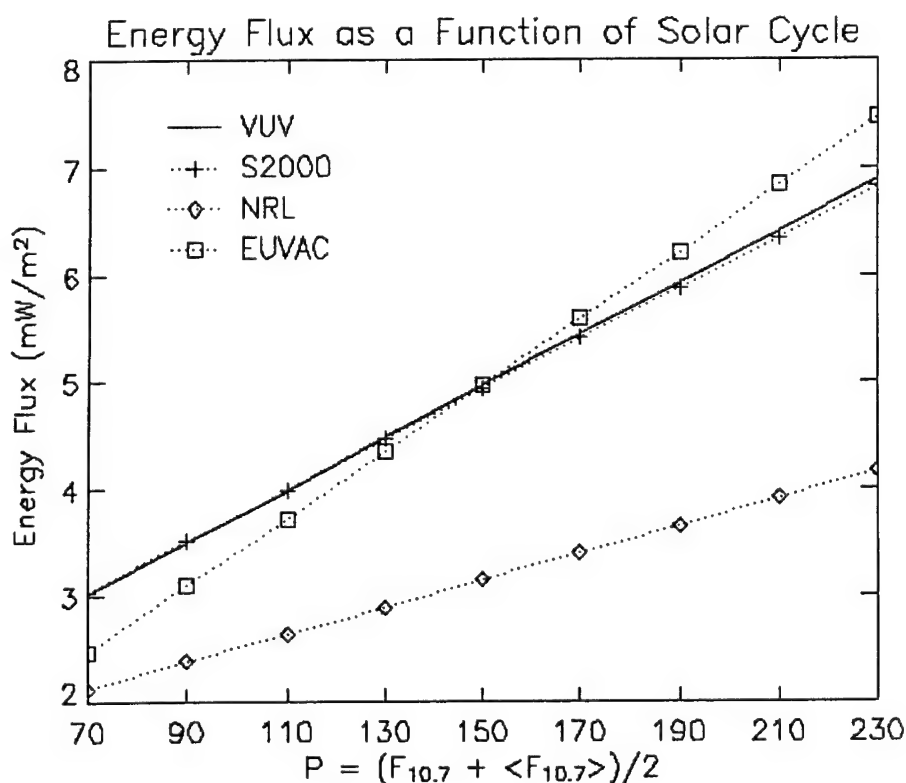
Figure 10. A comparison of the total EUV energy flux (3-105 nm) as a function of solar activity, calculated using four different irradiance models. The solid line corresponds to the standard input, the VUV model [*Woods and Rottman*, 2002], while the dotted lines with cross, diamond, and square symbols correspond to the Solar 2000 version 2.21 [*Tobiska et al.*, 2000], NRLEUV [*Warren et al.*, 2001], and EUVAC [*Richards et al.*, 1994] models, respectively.

returns the lowest absolute energy flux, 2.12 mW/m^2 at solar minimum, as well as the

lowest solar cycle variation, a factor of 1.97. The EUVAC model predicts the largest variation, a

factor of 3.02, starting from 2.47 mW/m^2 at solar minimum. The total energy flux for the VUV

and S2000 models are nearly identical, 3.02 and 3.04 mW/m^2 at solar minimum and 6.90 and

6.83 mW/m^2 at maximum, although we will see spectral differences between the two result in

significant differences in the thermosphere.

The GAIT model was run for low, moderate, and high solar activity (P = 70, 150, and 230),

using each of the four EUV irradiance representations as input, while keeping the other

parameters fixed. In all cases, the VUV model was used to specify the longer UV wavelengths.

The resulting exospheric temperatures are plotted in Figure 11 as a function of the total EUV

energy flux (3-105 nm). In the figure, each of the four irradiance models are identified by a

different symbol: VUV (circle), S2000 (triangle), NRLEUV (diamond), and EUVAC (square).

Each symbol is also color coded according to the solar activity level: white (low, P = 70), grey

(moderate, P = 150), and black (high, P = 230). The solid line represents a linear least squares fit

to the results. Regardless of the irradiance representation, all of the temperatures are fairly well

clustered around the solid line (R^2 = 0.96). In fact, the modeled exospheric temperature responds

linearly for each of the four irradiance representations, although the slope varies due to the

spectral differences between them. For example, even though the VUV and S2000 models

predict essentially the same total energy flux, the S2000 exospheric temperatures are 8% smaller

at solar minimum (P = 70) and 12% smaller at maximum (P = 230). Although for clarity they are

not shown in the figure, temperatures calculated with the early EUV representations used by

Roble et al. [1987] also fall within 5% of the solid line.

The NRLEUV results are particularly striking and the impact of its smaller dynamic range is

readily apparent. As Figure 11 illustrates, the total energy input predicted by NRLEUV for high

solar activity (P = 230) is less than that predicted by the other three models for moderate activity

Modeled Exospheric Temperatures
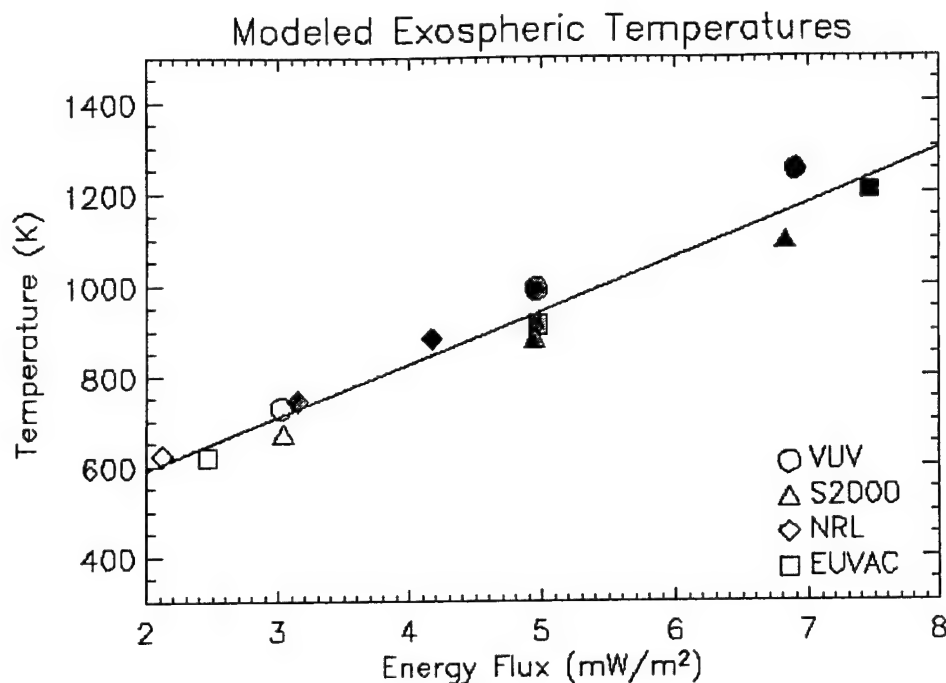
Figure 11. Modeled global mean exospheric temperatures as a function of the EUV energy flux (3-105 nm), calculated using four different irradiance models. The circle, triangle, diamond, and square symbols correspond to the VUV [*Woods and Rottman*, 2002], Solar 2000 version 2.21 [*Tobiska et al.*, 2000], NRLEUV [*Warren et al.*, 2001], and EUVAC [*Richards et al.*, 1994] models, respectively. Open symbols represent solar minimum conditions (P = 70), black filled symbols solar maximum conditions (P = 230), and grey filled symbols moderate solar conditions (P = 150). The solid line indicates a least squares fit to the results.

(P = 150). The exospheric temperatures are correspondingly low. Using NRLEUV the model

returns an unphysical solar maximum temperature of 883 K, 30% lower than the MSIS-90 model.

Another conclusion to be drawn from Figure 11 is that key reaction rates and inputs, such as

those discussed in section 5.1. must be tuned to a specific irradiance representation in order for

the calculated exospheric temperatures to match the empirical MSIS-90 results. Using the

standard reaction rates and inputs described in Chapter 3, only the VUV model predicts

exospheric temperatures within 10% of MSIS-90. All of the chemical reaction rates have

associated uncertainty, so in principle there are an infinite number of tuning possibilities.

However, by simply adjusting some of the key rates listed in Table 3, exospheric temperatures

calculated using both the S2000 and EUVAC models can be easily brought within 2% of the

empirical model at both solar minimum and maximum. For example, by adopting the

NO + N(^{4}S) loss rate used by *Roble* [1995], 1.6×10^{-11} Exp$[-460/T_n]$ cm^{3}s^{-1}, and reducing the

CO_2-O excitation rate to 3×10^{-12} cm^3 s^{-1} at 300 K [*Bougher et al.*, 1994], exospheric

temperatures calculated with the S2000 irradiance model fall within 1% of the MSIS-90 values.

However, we could find no combination of reasonable adjustments sufficient to bring the

NRLEUV output in line with MSIS-90. Even after modifying all of the reaction rates and inputs

listed in Table 3 to give the highest temperatures, the NRLEUV solar maximum temperature only

reached 1148 K, still 8% less than the MSIS-90 value. Furthermore, these changes caused the

solar minimum temperature to increase to 802 K, 9% larger than the empirical value. Barring

significant changes to the accepted reaction rates or new nonlinear heat sources, the dynamic

range of the NRLEUV model is apparently not large enough to support the observed solar cycle

temperature variation. The model's authors have acknowledged that NRLEUV appears to

underestimate variability, especially in the range 70-105 nm, and believe this could account for

the problems described above [*Lean*, private communication, 2004].

CHAPTER 6

MAUNDER MINIMUM

6.1. Sunspot Cycle

The P index described in section 3.4, and used to specify the solar irradiance, is based on the standard activity proxy, F10.7, which is a measure of the solar radio emission at 10.7 cm. *Covington* [1947] and others initially uncovered the relationship between solar radio emissions and sunspots. These emissions, particularly F10.7, proved to be useful indicators of solar activity levels, and have been used ever since as objective proxies. Although objective and reliable, the F10.7 record includes only a few solar cycles, during which time the Sun has remained remarkably consistent in its 11-year variability. The written sunspot record, however, extends back to nearly 165 B.C., primarily through the Chinese who considered such solar blemishes as portents and omens [*Wittmann and Xu*, 1987]. With the invention of the telescope, European scientists began to keep detailed records of both the number and location of sunspots that has continued to this day.

Hoyt and Schatten [1998a; 1998b] reviewed the available sunspot records and constructed an internally self-consistent time series of the sunspot group number, Rg, that extends back to 1610. Figure 12 displays the annual mean group number from 1610 to 1995. It is immediately apparent that the normal 11-year solar cycle measured during the space age is in fact only part of a larger pattern of activity. Virtually no sunspots were observed during the extended period from roughly 1645-1715, now known as the Maunder Minimum. It is important to note this period was characterized by reports of no sunspots, rather than just an absence of reports. From roughly 1800-1830, the sunspot counts were again low and the cycle lengthened; it has even been suggested the Sun skipped a cycle during this so-called Dalton Minimum [*Usoskin et al.*, 2001]. Earlier, less reliable sunspot records hint at other minima between 600 and 800 A.D. (the

Mean Group Sunspot Number

Maunder Minimum

Dalton Minimum
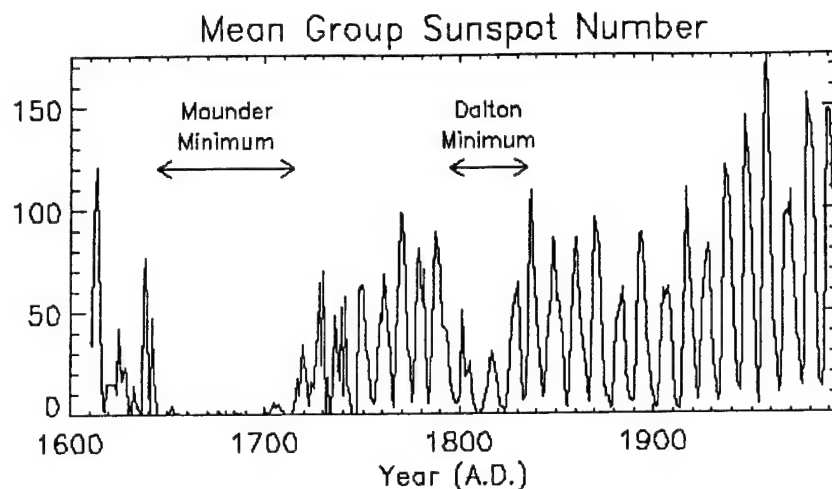
Figure 12. A time-series of the mean annual group sunspot number (Rg), covering the period 1610 to 1995 A.D.

Medieval Minimum) and 1460 and 1550 A.D. (the Spörer Minimum) [*Wittmann and Xu,* 1987], as well as a Grand Maximum between 1100 and 1250 A.D. [*Eddy,* 1976]. The regular 11-year variability experienced during the modern era thus appears to constitute just one facet of a much more complex pattern.

One could argue the low sunspot number observed during Maunder Minimum represented merely an extended solar minimum, with similar emission levels. However, additional, independent lines of evidence suggest the solar output during this time was indeed dramatically different. Cosmogenic isotopes such as ^{14}C and ^{10}Be are formed via the interaction between cosmic ray protons and the Earth's atmosphere. Long-term records of the ^{10}Be production rate can be inferred through analysis of ice cores [*Webber and Higbie,* 2003], and in the case of ^{14}C, tree rings [*Eddy,* 1976]. As solar modulation is the dominant source of variability in the galactic cosmic ray flux reaching the Earth, this record gives an independent measure of the level of solar activity.

Webber and Higbie [2003] recently reported on the systematic variation of ^{10}Be production extending back through the Maunder Minimum period. They found the normal 11-year solar cycle modulation of cosmic rays to result in solar minimum production rates that are roughly a

factor of 1.5-2.0 larger than solar maximum. However, the [10]Be production rate calculated for the Maunder Minimum period was even higher than contemporary minima, by a factor of ~1.8-2.0, consistent with negligible solar modulation of the cosmic rays.

A second line of evidence involves astronomical measurements of Sun-like stars. Chromospheric emissions from Sun-like stars exhibit a broader range of variability than is seen in the Sun's contemporary cycles [*Baliunas and Jastrow*, 1990; *Radick*, 2003; *Radick et al.*, 1998; *White et al.*, 1992]. A distribution of chromospheric emissions from the contemporary Sun mimics only the high-activity tail of the Sun-like star distribution. *Baliunas and Jastrow* [1990] suggest the low-activity end of the distribution arises from stars that have entered a non-cycling state. *Lean et al.* [2001] further argued that during the Maunder Minimum, the Sun entered such a non-cycling state. Using the group sunspot number as a proxy, Lean et al. created a solar chromospheric activity index composed of an 11-year cycle superimposed on top of a varying background component, such that the reconstructed emission distribution approximated the Sun-like star distribution of *Baliunas and Jastrow* [1990]. Over the course of a typical modern solar cycle, the *Lean et al.* [2001] chromospheric index increased by roughly a factor of 1.2, while from Maunder Minimum to modern minima the predicted increase was an additional factor of ~1.2. These results are similar to the variation found in cosmogenic isotopes. Taken together, they lead to the conclusion solar activity during the Maunder Minimum period was dramatically lower than modern minima.

6.2. The Maunder Minimum Irradiance

EUV and UV photons originate from a range of altitudes in the solar atmosphere, as well as through different physical processes. Electronic transitions, such as the Lyman series in hydrogen, result in individual line emission, while the capture of free electrons produces a continuum emission corresponding to the electron energy distribution. Given the ionization energy, and assuming a solar density and temperature model, one can use the Saha equation to

estimate the formation temperature of the various ion species, and thus the altitude from which the photons originate. In general, shorter wavelength photons originate in the hot solar corona, while the cooler chromosphere is responsible for longer EUV and UV photons. Variability in the solar atmosphere increases with altitude, such that coronal emission lines show the largest modulation, while line and continuum emission from the chromosphere are much less variable.

Based on the earlier work of *Lean et al.* [2001], *Lean* [2004] suggested a reasonable representation of the Maunder Minimum irradiance could be obtained by linearly reducing the individual emission components from normal minimum values by an amount between one half and a full solar cycle variation. Using this approach, many of the highly variable coronal lines become negative and are set to zero. The estimated Maunder Minimum irradiance is then dominated by appropriately reduced chromospheric lines and continuum.

In terms of the P index introduced in section 3.4, the *Lean* [2004] recommendation puts Maunder Minimum between P = −10 and P = −90. However, the P index is a physical quantity tied to the 10.7 cm radio flux, and therefore loses meaning for negative values. To avoid confusion, we instead define a solar cycle factor S, with S = 0 identifying normal solar minimum (P = 70) and S = 1 being solar maximum (P = 230). Using this index and the *Lean* [2004] suggestion, we assume Maunder Minimum levels to reside somewhere between S = −0.5 and S = −1. The irradiance, $I(\lambda)$, of the individual components is thus specified as a function of S by

$$I(\lambda) = I_{S=0}(\lambda)[(\text{var}(\lambda)-1)S+1], \tag{13}$$

where λ is the wavelength, $I_{S=0}$ the solar minimum reference irradiance, and var(λ) the solar minimum to maximum variability factor.

The component approach to building a representative spectrum requires high spectral resolution, one Angstrom or better, in order to separate the individual emission lines. In addition, we must be able to scale the line and continuum emission separately. Of the EUV irradiance

models described previously in section 5.2, only the NRLEUV model satisfies these requirements. However, as we have shown, the NRLEUV model lacks the dynamic range necessary to reproduce the expected solar cycle variation in T_n, and so it is assumed to also underestimate the irradiance decreases that occur approaching Maunder Minimum. The NRLEUV model is therefore used to investigate the sensitivity to coarser approximations; the results can then be applied to the three other empirical EUV models.

The resolution of the empirical VUV, S2000, and EUVAC models is no better than 1-nm, and there is no provision to separate line from continuum emission. We therefore need to determine the impact of scaling the irradiance to Maunder Minimum (S = −1) levels on such a coarse grid. Figure 13 compares representative EUV spectra, calculated using the NRLEUV model for S = −1,
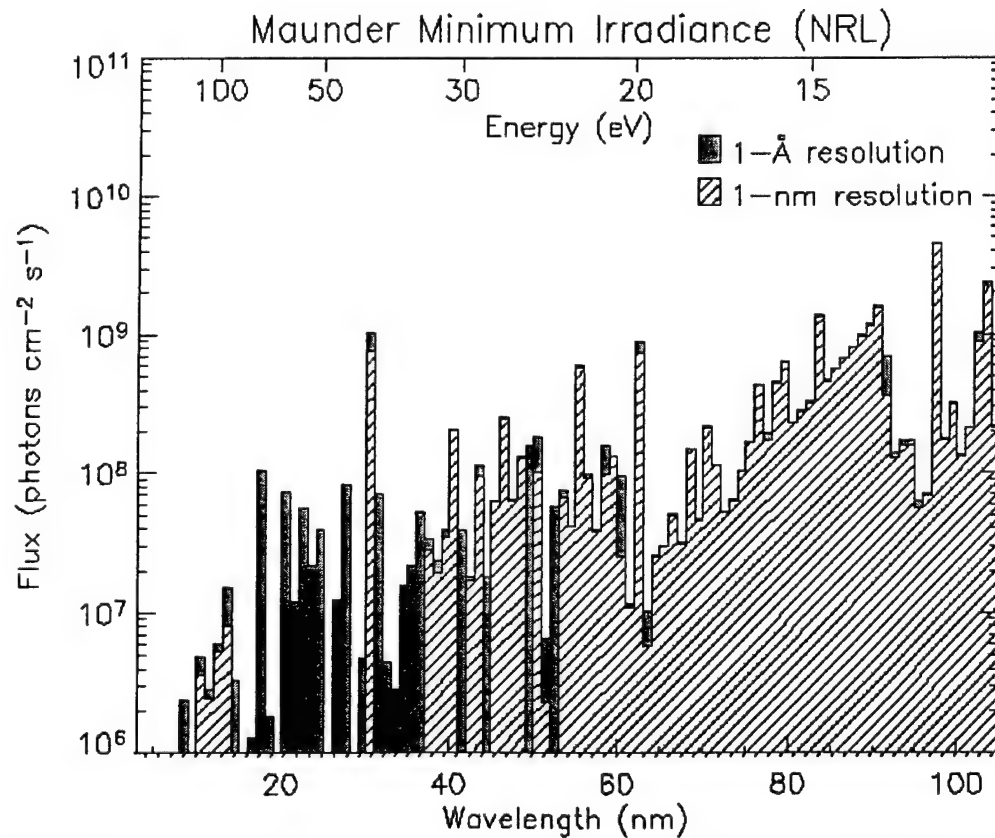
Figure 13. A comparison of the approximated Maunder Minimum irradiance (S = −1), calculated with the NRLEUV model using both high and low resolution.

at both high (1-Å) and low (1-nm) resolution. For the high-resolution representation, the line and continuum contributions were scaled separately and then combined, whereas the low-resolution approach simply scaled the total flux in each 1-nm bin.

Longward of 60 nm, the two approaches yield essentially the same flux. Chromospheric emission dominates these wavelengths, and therefore separating out the coronal contribution is not important. Shortward of 40 nm, the reference flux is dominated by highly variable coronal lines, which essentially all disappear at $S = -1$. Using the coarse approximation, this results in an extended band, ~15-35 nm, over which the irradiance is essentially set to zero. At high resolution, however, the less variable chromospheric lines and continua remain.

Comparing the two spectra for $S = -1$, the high-resolution approach results in a 10% greater EUV photon flux and 19% greater energy flux. At $S = -0.5$ the differences are 6 and 11% respectively. The sensitivity of the coupled thermosphere/ionosphere is comparable; TEC values are uniformly low, and differ by less than 19% between the coarse and high-resolution approaches. There is less than a 3% difference in the modeled exospheric temperature, reflecting the fact that at these low S values, the UV contribution to global heating dominates over the EUV. More importantly for our later discussion, a comparison of the various ion profiles shows no significant morphological differences between the high-resolution and coarse approximations.

Based on these results, we believe a simple linear scaling of the 1-nm empirical irradiance models can be used to adequately represent Maunder Minimum type irradiances. As before, the VUV model is used as the standard irradiance input. Figure 14 shows the same VUV reference spectrum as in Figure 2, with a representative Maunder Minimum ($S = -1$) spectrum superimposed. The solar cycle variability factor, which was previously used to scale between solar minimum and maximum, is now used to reduce the reference spectrum according to equation (13). As shown in the figure, wavelengths with a variability factor greater than two (dotted line) are zeroed when $S = -1$.
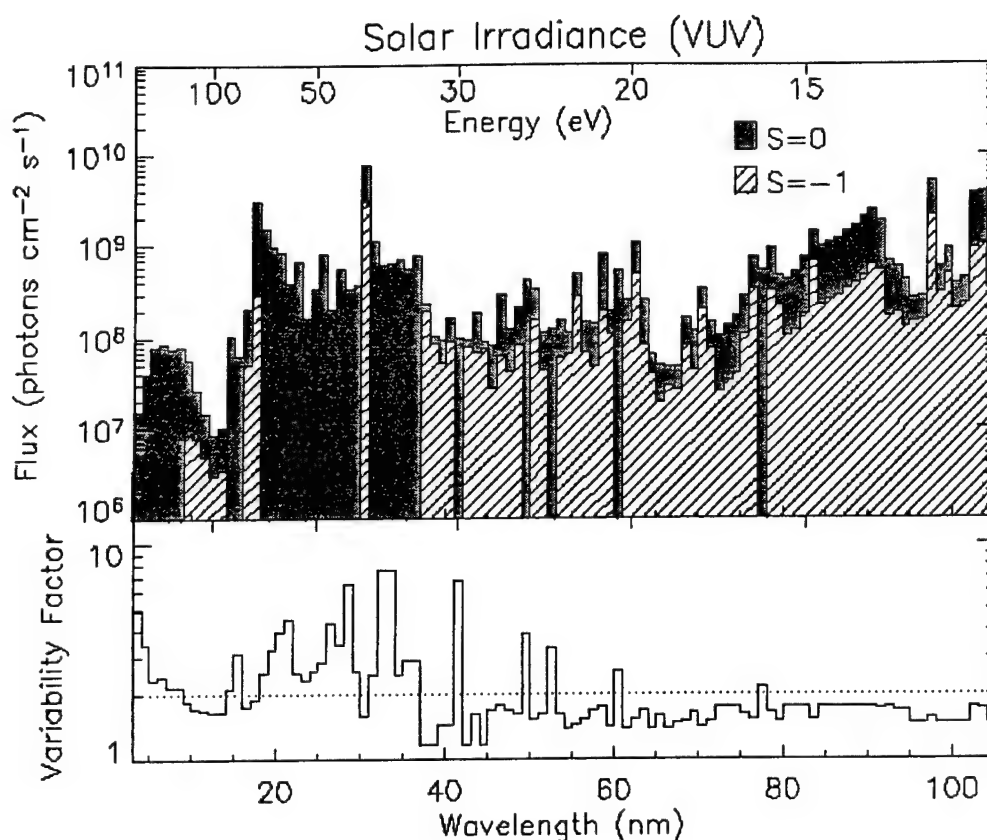
Figure 14. The VUV irradiance model [*Woods and Rottman*, 2002] used to specify the solar input. The top panel shows both the solar minimum reference spectrum (S = 0) as well as a representative Maunder Minimum (S = −1) spectrum. The bottom panel details the solar cycle variability factor used to scale the reference spectrum. Wavelengths with a variability greater than two (dotted line) are zeroed in the S = −1 spectrum.

6.3. GAIT Model Changes

One change is made to the GAIT model described in Chapter 3. Previously, the electron temperature upper boundary condition was specified by a parameterization of the heat flux calculated from the empirical *Titheridge* [1998] model (section 3.2). This parameterization relied on the P index, and could result in unphysical values for very low solar activity levels. In the updated scheme, the heat flux boundary condition is instead tied to the photoelectron energy flux, self-consistently calculated in the model. This approach assumes the majority of the heat flux comes from the conjugate hemisphere rather than the magnetosphere. The heat flux boundary

condition is set equal to $1/10^{th}$ of the photoelectron energy flux calculated at $Z = 3$. Over the normal solar cycle range, this approximation reproduces the original Titheridge parameterization to within 10%, with the added benefit the boundary condition is now self-consistent with the input solar spectrum.

In accordance with the arguments of section 3.3, we continue to assume the lower atmosphere is essentially unchanged by the irradiance changes described above, and we can therefore keep the lower boundary conditions fixed. The rationale for this assumption is that the variable component of the solar spectrum is absorbed primarily in the thermosphere, with little coupling between layers.

6.4. Maunder Minimum Results

The GAIT model was run using an S index ranging between $S = -1$ and 1, where $S = 0$ represents normal minimum ($P = 70$), $S = 1$ maximum ($P = 230$), and Maunder Minimum is assumed to fall between $S = -0.5$ and -1. As expected, thermospheric temperatures continue to fall with decreasing solar activity. At $S = -0.5$, the global mean exospheric neutral gas temperature is calculated to be 560 K, a decrease of 24% from normal minimum. By $S = -1$, the temperature is down to 490 K.

The most distinguishing characteristic of the Maunder Minimum result is found in the electron density. Figure 15 shows a contour plot of the computed global mean electron density as a function of both pressure and solar activity. A dashed line identifies the pressure of the peak electron density. Over the normal solar cycle range, the peak electron density remains essentially constant at a pressure of $Z = 1$. This is consistent with our understanding of how the F-layer resides on a constant pressure surface [*Rishbeth and Edwards*, 1989]. Between $S = -0.2$ and $S = -0.4$, the peak electron density drops to approximately $Z = -1$, signaling a major morphological
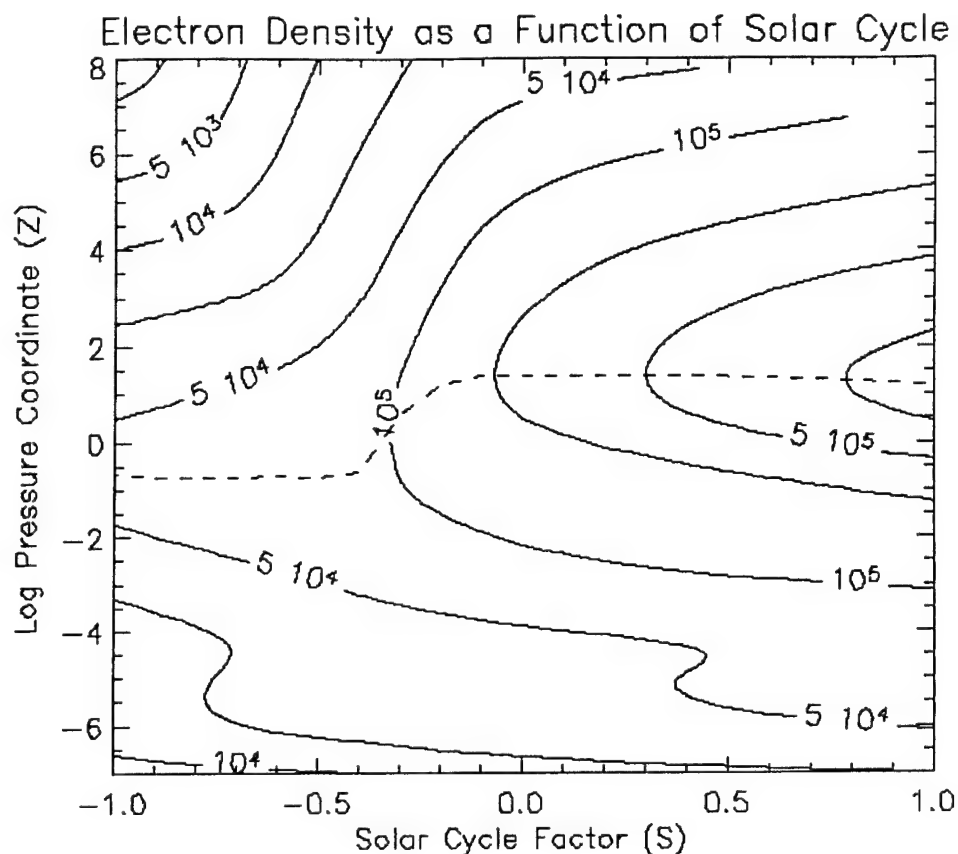
Figure 15. A contour plot of the global mean electron density (cm^{-3}), calculated as a function of the log pressure altitude and solar cycle factor. The dashed line indicates the pressure of the peak electron density.

change in the structure of the ionosphere. After the transition, the peak electron density remains fixed on the new, lower pressure surface.

The source of the transition is readily apparent in the ion density profiles. Figure 16 presents a comparison of the ion and electron density profiles for three levels of solar activity, S = 0.0, –0.5, and –1.0. As the level of solar activity decreases, we see O$^+$, which comprises the majority of the ionospheric F$_2$ layer, is preferentially decreased versus the other ions. By S = –0.5, O$^+$ is no longer the dominant ion, and the peak electron density has shifted to coincide with the maximum NO$^+$ density, at a lower altitude. The trend continues for even lower levels of activity, such that at S = –1.0, the O$^+$ density is lower than N$_2$$^+$, which is typically considered a

Figure 16. Ion and electron (dashed lines) global mean number densities, calculated for three different levels of solar activity. The top panel displays the densities computed under normal solar minimum conditions (S = 0.0); the middle and lower panels reflect the results for S = –0.5 and S = –1.0, respectively.

minor ion. Thus Figures 15 and 16 reveal a major morphological change in the ionosphere

in which molecular ions, specifically NO^+, come to dominate over atomic O^+ in the F-region. We

will refer to such a state as a Maunder Minimum ionosphere.

Figure 17 further exposes the extent to which the ion concentrations decrease. This figure

shows the peak concentrations of the three major ions (O^+, NO^+, and O_2^+) as a function of the

solar cycle factor S. The peak electron density is also plotted, indicating the transition from an O^+

dominated ionosphere to a molecular one. While the molecular ions display a relatively steady

decrease, the O^+ concentration falls dramatically.

Investigations into the cause of this dramatic fall reveal a simultaneous decrease in

production and increase in loss. Reductions in the EUV photon flux obviously decrease the net

ionization rate; however, the O^+ production rate is further diminished due to a concurrent

decrease in the neutral O concentration. Recall every ionization results in the eventual

dissociation of an O_2 molecule [*Stolarski*, 1976]. So as the total ionization rate decreases, so does

Figure 17. Peak concentrations of the three major ions as a function of the solar cycle. A dotted line indicates the value of the peak electron density.

the production of O. Direct photolysis of O_2 is also reduced for lower values of S. With less O available, the O^+ production rate decreases faster than for the other species.

More important than the decrease in production, is the rapidly increasing loss rate. The principle loss mechanisms for O^+ involve chemical reactions with neutral N_2 and O_2. On a fixed pressure surface, the total gas concentration and temperature are inversely related; thus as the neutral temperature decreases, more N_2 and O_2 are available to react with O^+. On top of that, the rate coefficients for both of these reactions are roughly quadratic in temperature, increasing rapidly for low temperatures [*St.-Maurice and Torr*, 1978].

While Figure 17 details the value of the peak concentration for the major ions, a logical companion is the absolute altitude of these peak values as a function of the solar cycle factor. Figure 18 shows these altitudes, as well as that for the peak electron density over the range $S = -1$ to 1. The peak O^+ altitude, constant in pressure coordinates, drops linearly from about 310 km at $S = 1$ to $\sim$180 km at $S = -1$. This corresponds to the similarly linear decrease in neutral gas

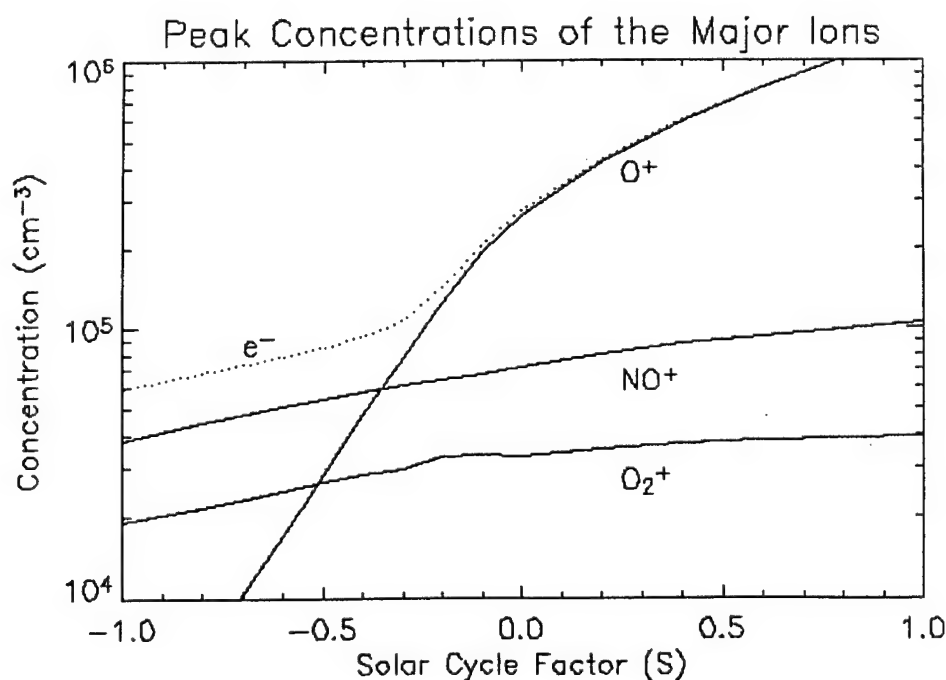**Figure 18.** Altitude of the peak concentrations of the three major ions as a function of the solar cycle. A dotted line indicates the altitude of the peak electron density.

temperature over this range. The molecular ions, on the other hand, are relatively stable in altitude. The transition to a Maunder Minimum ionosphere is again apparent between $S = -0.2$ and $S = -0.4$, as the peak electron density altitude, which mirrored O^+, drops to follow NO^+.

6.5. Impact of the Maunder Minimum Morphology

6.5.1. Neutral Mass Density

We can use the simple example of a satellite body in a circular orbit to examine the importance of variability in the global average mass density. The decay of satellite orbits are typically measured in terms of the rate of change of the orbital period, P, since the period is more accurately measured than the altitude [*Hargreaves*, 1992]. Assuming a circular orbit, P decreases at a rate given by

$$\frac{dP}{dt} = -\frac{3\pi C_D A r \rho}{m_s}.$$
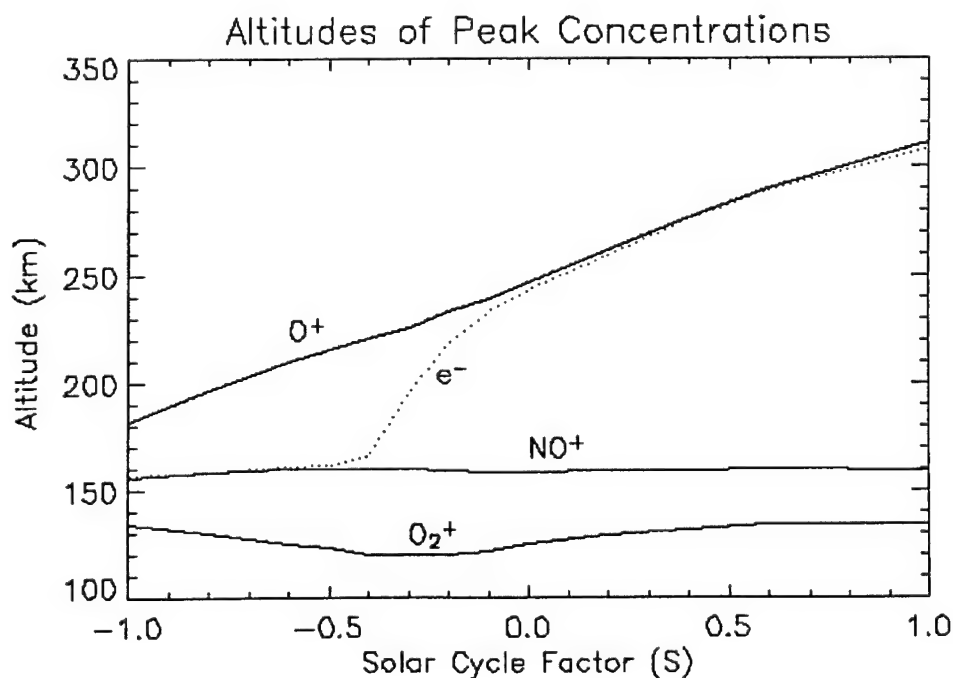
(14)

The satellite's surface area, A, mass, m_s, and drag coefficient, C_D, are combined into a ballistic coefficient. For a given ballistic coefficient, the rate of decrease at a given altitude r is then directly proportional to the local mass density, ρ.

Figure 19 displays a contour plot of the global mean mass density as a function of both altitude and solar cycle. At high altitudes, the mass density drops significantly with solar activity, corresponding to a decrease in the neutral gas temperature. For example, at 275 km, the mass density varies by a factor of three over the course of a normal solar cycle. The pace quickens as solar activity approaches Maunder Minimum conditions. Lowering the activity index to $S = -0.5$ decreases the mass density by a factor of five from normal solar minimum, and by $S = -1$ the density is 30 times lower than the solar minimum value. Spacecraft in low Earth orbit would therefore experience significantly less drag during a Maunder Minimum epoch.
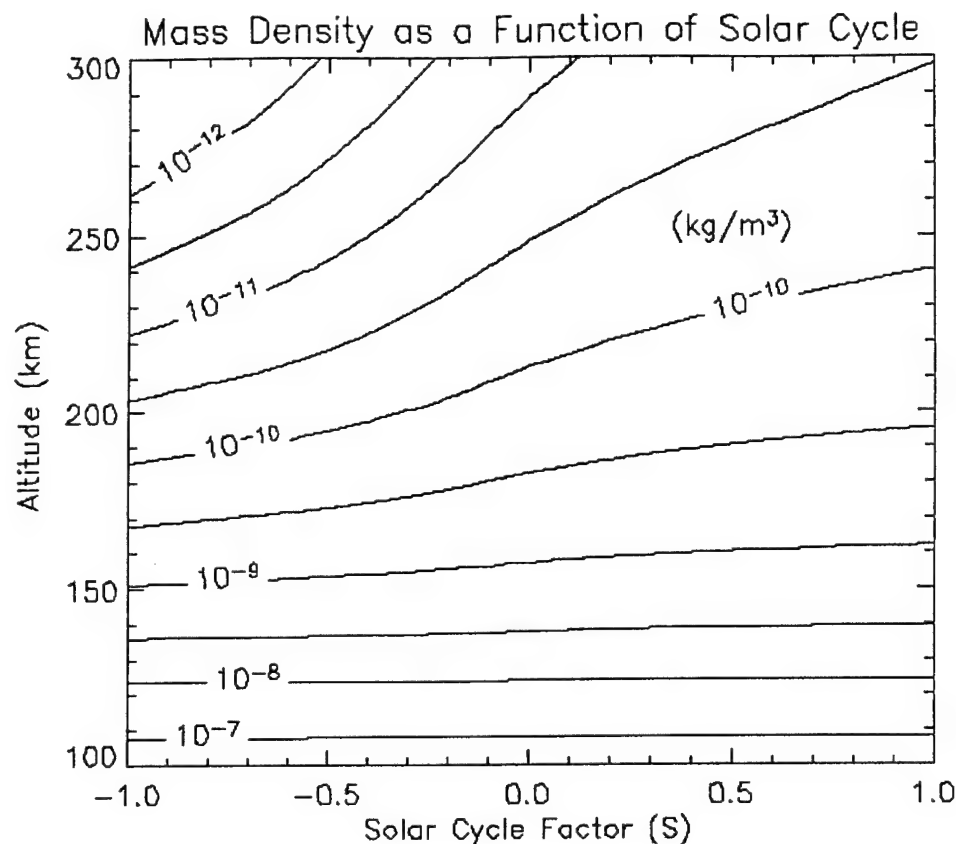
Figure 19. A contour plot of the global mean neutral mass density (kg/m³), shown as a function of altitude and solar cycle.

The neutral gas temperature, and hence mass density, varies much less at low altitudes. Near 130 km, the global mean mass density varies by only ~5% over the course of a normal solar cycle. Decreasing the solar activity index to $S = -1$ only reduces the density 9% from normal minimum conditions. Highly elliptic satellites, such as the proposed Geospace Electrodynamic Connections (GEC) mission designed to study current closures in the lower ionosphere at roughly 130 km, would therefore not experience significant gains to their lifetime.

6.5.2. Total Electron Content

In Figure 9, section 4.5, we described the variation of the global average total electron content (TEC) over the course of a normal solar cycle. The top panel of Figure 20 similarly displays the TEC, but now extending the range down to $S = -1$, and on a logarithmic scale. In
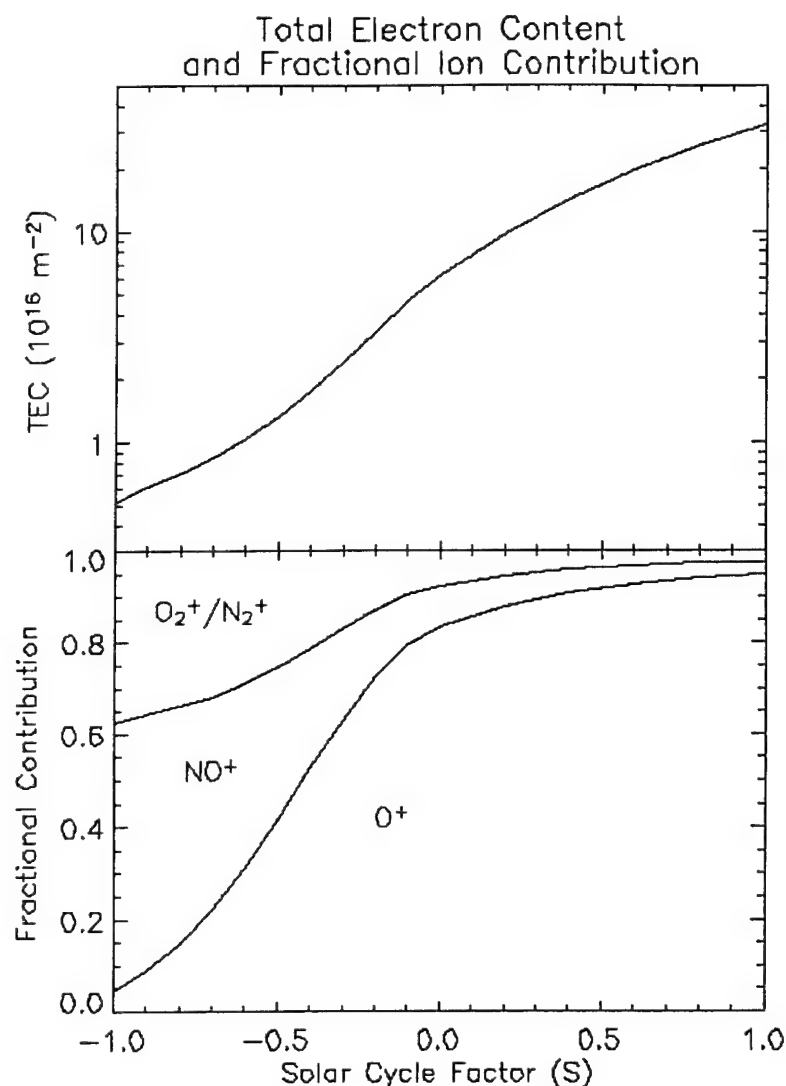
Figure 20. The top panel showing the modeled global mean total electron content (TEC) as a function of the solar cycle. Assuming an electrically neutral ionosphere, the lower panel indicates the fractional contribution made to TEC by the important ion species. This panel is cumulative, with the contributions summing to one at each value of S.

general, the figure illustrates the rapid decrease of TEC, falling below one TEC unit (10^{16} m^{-2}) by

S = −0.7.

On a linear scale the curve appears roughly quadratic or even exponential, but note on the log

scale the transition to a Maunder Minimum ionosphere is apparent. Between S = 0.0 and S =

−0.5, the curve exhibits a broad inflection, in the same region molecular ions begin to dominate

over O$^+$. Assuming an electrically neutral ionosphere, the individual ion concentrations represent

fractional contributions to the total electron content. The inflection in TEC thus reemphasizes the transition from a rapidly decreasing O^+ contribution to a more slowly decreasing molecular contribution.

The bottom panel of Figure 20 highlights the fractional contribution made by each ion species to the overall TEC. In the normal ionosphere, O^+ contributes more than 80% to the total TEC; by contrast, at $S = -0.5$ the fraction is down to 40%, and it decreases to just 5% at $S = -1$. These changes have implications to the operation of incoherent scatter radars (ISR). When an ISR is used to sound the upper atmosphere, the echoes it receives contain a convolution of both ion composition and temperature information. The echoes are typically interpreted assuming a specific altitude-dependent ion composition, which would be radically different in a Maunder Minimum epoch.

6.5.3. Pedersen and Hall Conductivities

In the ionosphere, the conductivity tensor can be expressed as a combination of three components oriented with respect to the external magnetic field line: specific conductivity orientated parallel to the magnetic field, Pedersen conductivity is perpendicular to the magnetic field but parallel to the applied electric field, and Hall conductivity is perpendicular to both fields. The specific current is controlled by the high electron mobility, and is orders of magnitude larger than the other two components, resulting in spatially uniform electric fields in the parallel direction. Pedersen and Hall conductivities determine closure of horizontal currents, and therefore the coupling between the ionosphere and magnetosphere.

To generate a Hall current the electrons must undergo an $\mathbf{E} \times \mathbf{B}$ drift (i.e., collisionless), while the ions remain relatively fixed by collisions, otherwise they will both drift in the same direction. This restricts the Hall conductivity to a narrow effective altitude range of roughly 95 and 130 km. Because of the high electron mobility, the Pedersen conductivity is determined primarily by the

ions. As long as the ions are not completely collisionless, there is a contribution to this

conductivity, which expands the effective altitude range to include the F-region.

The top panel of Figure 21 displays the height integrated Pedersen and Hall conductivities

(conductance) as a function of solar cycle; in both cases the conductivities are integrated over the

full vertical profile, 95 to 700 km. At S = 0, the two values are roughly equal. Over the course of

the normal solar cycle the Pedersen conductance begins to separate from the Hall, until it is about
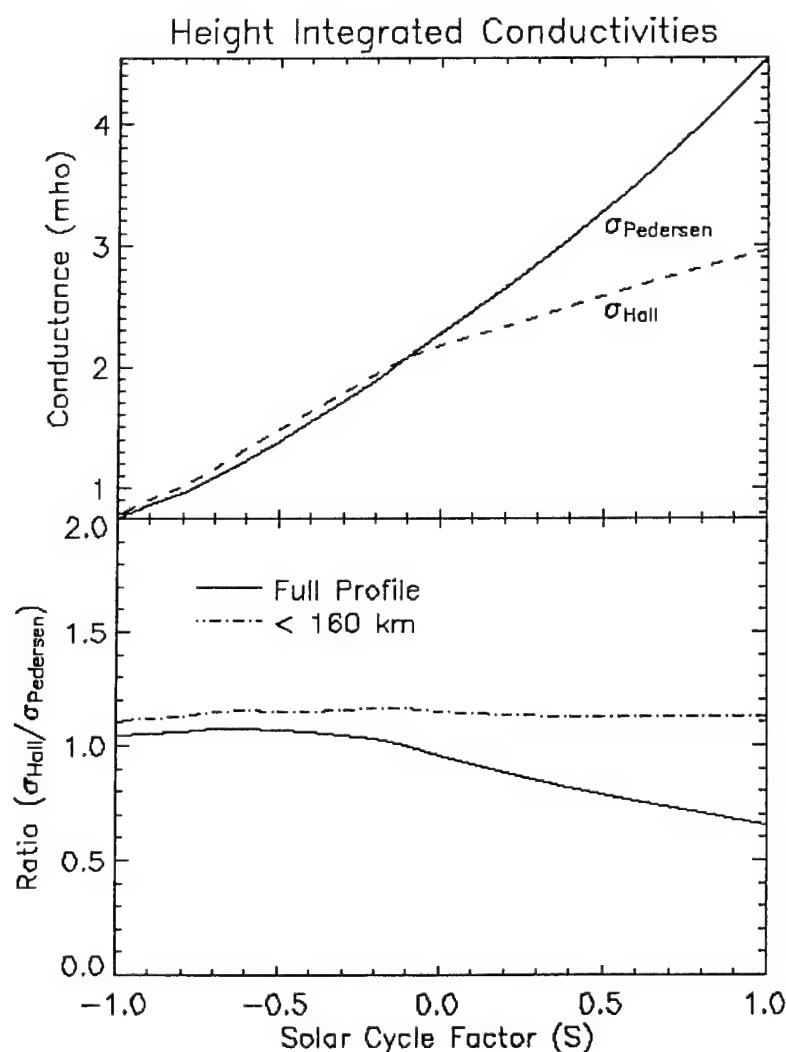
Figure 21. Height integrated conductivities as a function of the solar cycle factor. The top panel
shows the Pedersen (solid) and Hall (dashed) conductance, where the conductance was calculated
by integrating up to 700 km. The bottom panel gives the ratio of the Hall to Pedersen
conductance for two cases: integration up to 700 km (solid) and only up to 160 km (dot-dash).

50% greater at S = 1. This separation reflects an increasing F-layer contribution to the Pedersen conductivity. For solar activity less than S = 0, the F-layer contribution quickly becomes negligible, and both values track closely.

The bottom panel of Figure 21 shows the ratio of the Hall to Pedersen conductance, also as a function of solar cycle. The solid line corresponds to a full integration over the entire vertical profile, while the dot-dash line gives the ratio when the integration is only up to 160 km. This panel again highlights the importance of the F-layer contribution to the total Pedersen conductance. When the F-layer contribution is excluded, the ratio is relatively constant and equal to ~1.1 over the full range of solar activity, otherwise the ratio drops with increasing solar activity to a value of ~0.6 at S = 1.

The exceptionally small conductivities predicted for Maunder Minimum would certainly impact the ionospheric current systems. For example, the equatorial electrojet, which is responsible for the Appleton anomaly, depends on the strength of these conductivities. To completely explore this question would require a 3-D model, since the primary driver of this current is the neutral wind. However, we suggest the combination of lower electron densities, peak electron density altitude, and conductivities should result in a smaller anomaly that lies closer to the magnetic equator. In accordance with the earlier results, we would expect the anomaly to be formed primarily from NO^+ rather than O^+.

6.6. Discussion

The transition of the normal ionosphere to one dominated by molecular ions represents a dramatic morphological change. This Maunder Minimum ionosphere is not tied to any specific representation of the input solar irradiance, but rather is a result of lower thermospheric temperatures and a decrease in the neutral atomic oxygen concentration. Furthermore, as Figure 15 indicates, this transition occurs between S = −0.2 and S = −0.4, prior to the level of activity suggested as representative of Maunder Minimum [*Lean*, 2004].

Hints of this transition can be found in the observational database. In the summer months, mid-latitude, daytime ionograms typically reveal E, F_1, and F_2 layer peaks at successively higher altitudes. The E and F_2 layers are known to correspond to molecular and O^+ ions respectively. While in situ measurements of F_1 layer are rarely made, our model indicates it is primarily NO^+ (see Figure 6, page 36). During solar minimum, the observed F_1 peak densities are not only better defined, but closer in magnitude to the F_2 peaks than they are during solar maximum. This is exactly the trend we expect from our Maunder Minimum results – decreasing importance of O^+ in relation to the molecular ions. These inferences were made from an initial inspection of ionosonde measurements available from the National Geophysical Data Center. Further climatological studies are needed to confirm this observational trend and compare with modeling results.

The choice of solar EUV model has little bearing on our results. Figure 22 compares the transition from a normal to Maunder Minimum ionosphere using each of the four EUV models described previously. Given the importance of the neutral temperature to the solution, the GAIT model was tuned, in turn, to each EUV representation such that it produced the correct exospheric temperatures over the normal solar cycle range. As described in section 5.2, this is not possible with NRLEUV model, so it was instead tuned to give the correct temperature at solar minimum. In the case of the NRLEUV model, the high-resolution (1-Å) approach described in section 6.2 was used to generate the irradiance; however, the low-resolution (1-nm) results are virtually identical.

As Figure 22 shows, the VUV, S2000, and EUVAC models each generate a similar transition window between $S = -0.1$ and $S = -0.4$. The NRLEUV model also produces a Maunder Minimum ionosphere; however, due to its smaller dynamic range, the transition does not fully occur until $S = -1$. Given the close agreement between the three empirical models, we suggest

Peak Electron Density Altitude
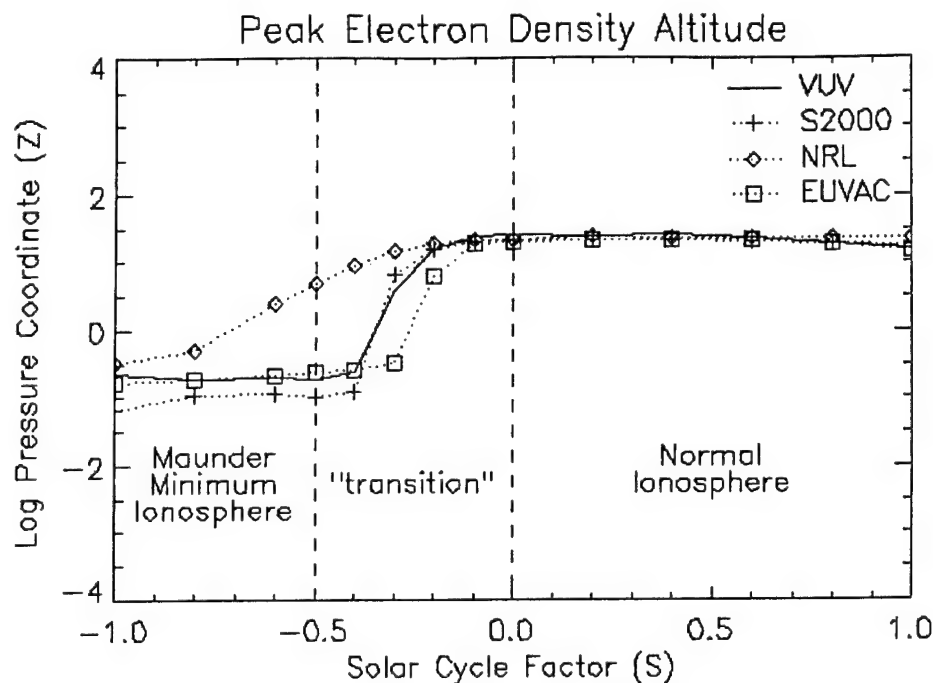
Figure 22. A comparison of the peak electron density pressure altitude, as a function of the solar cycle, calculated using four different solar irradiance models. The solid line corresponds to the standard input, the VUV model [*Woods and Rottman*, 2002], while the dotted lines with cross, diamond, and square symbols correspond to the Solar 2000 version 2.21 [*Tobiska et al.*, 2000], NRLEUV [*Warren et al.*, 2001], and EUVAC [*Richards et al.*, 1994] models, respectively.

if NRLEUV were able to reproduce the normal solar cycle variation in temperature, it too would transition to a molecular dominated ionosphere near S = −0.4.

Although the S index is convenient, the transition to a Maunder Minimum ionosphere can also be tied to a more tangible quantity – the neutral gas temperature. The pressure coordinate of the peak electron density is again shown in Figure 23, but this time as a function of the neutral gas exospheric temperature. When temperature is used as the independent variable, all four irradiance models agree remarkably well. The transition begins at roughly 650 K, just 80 K less than temperatures expected during typical solar minimum conditions. Regardless of which EUV model is used, the transition is complete when the temperature reaches 585±10 K. This is true even for the NRLEUV model; it just requires a lower S index to reach this temperature.
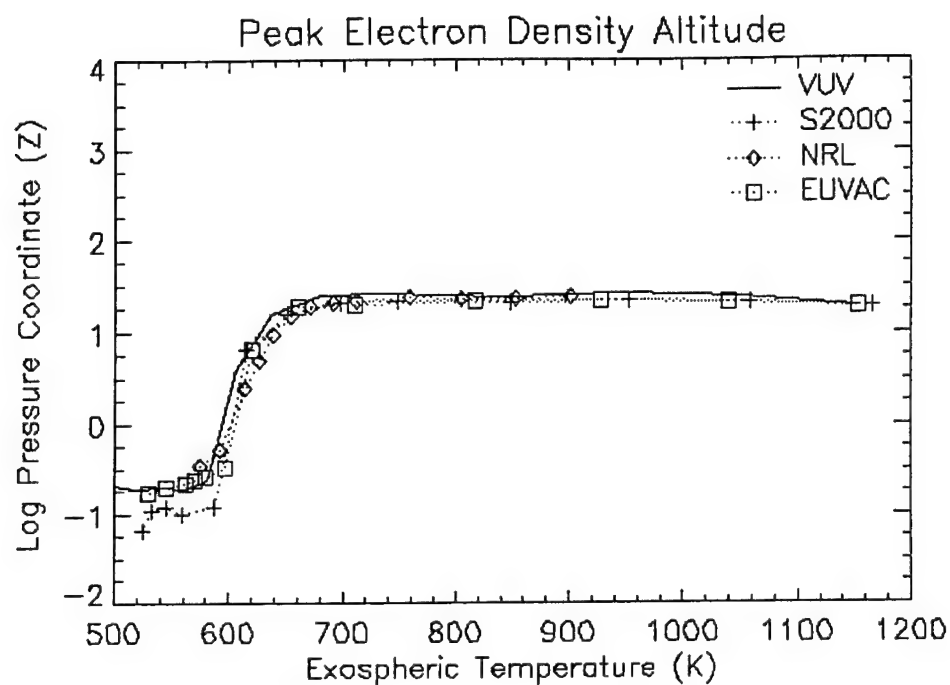
Figure 23. A comparison of the peak electron density pressure altitude, as a function of the neutral gas exospheric temperature, calculated using four different solar irradiance models. The solid line corresponds to the standard input, the VUV model [*Woods and Rottman*, 2002], while the dotted lines with cross, diamond, and square symbols correspond to the Solar 2000 version 2.21 [*Tobiska et al.*, 2000], NRLEUV [*Warren et al.*, 2001], and EUVAC [*Richards et al.*, 1994] models, respectively.

CHAPTER 7

EXTREME SOLAR MAXIMUM

7.1. Extreme Solar Maximum Irradiance

This chapter examines the response of the coupled thermosphere/ionosphere to exceptionally high levels of solar activity. In our previous efforts to simulate the Maunder Minimum period (Chapter 6), we reduced the input solar irradiance by an amount equal to the normal solar cycle variation, re. $S = -1$, because we had reason to believe the true Maunder Minimum representation fell somewhere between $S = -0.5$ and $S = -1$ [Lean, 2004]. In attempting to simulate extreme solar maximum conditions we have less guidance, and therefore more freedom.

The work of *Radick et al.* [1998] and *Radick* [2003] suggests among Sun-like stars, there exists a fairly wide range of variability, with many stars exhibiting a larger cyclic variation than the contemporary Sun. Measurements taken over the past 30 years indicate the "Sun appears to have relatively subdued … variability for its average chromospheric activity level," and could be a factor of two to three less than the stellar average [*Radick et al.*, 1998]. Given the relatively short observational database and small sample size (35 stars), it is difficult to draw strong conclusions from the Radick et al. work, but it does suggest the Sun is physically capable of much higher activity levels. One possibility, yet to be confirmed by observation, is Sun-like stars transition through a range of activity levels, from non-cycling, Maunder Minimum type periods, to extremely active periods. The contemporary Sun could, in fact, be in the midst of a relatively quiet epoch, with significantly higher activity in both its past and future.

Analysis of cosmogenic isotopes, such as ^{14}C and ^{10}Be, provides clues to past levels of solar activity. In Chapter 6, we cited the work of *Webber and Higbie* [2003] and *Eddy* [1976] to argue that solar activity during the Maunder Minimum was significantly different from normal minimum conditions. *Eddy* [1976] also used the ^{14}C record to identify a Grand Maximum period

during the 12th and 13th centuries, which coincided with an increase in the number of recorded naked-eye sunspot observations. Taken in conjunction with the Radick et al. work, there is sufficient evidence to warrant an investigation of solar activity levels significantly higher than S = 1, and their impact on the coupled thermosphere/ionosphere.

Rather than attempt to justify a particular S value as an upper limit on our Sun's cyclic variation, we chose to simply increase the solar cycle factor until the GAIT model began to break down. This practical limit was found to be approximately S = 6; above this value, the model experienced stability problems. More work is needed in order to fully understand and overcome these issues; in the meantime, we have uncovered a variety of interesting and unexpected results within the range S = 1 to 6.

When computing the Maunder Minimum irradiance, we were primarily concerned with how to appropriately reduce each of the solar emission components toward zero, and argued the best approach would be to scale the chromospheric and coronal emissions separately (section 6.2). Although it would be preferable to separate the emission components in this case as well, it is not as important, since the flux at all wavelengths is increasing. The question is moot anyway, since only the NRLEUV model provides sufficient spectral resolution to make this separation, and we have already shown it cannot reproduce the normal variation in exospheric temperatures (section 5.2). An issue of greater concern is whether we can reasonably expect all of the various emission components to scale linearly and uniformly over such a wide range (S = −1 to 6). But again, in the absence of more sophisticated irradiance models, we have no alternative but to continue using the same linear extrapolation described previously by equation (13).

Figure 24 details the spectral differences between a solar cycle factor of one and six, using the VUV irradiance model [*Woods and Rottman*, 2003]. The figure shows the solar energy flux as a function of wavelength, with both axes on a logarithmic scale. Even though some of the
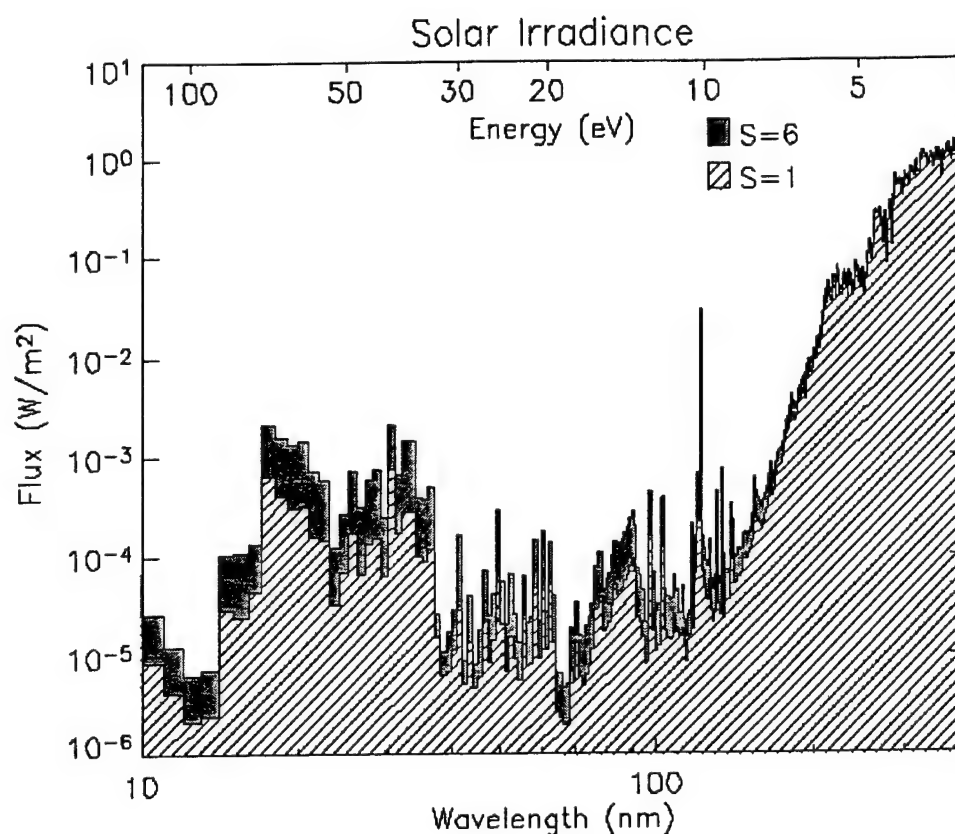
Figure 24. The standard solar maximum irradiance (S=1) compared to a hypothetical extreme maximum spectrum (S=6); both examples are calculated using the VUV model [*Woods and Rottman*, 2003]. The irradiance is shown in energy units (W/m²), and both the x and y axes are given on a logarithmic scale.

EUV wavelengths vary by more than an order of magnitude, the integrated energy input is essentially constant. For example, between S = 1 and S = 6, the EUV energy flux at the top of the atmosphere increases from 7 mW/m² to 26 mW/m², or 280%. In the UV wavelengths the increases are much smaller; since the UV dominates the integrated energy flux, the net energy increase between 3 and 360 nm is less than 2%.

Tracking the total energy input is important, since we assume the lower boundary conditions remain constant under increased solar activity. One way to gauge the impact to the lower atmosphere is by considering the net increase in solar energy flux penetrating through to the mesosphere. Table 4 lists the solar energy flux, at the top of the atmosphere, in six wavelength

Table 4. The Solar Energy Flux (W/m^2) as a Function of the Activity Index S, in Six Wavelength Bands. The Percentage of Energy Penetrating Through to the Mesosphere Is Given at the Bottom.

Solar Energy Flux (W/m^2)

S	3-105 nm	121.6 nm	125-175 nm	175-200 nm	200-360 nm	Total
0	3.02E-3	6.19E-3	1.36E-2	5.00E-2	6.60E+1	6.61E+1
1	6.90E-3	1.02E-2	1.54E-2	5.42E-2	6.62E+1	6.64E+1
3	1.47E-2	1.84E-2	1.88E-2	6.27E-2	6.68E+1	6.69E+1
6	2.63E-2	3.05E-2	2.40E-2	7.54E-2	6.74E+1	6.76E+1
	0.03%	65%	5%	70%	100%	100%

bands, and for four different values of S. The bottom row of the table gives the percentage of this incident energy that penetrates through to the mesosphere. As it turns out, the percentage for each wavelength bin is essentially independent of S.

In the EUV (3-105 nm), the energy flux increases more than eight-fold between S = 0 and 6, but it is deposited exclusively in the thermosphere; only 0.03% of this flux penetrates to the mesosphere. At longer wavelengths, a greater fraction of the energy penetrates, but the variability is smaller. Because the photon flux increases logarithmically with wavelength, the integrated 3-360 nm energy flux is dominated by the longest wavelength band (200-360 nm). Effectively all of this energy passes through the thermosphere, but between S = 0 and 6 the total flux only increases by 2%. Based on these results, we believe it is reasonable to keep the lower boundary conditions fixed with S. Certainly there would be some differences at S = 6, but extrapolating from the normal solar cycle variation at 95 km, they should be on the order of 5%.

7.2. Temperature Response

We ran the GAIT model using solar cycle factors ranging from S = 0 to 6. The model was configured using the same parameters and inputs as described previously in Chapters 3 and 4, and included the modification to the electron temperature boundary condition given in section 6.3. The altitude of the upper boundary was chosen such that the pressure coordinate there stayed

fixed at $Z = 6.2$; in the case of $S = 6$, this required a peak altitude of 4270 km, compared to only 700 km at $S = 1$.

Profiles of the global mean neutral (T_n), ion (T_i), and electron (T_e) gas temperatures are provided in Figure 25. The profiles are given as a function of the log pressure coordinate, with the corresponding altitudes on the right-hand side of the figure. Three panels correspond to increasing levels of solar activity. The top panel highlights normal solar maximum conditions ($S = 1$), and is the same as the result presented earlier in Figure 4. The middle and lower panels correspond to $S = 3$ and $S = 6$, respectively. A complementary view is provided in Figure 26. In this figure the temperatures are plotted as a function of altitude, to highlight the gradients near the model's lower boundary.

From Figure 25, we can see the modeled exospheric temperatures increase rapidly with S. At $S = 1$, the neutral exospheric temperature is calculated to be 1255 K; this increases to 2570 K at $S = 3$, and jumps past 5700 K by $S = 6$. As S increases, so does the total electron density; this increases the collisional coupling between the three gases, to the point the temperatures shown in the bottom panel are nearly equal over the entire profile.

As is apparent from Figure 26, below 120 km there is relatively little change in the temperature profile with S. At the lower boundary, the neutral gas scale height is approximately 6 km. Within two scale heights of the boundary, T_n increases by only 32 K (18%) at $S = 3$ and 50 K (28%) at $S = 6$. However, the issue of temperature gradients raises the question of how much energy is being lost, via conduction, through the lower boundary, and if this heat source will upset our assumption of fixed boundary conditions. At $S = 1$, eddy and molecular conduction combine to push roughly 0.65 mW/m^2 into the mesosphere; this increases to 1.01 mW/m^2 at $S = 6$. These levels are small compared to the solar flux that penetrates from the thermosphere. Mesospheric heating by downward conduction amounts to only 2% of the energy available in Hydrogen Lyman-α (121.6 nm) and the Schumann-Runge bands (175-200 nm), which are
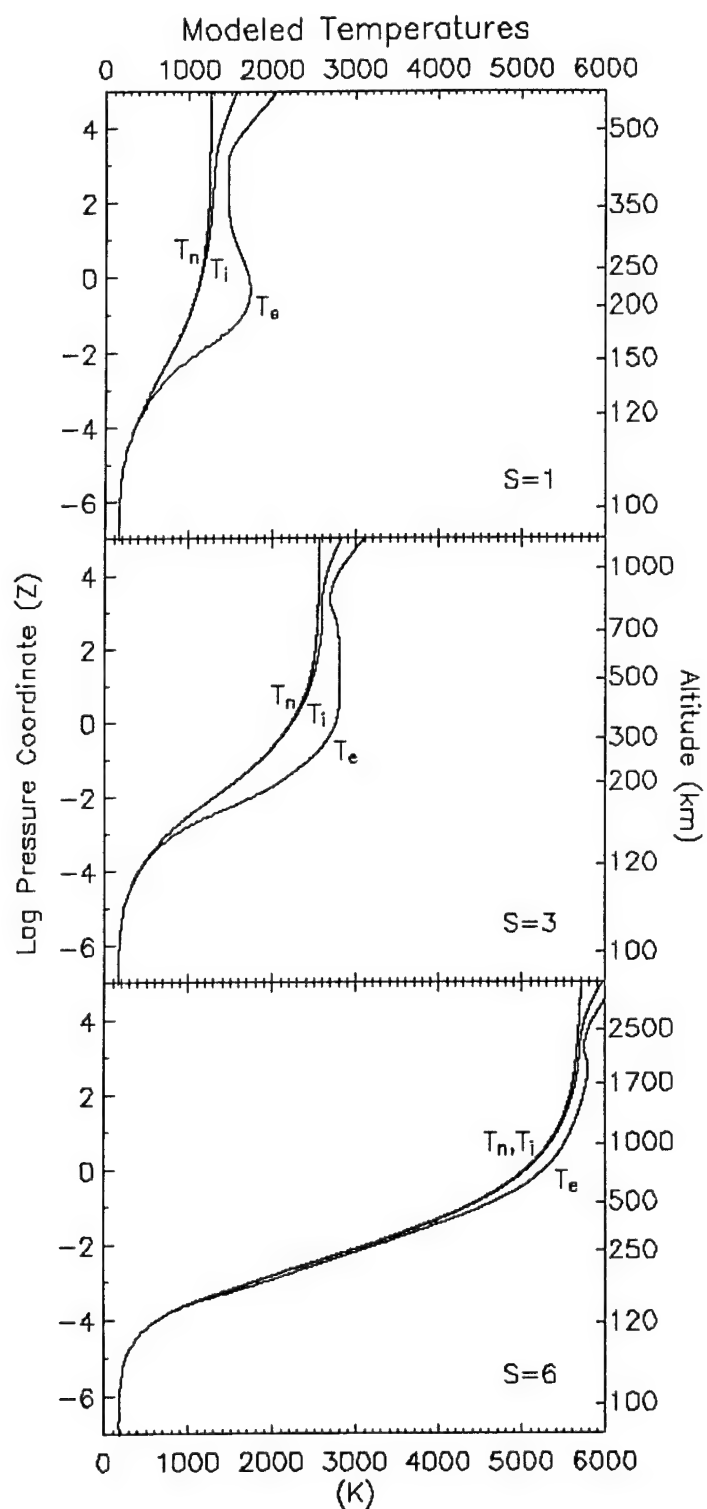
Figure 25. Global mean temperature profiles calculated using the GAIT model for three increasing levels of solar activity: S=1, S=3, and S=6. The profiles are plotted as a function of the log pressure coordinate, Z, with the corresponding altitudes provided on the right-hand side of the figure.
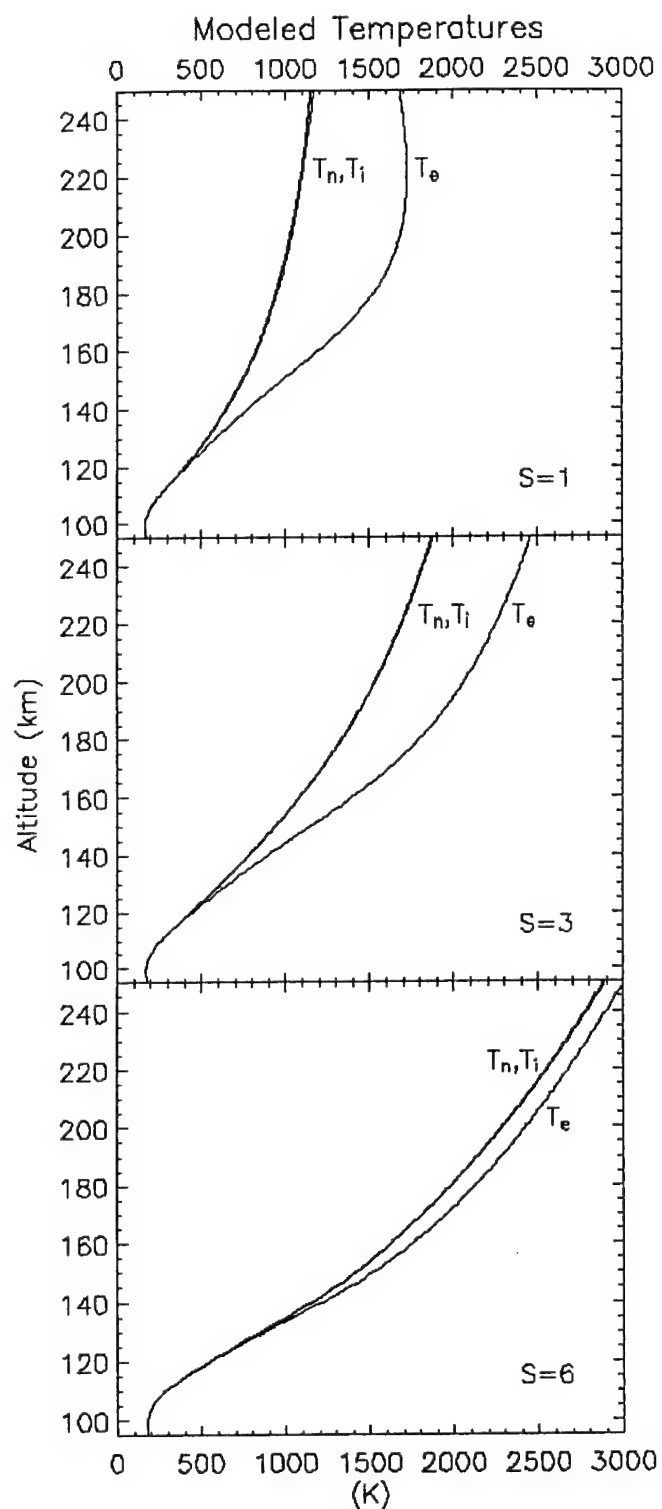
Figure 26. Global mean temperature profiles calculated using the GAIT model for three increasing levels of solar activity: S=1, S=3, and S=6. The profiles are plotted as a function of the absolute altitude (km).

the wavelength regions most readily absorbed in the upper mesosphere. For this reason, we again conclude the lower atmosphere is relatively unchanged, even when subject to extremely high S values.

From the profiles given in Figure 25, we recognized the temperatures were increasing rapidly with S. In Figure 27 we show the neutral gas exospheric temperature as a function of the solar cycle factor. The plot is fairly straight on a logarithmic scale, especially between S = 1 and 5, indicating a near exponential increase in the temperature. In section 4.5 we noted the thermosphere responded linearly over the normal solar cycle, but this behavior obviously breaks down under extreme solar maximum conditions. The total energy input to the system remains linear with S, thus the likely cause of this response is a decrease in the effective cooling rate.

Figure 28 reveals the fractional contributions of the various cooling mechanisms as a function of the solar cycle factor. Infrared radiation emitted by O, NO, and CO_2 comprise the majority
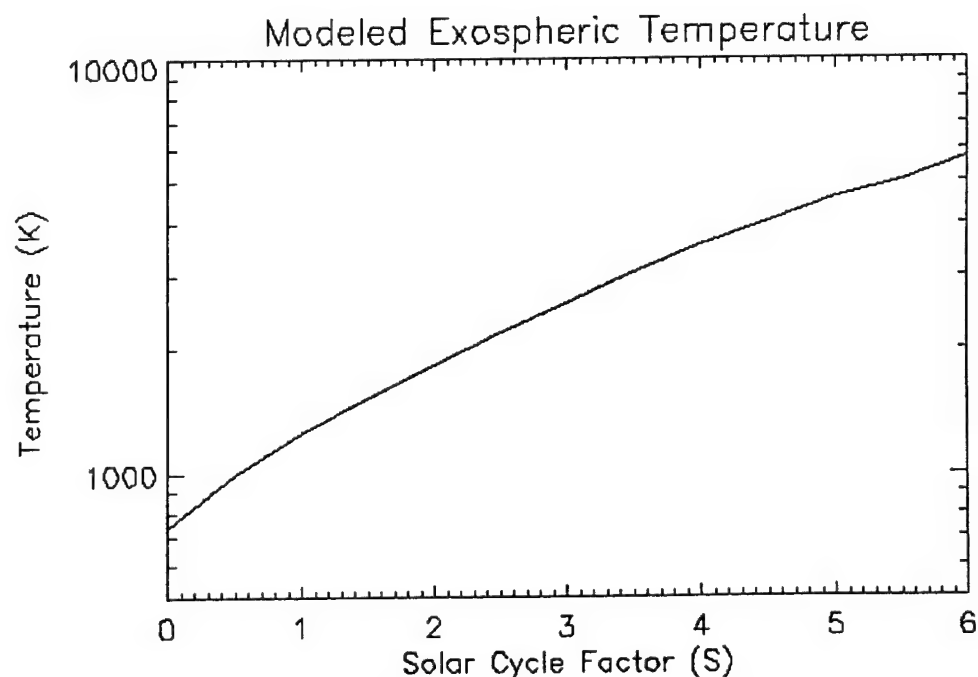
Figure 27. The variation of the global mean exospheric temperature shown as a function of the solar cycle factor S, ranging from normal solar minimum (S=0) to an extreme maximum (S=6). The temperature is given on a logarithmic scale.
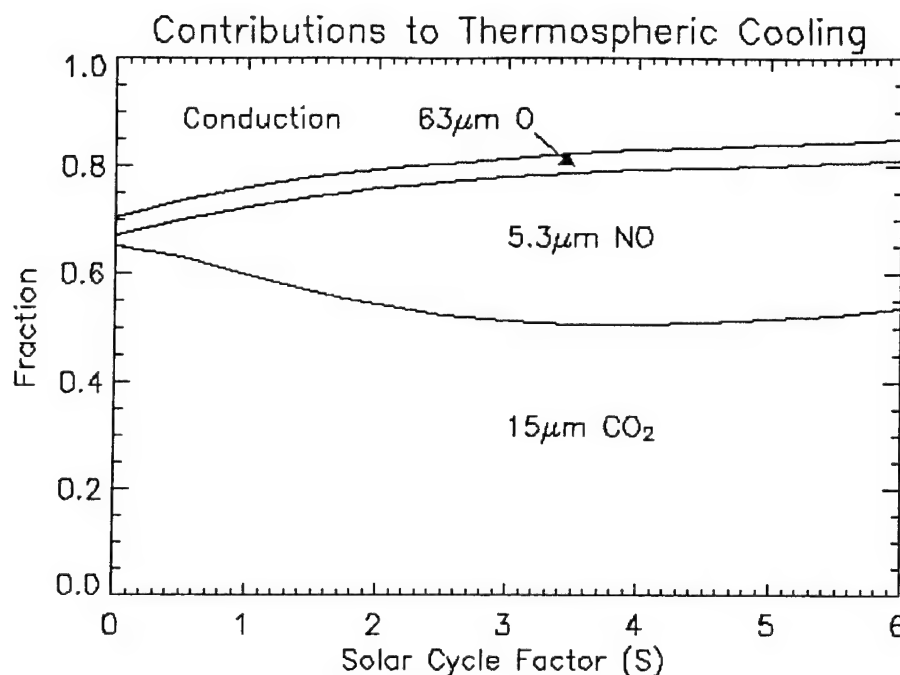
Figure 28. A cumulative plot showing the fractional contribution of important processes to the total cooling rate as a function of the solar cycle factor S, which ranges from normal solar minimum (S=0) to an extreme maximum (S=6). Infrared radiation emitted by O, NO, and CO_2 comprise the majority of the cooling rate; a combination of eddy and molecular conduction make up the balance.

(70-85%) of the total thermospheric cooling rate, with the balance made up by a combination of eddy and molecular conduction. The contribution from conduction, primarily eddy conduction, decreases from roughly 30 to 15% with increasing solar activity. Among the radiative cooling mechanisms, 63 μm radiation from the fine structure of O constitutes a small (~5%), yet constant contribution. As described in Chapter 4, the relative importance of 5.3 μm radiation from NO increases over the course of the normal solar cycle; at S = 0, it contributes only 2% to the net cooling rate, increasing to 13% by S = 1. This trend continues to S = 4 where the contribution peaks at 29%, and then remains relatively steady through S = 6. The 15 μm radiation from CO_2 comprises the remainder of the total cooling rate. Its importance decreases slightly as NO cooling grows more effective, but never drops below 50% of the total. It is important to note the rate coefficient for excitation of the fundamental band in NO does not include any temperature

dependence (see section 3.6). *Dodd et al.* [1999] suggested the coefficient could be

inversely related to temperature, which would decrease the cooling rate at high S levels, but there

is currently no experimental evidence to support this speculation.

We can explain the nonlinear temperature increase observed in Figure 27 by examining the

behavior of the two species most important to cooling, CO_2 and NO. Figure 29 compares the

number density profiles of CO_2 (top panel) and NO (bottom panel), calculated at three different
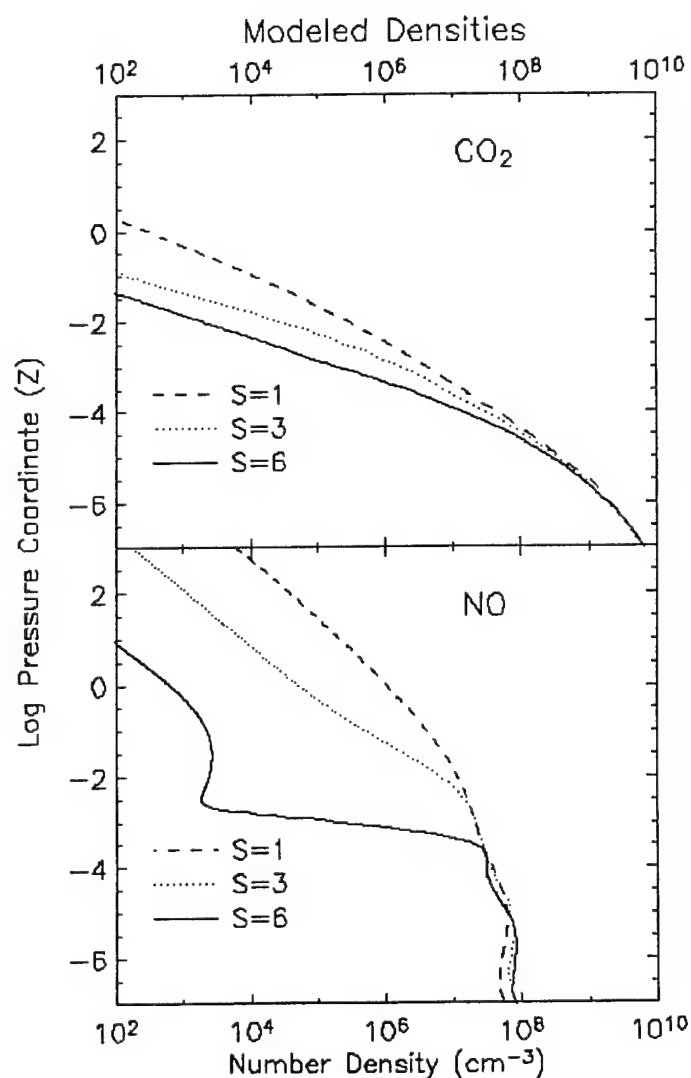
Figure 29. A comparison of the CO_2 (top panel) and NO (bottom panel) global mean number densities, calculated at three increasing levels of solar activity. The dashed lines correspond to a solar cycle factor of S=1, the dotted lines to S=3, and the solid lines to S=6.

solar activity levels. Note at $Z = -2$ the CO_2 concentration falls by a little more than two orders of magnitude from $S = 1$ to $S = 6$. On a constant pressure surface, we would expect some decrease due to the fact the total concentration must decrease as the temperature increases; however, the neutral gas temperature at $Z = -2$ only increases by a factor of four. The bulk of the decrease in CO_2 comes, instead, from photolysis. At the top of the atmosphere, the total CO_2 photolysis rate increases by more than a factor of two between $S = 1$ and $S = 6$. With no thermospheric production terms to compensate, the CO_2 concentration decreases rapidly.

In a similar vein, Figure 29 reveals the NO concentration undergoes a dramatic decrease near $Z = -3$. The NO photolysis rate only increases by 40% between $S = 1$ and $S = 6$, not enough to explain the observed drop in concentration. Instead, the dominant loss mechanism for NO is its reaction with atomic nitrogen, k_{14} in Table 1. Figure 30 compares the calculated $N(^4S)$ concentration for three levels of solar activity, and we find the peak value increases almost two orders of magnitude between $S = 1$ and 6. This is due to enhanced photolysis of N_2, which

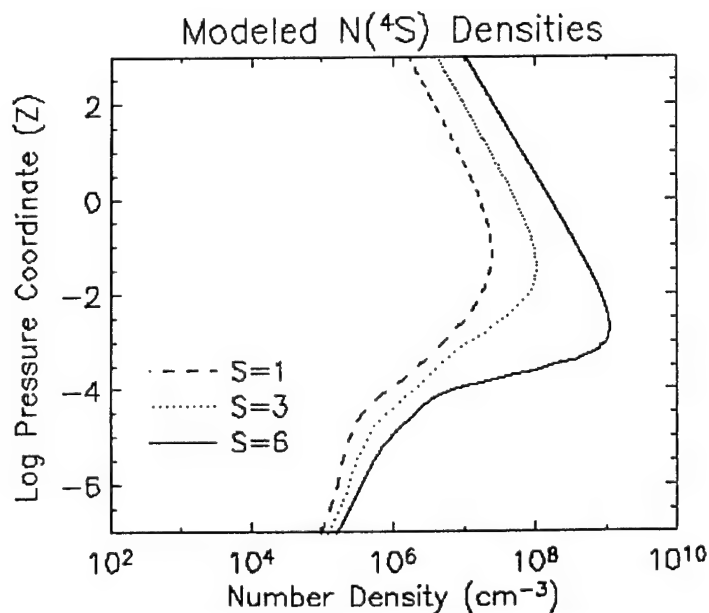**Figure 30**. A comparison of the $N(^4S)$ global mean number density, calculated at three increasing levels of solar activity. The dashed line corresponds to a solar cycle factor of S=1, the dotted line to S=3, and the solid line to S=6.

occurs primarily via the highly-variable EUV wavelengths. In addition, many of the ion-neutral chemical reactions found in Table 2 result in the production of $N(^4S)$, further increasing the concentration. Over the range $S = 1$ to 6, the temperature-dependent rate constant for the $NO + N(^4S)$ reaction decreases by roughly 10% at $Z = -2$, but this is more than made up by the increase in $N(^4S)$.

Taken together, the decreases to CO_2 and NO confine the bulk of the radiative cooling to the lowest levels of the thermosphere. The net cooling rate typically increases with both the concentration of the radiating gas and the temperature; since the concentrations of CO_2 and NO are either stable or decreasing with S (Figure 29), the temperatures must increase rapidly to achieve an energy balance. A steep gradient in temperature is indeed observed at approximately 120-140 km, just above the $Z = -4$ pressure level, where the CO_2 and NO concentrations begin to plummet. The behavior of the exospheric temperature is therefore explained by nonlinear decreases to CO_2 and NO.

7.3. Major Neutral Species

Figure 31 shows the global mean number densities calculated for the three major neutral species, N_2, O_2, and O, as a function of the log pressure coordinate. Three panels in the figure correspond to increasing levels of solar activity. The top panel highlights normal solar maximum conditions (S = 1), and is the same as the result presented earlier in Figure 5. The middle and lower panels correspond to S = 3 and S = 6, respectively. A complementary view is provided in Figure 32. In this figure each of the three species is plotted separately in its own panel, and the solar activity levels are represented by dashed (S = 1), dotted (S = 3), and solid (S = 6) lines. In order to keep a uniform x-axis, the O_2 concentration is multiplied by 1000. The vertical coordinate is also changed to altitude (km).
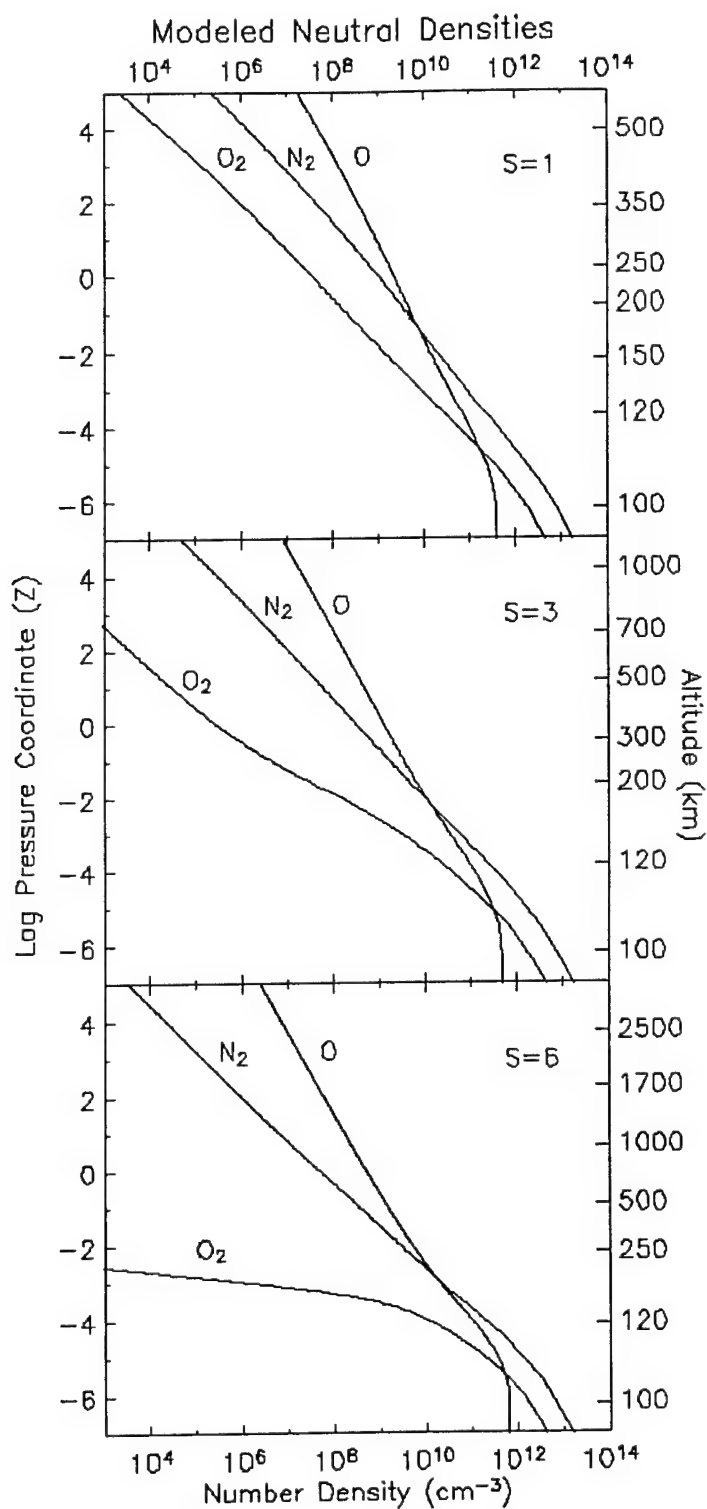
Figure 31. Global mean number density profiles of the three major neutral species (N_2, O_2, and O) calculated using the GAIT model for three increasing levels of solar activity: S=1, S=3, and S=6. The profiles are plotted as a function of the log pressure coordinate, Z, with the corresponding altitudes provided on the right-hand side of the figure.
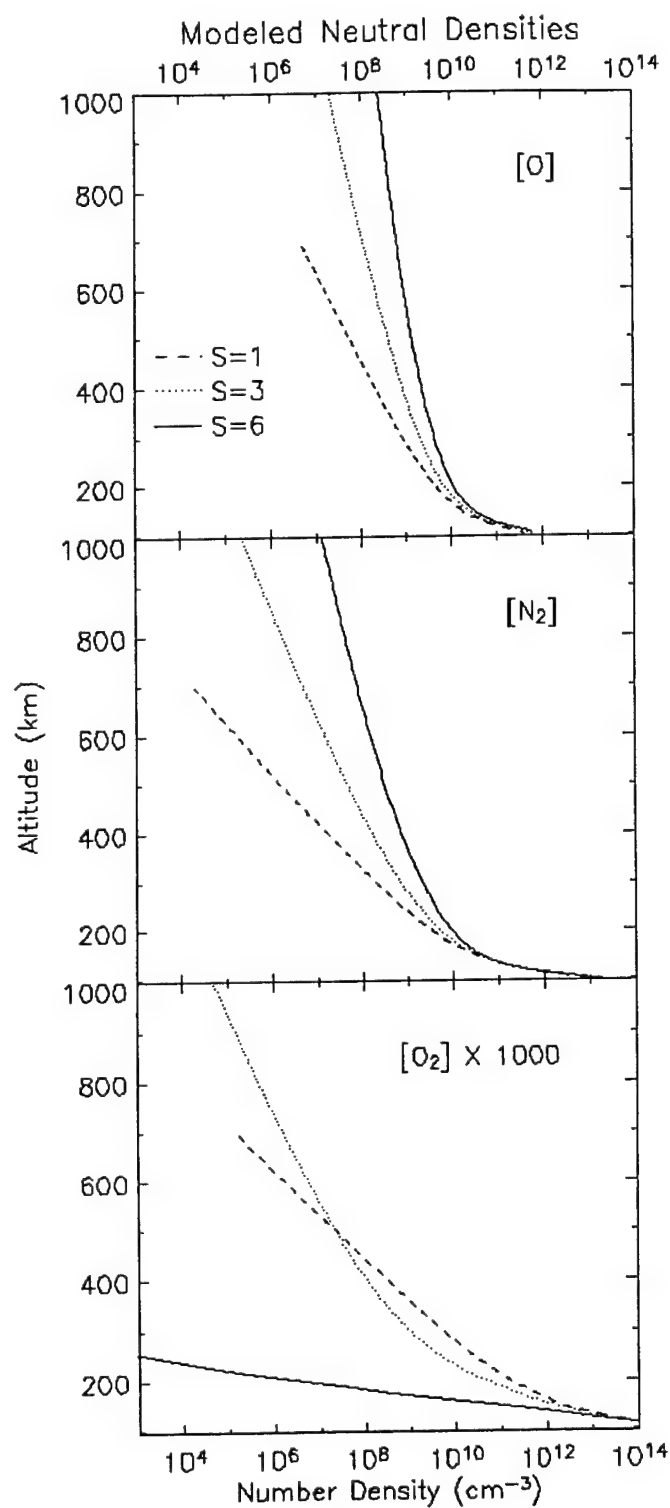
Figure 32. A comparison of global mean neutral number densities calculated at three increasing levels of solar activity: O (top), N_2 (middle), and O_2 (bottom). Dashed lines correspond to a solar cycle factor of S=1, dotted to S=3, and solid to S=6. The profiles are plotted as a function of the absolute altitude (km). The O_2 density is multiplied by 1000.

The most dramatic effect observed in the two figures is the depletion of O_2 with increasing S. Recall O_2 is dissociated directly by both EUV and UV photons. In addition, through ion-neutral chemical reactions, nearly every ion produced also results in the dissociation of an O_2 molecule [*Stolarski*, 1976]. At S = 1 (Figure 31), dissociation causes only a small inflection in the O_2 profile. However, by S = 6, the profile is radically altered; in fact, the O_2 concentration drops to nearly 10^{-2} cm^{-3} before it recovers a diffusive equilibrium shape near Z = −2. The bottom panel of Figure 32 indicates the O_2 density at a given altitude in fact decreases with S, counter to the response or N_2 and O, which increase.

Over the range of S = 1 to S = 6, the O_2 photolysis rate at the top of the atmosphere increases 80% in the UV, from 2.1×10^{-6} s^{-1} to 3.8×10^{-6} s^{-1}, and roughly 200% in the EUV and Lyman-α, from 1.9×10^{-7} s^{-1} to 5.8×10^{-7} s^{-1}. Although the percentage increase is larger, the relative contribution of the EUV and Lyman-α to photolysis is less than 15% of the UV. The more important EUV contribution comes in the form of a dramatic increase to the ionization rates, since each ion produced leads to dissociation of O_2. The total ionization rate at the top of the atmosphere increases 280% over the same S = 1 to 6 range, from 2.6×10^{-6} s^{-1} to 1.0×10^{-5} s^{-1}.

At the model's lower boundary, the atomic oxygen concentration reflects the additional O_2 dissociation, increasing roughly 60% from S = 1 to S = 6. In pressure coordinates (Figure 31), the overall shape of the O and N_2 profiles is relatively unchanged. Note, however, at a given pressure level the concentration of these two species decreases with increasing S. This is, of course, due to the fact at constant pressure the total concentration is inversely proportional to temperature. Since the neutral gas temperature increases with S, the concentrations of O and N_2 must decrease. In altitude coordinates (Figure 32), the O and N_2 profiles instead reflect the dramatic increases in scale height that occur with the rising neutral gas temperature.

7.4. Ionospheric Response

The response of the ionosphere to extreme solar maximum conditions is illustrated by three complementary figures. Figure 33 shows the global mean number densities calculated for four ion species, O^+, NO^+, O_2^+, and N^+, as well as the total electron density. The profiles are plotted as a function of the log pressure coordinate. Three panels in the figure correspond to increasing levels of solar activity. The top panel highlights normal solar maximum conditions ($S = 1$), and is the same as the result presented earlier in Figure 6; the middle and lower panels correspond to $S = 3$ and $S = 6$, respectively.

In order to highlight the effects of the expanding neutral atmosphere, Figure 34 and Figure 35 recreate the ion density profiles, but as a function of altitude. In addition, each ion is shown separately. The three panels in Figure 34 detail O^+, NO^+, and O_2^+, while N^+ is shown in Figure 35. The solar activity levels are represented by dashed ($S = 1$), dotted ($S = 3$), and solid ($S = 6$) lines, respectively.

Unlike the Maunder Minimum case, molecular ions do not become dominant. Overall, NO^+ exhibits relatively little change between $S = 1$ and $S = 6$. As expected, the peak density increases, but the profile shape remains essentially static in pressure coordinates. In contrast, O_2^+ undergoes a significant change. Although the peak O_2^+ density increases, the profile, which is bimodal at $S = 1$ and $S = 3$, loses its upper peak by $S = 6$. This is due to the dramatic decrease in neutral O_2, described previously in section 7.3. With no O_2 available to ionize, the second peak vanishes.

Perhaps the most unexpected results are the responses of the two atomic ions, O^+ and N^+. As is evident from Figure 33, the N^+ density increases dramatically over the range $S = 1$ to 6, while O^+ is relatively static, especially when viewed in pressure coordinates. When the two ions are plotted separately (Figure 34 and Figure 35), we see the O^+ peak density increases by less than 70% between $S = 1$ and 6, while N^+ jumps by nearly two orders of magnitude. A simple plot of the O^+ to N^+ ratio further quantifies these changes (Figure 36).
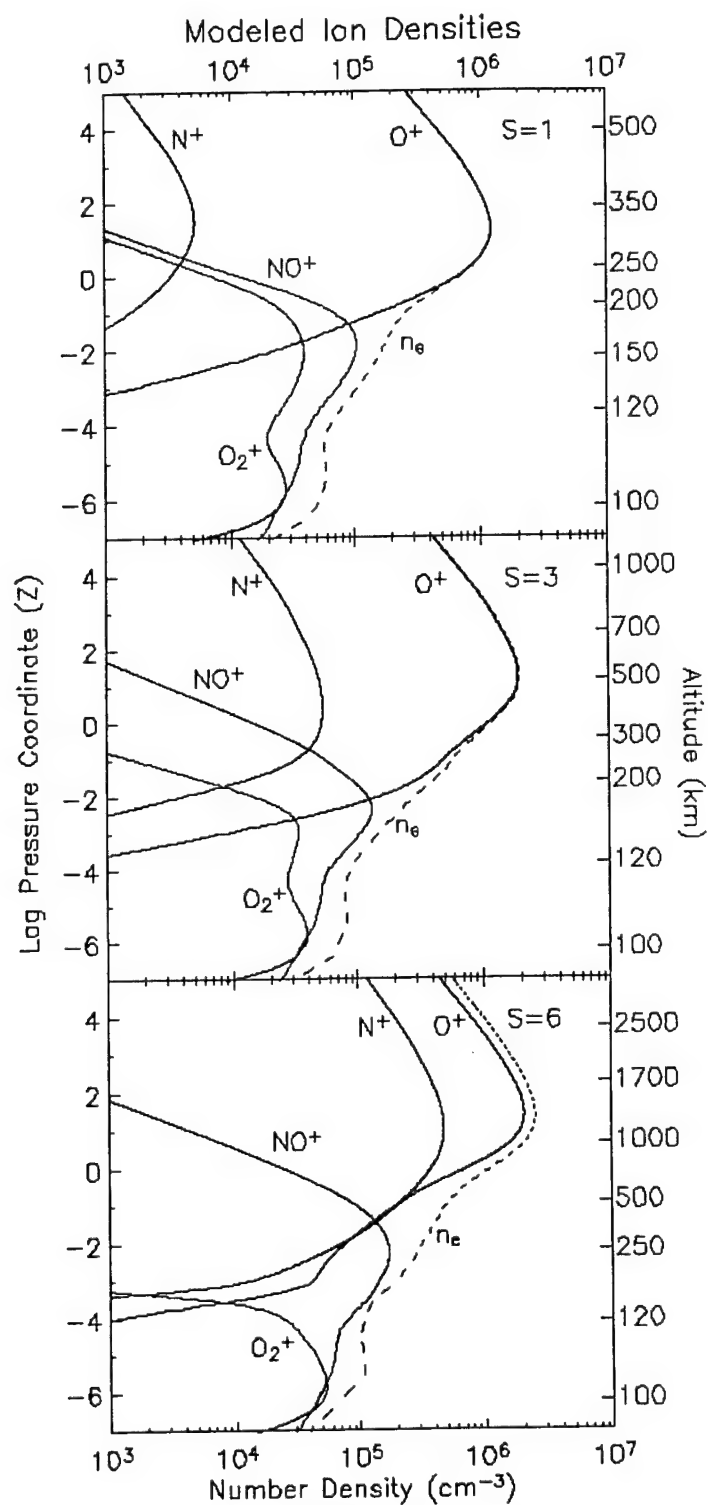
Figure 33. Global mean number density profiles of four ion species (O^+, NO^+, O_2^+, and N^+) and the total electron density (n_e), calculated for three increasing levels of solar activity: S=1, S=3, and S=6. The profiles are plotted as a function of the log pressure coordinate, Z, with the corresponding altitudes provided on the right-hand side of the figure.
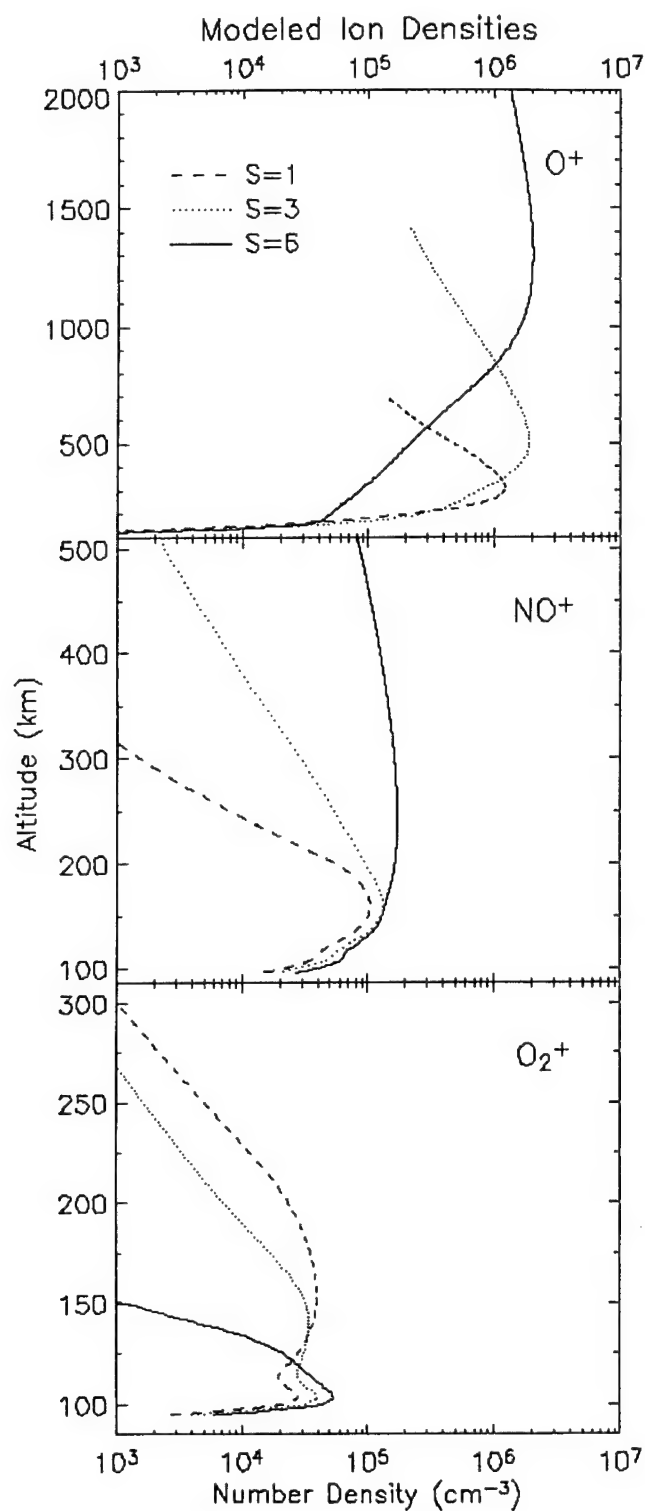
Figure 34. A comparison of global mean ion number densities, calculated at three increasing levels of solar activity. The three major ion species are shown: O^+ (top), NO^+ (middle), and O_2^+ (bottom). Dashed lines correspond to a solar cycle factor of S=1, dotted to S=3, and solid to S=6. The profiles are plotted as a function of the absolute altitude (km).
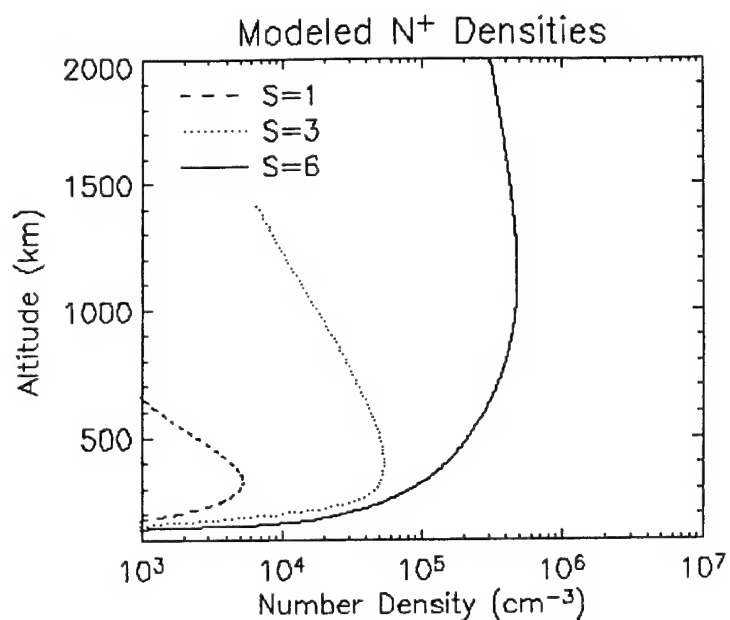
Figure 35. A comparison of the N^+ global mean number density, calculated at three increasing levels of solar activity. The dashed line corresponds to a solar cycle factor of S=1, the dotted line to S=3, and the solid line to S=6. The profiles are plotted as a function of the absolute altitude (km).
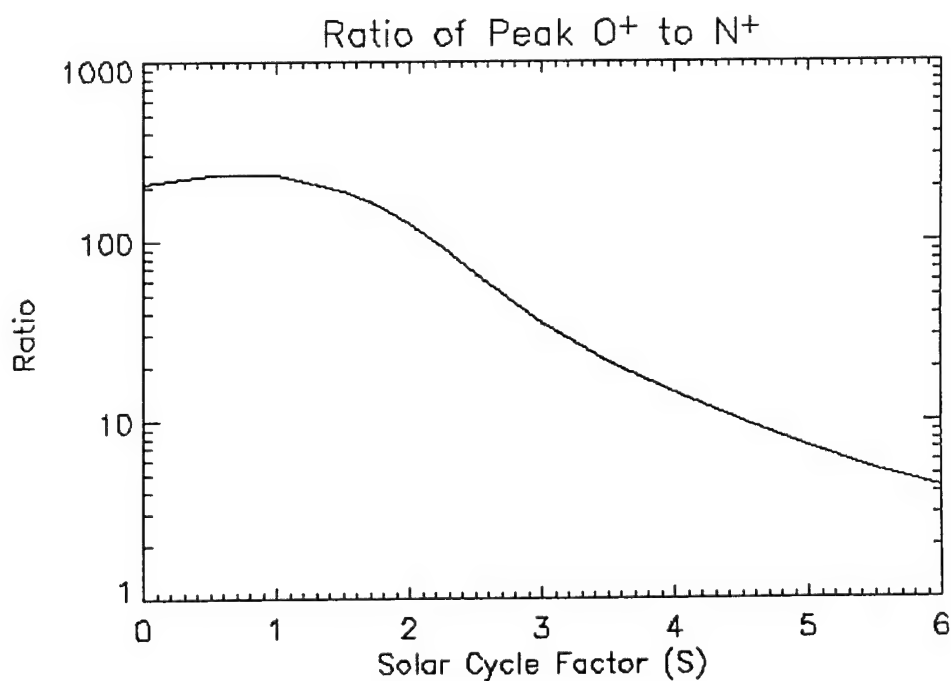
Figure 36. The ratio of the peak O^+ to N^+ concentration as a function of the solar cycle factor, which ranges from normal solar minimum (S=0) to an extreme maximum (S=6). The ratio is given on a logarithmic scale.

Figure 36 gives the ratio of O^+ to N^+ densities at the F-region peak, as a function of the solar cycle factor. Over the normal solar cycle range, the N^+ peak is more than two orders of magnitude less than O^+. By S = 6, O^+ is only about four times greater than N^+, and falling. Such a dramatic change is also apparent in bottom panel of Figure 33, where the F-region electron density is noticeably greater than the O^+ density. Assuming an electrically neutral ionosphere, we find that N^+ contributes roughly 20% to the peak electron density at S = 6, compared to less than 1% at S = 1.

The dramatic increase in N^+, and stagnation of O^+, combine to produce an interesting F-region response over the range of S. Figure 37 presents a contour plot of the global mean
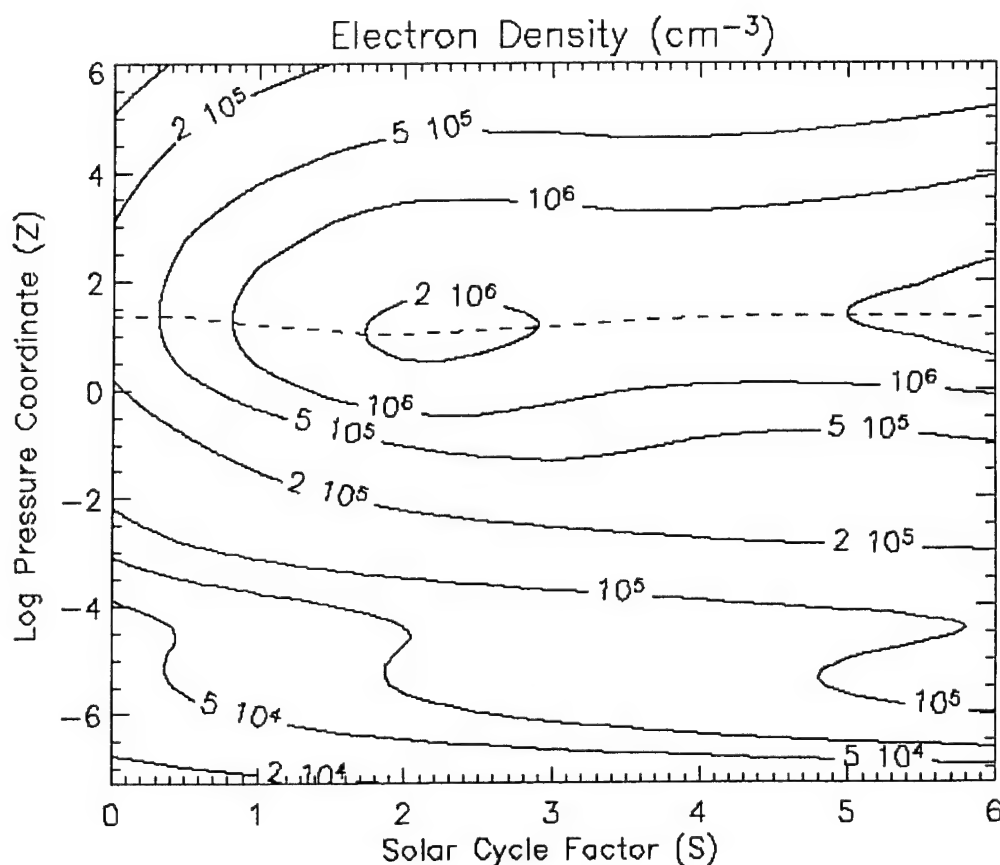
Figure 37. A contour plot of the global mean electron density (cm^{-3}), shown as a function of the solar cycle factor, which ranges from normal solar minimum (S=0) to an extreme maximum (S=6). The dashed line indicates the pressure of the peak electron density.

electron density as a function of both pressure and solar activity. The solar cycle factor

ranges from normal solar activity up to the extreme case of $S = 6$. A dashed line identifies the

pressure of the electron density peak. As described for the normal solar cycle, the peak remains

relatively fixed near $Z = 1$. Unlike the Maunder Minimum case, there is no obvious

morphological change from an O^+ dominated F-region. However, the stagnation of O^+ causes a

plateau in the peak electron density. In the figure, the electron density reaches a local maximum

near $S = 2$. After falling, the electron density begins to rise again at higher S levels, concomitant

with the elevated N^+ densities.

The underlying cause of this unique electron density structure is further revealed by an

examination of each ion over the full range of S. Figure 38 plots the peak concentration of the

four major ions, O^+, NO^+, O_2^+, and N^+, as a function of S, as well as the peak electron density. A

number of the characteristics described previously are made clear by this figure. The molecular
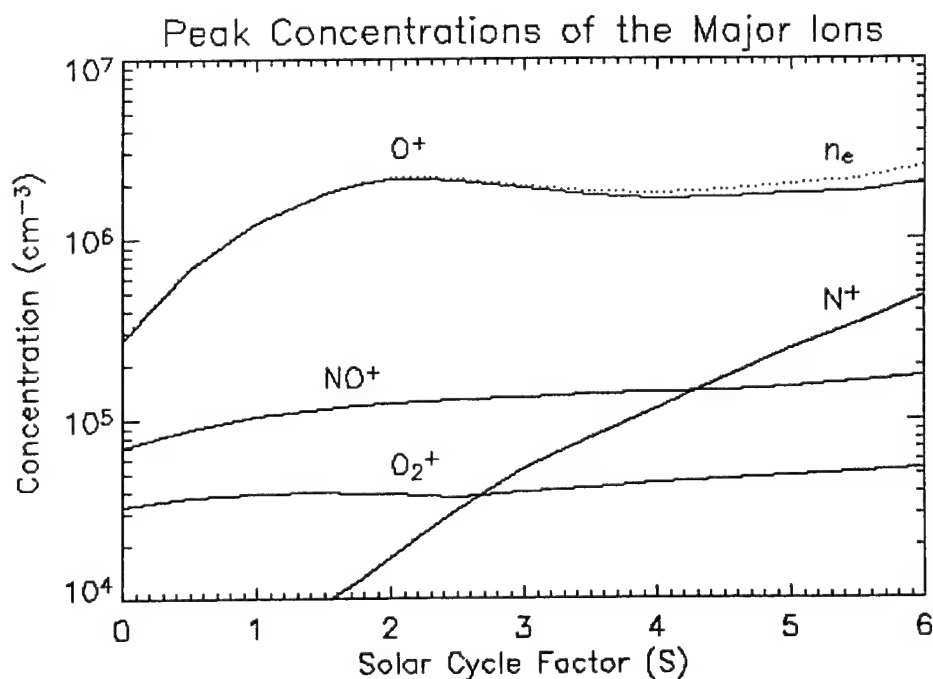
Figure 38. Peak concentrations of four ions (O^+, NO^+, O_2^+, N^+) as a function of the solar cycle factor, which ranges from normal solar minimum (S=0) to an extreme maximum (S=6). A dotted line indicates the value of the peak electron density.

ions, NO^+ and O_2^+, increase slowly, but steadily, over the range of S. A small dip in the peak O_2^+ concentration near S = 2.5 indicates a transition in its bimodal profile. For S less than 2.5, the O_2^+ peak is found in the upper maximum (see Figure 33 and Figure 34). As S increases, and neutral O_2 becomes scarce at high altitudes, the maximum concentration drops to the lower peak. Approaching S = 6, the O_2^+ concentration at this lower peak continues to increase, while the secondary peak disappears (see Figure 34).

The behavior of the atomic ions is again the most interesting feature. From Figure 38, it is evident O^+ not only plateaus, but reaches a local maximum near S = 2, and then decreases. By S = 5, the peak O^+ concentration is again increasing, but we see it is no longer solely controlling the electron density. The unexpected saddle structure observed in Figure 37 is therefore explained by a combination of O^+ and N^+ effects. Due to their interesting responses, a closer examination of both atomic ions is warranted.

7.4.1. O^+ Response

Over a range of S = 0 to 6, the O^+ concentration undergoes an interesting morphology. Within the bounds of the normal solar cycle, the peak O^+ concentration increases roughly linearly with S. But as we saw in Figure 38, this increase only holds up to S = 2. Beyond S = 2, the peak concentration decreases, reaching a local minimum near S = 4, before it slowly begins to increase again. In Figure 39 we examine the factors responsible for this morphology.

Figure 39 consists of three panels, all plotted as a function of the solar cycle factor, S. The top panel gives the peak O^+ concentration, on a linear scale. The middle panel shows the production rate ($cm^{-3} s^{-1}$) at the peak; it is dominated by ionization, both photo and secondary, of O. The bottom panel gives the loss rate (s^{-1}) at the O^+ peak. The total loss rate is determined by the contribution of two reactions, $N_2 + O^+$ and $O_2 + O^+$, which correspond to γ_1 and γ_2 in Table 2.

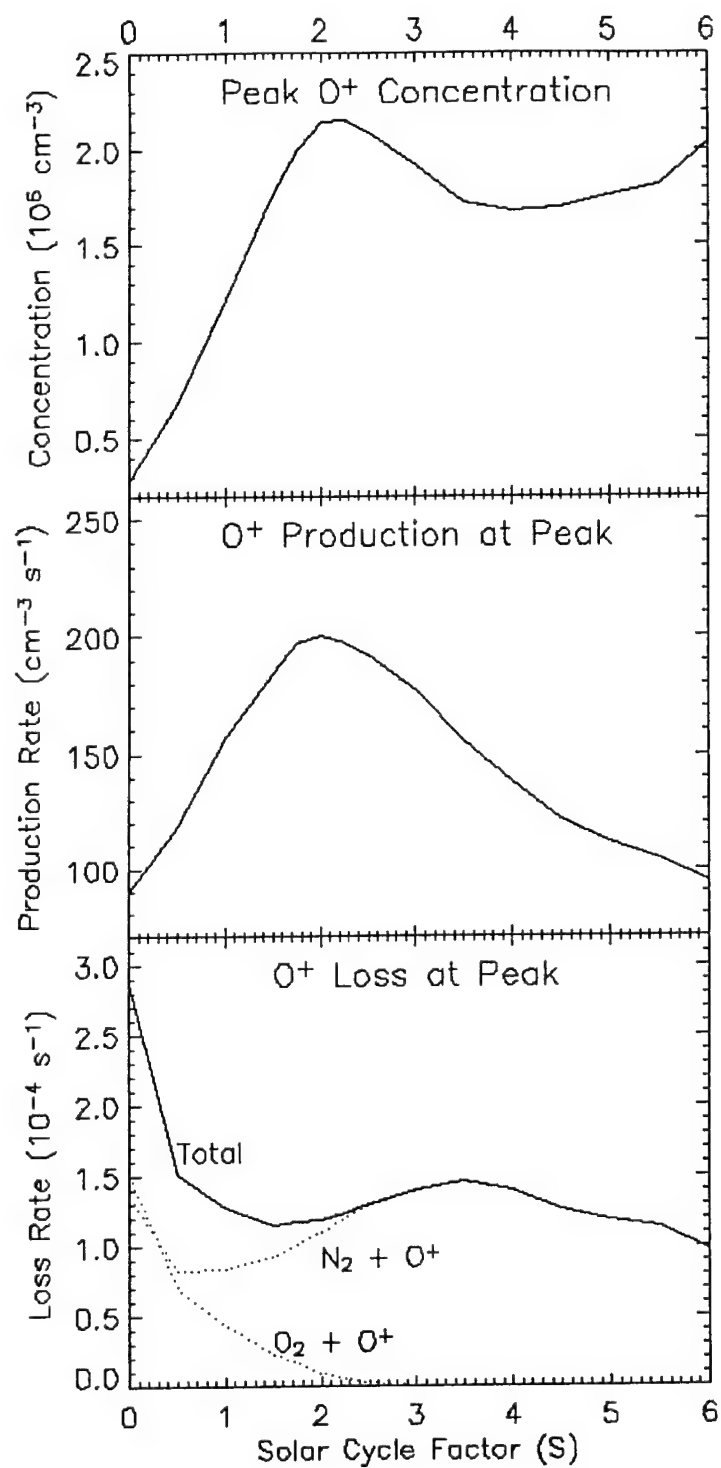**Figure 39.** Three panels showing the concentration (top), production rate (middle), and loss rate (bottom panel) at the O^+ peak, as a function of the solar cycle factor. Dotted lines in the bottom panel indicate the contributions of two different chemical reactions to the total loss rate.

Although we must consider transport when solving for O^+, we can estimate the peak concentration using a simple balance of production and loss. For S less than two, this approximation reproduces the peak concentration to within 20%. At higher S values, diffusion becomes increasingly important, but the approximation is still within 50% of the rigorous calculation. Even given these differences, the qualitative morphology of the two solutions is the same. The shape of the peak concentration curve in the top panel of Figure 39 is therefore explained by the production and loss terms plotted below it.

From the middle panel of Figure 39, we immediately conclude that production is responsible for the observed maximum near S = 2. The production curve is actually a convolution of the neutral O density and the incident photon flux. Based on our solar irradiance model, we know the photon flux increases linearly with S. The O density is a more complicated function. At Z ~ 1, where the O^+ peak resides, the neutral atomic oxygen concentration undergoes a factor of eight decrease from S = 0 to 6, concomitant with the increases in neutral gas temperature (Figure 27). This follows from the inverse relationship between temperature and total concentration at a fixed pressure. The O concentration does not follow this relationship exactly, as some of the decrease is offset by increased dissociation of O_2. The net result is still a substantial decrease in O at Z = 1. It is the convolution of the linearly increasing photon flux and decreasing O concentration that gives the O^+ production curve seen in Figure 39.

In the case of the loss rate, we again have a combination of terms. For low S values, reactions with both N_2 and O_2 contribute roughly equally to the total loss rate. As S increases, the concentration of O_2 rapidly decreases, to the point its contribution to the loss rate becomes negligible. This leaves N_2 to control the total loss. Again, because of the inverse relationship between total concentration and temperature, as well as increased dissociation, N_2 undergoes a significant decrease with S at Z = 1. However, this decrease is offset by a quadratic increase to

the rate coefficient at high temperatures [*St.-Maurice and Torr*, 1978]. Combined, the two trends give the total loss rate a different shape than the production rate curve.

While production alone determines the local O^+ concentration maximum near $S = 2$, the secondary increase, for S values greater than five, results from the total loss rate decreasing faster than the production rate.

7.4.2. N^+ Response

We can also examine the terms responsible for the rapid increase to N^+. The three panels of Figure 40 present the N^+ concentration (cm^{-3}), production rate ($cm^{-3} s^{-1}$), and loss rate (s^{-1}), all evaluated at the peak in the N^+ profile. The curves are plotted as a function of the solar cycle factor, S. The concentration, in the top panel, is on a logarithmic scale, while the other two panels are on linear scales.

As was the case for O^+, the only significant source of N^+ is via ionization. In this case, however, there are two paths: either dissociative ionization of N_2 or direct ionization of $N(^4S)$. The contribution from each is represented by dotted lines in the middle panel of Figure 40. The production of N^+ via N_2 exhibits a trend similar to the production rate of O^+ (Figure 39). This is because both cases involve the convolution of a linearly increasing photon flux with a decreasing neutral gas concentration. On the other hand, the production of N^+ via direct ionization of $N(^4S)$ exhibits a continuous increase because both the photon flux and atomic nitrogen concentration are increasing with S. Recall that $N(^4S)$ concentrations increase with S due to the enhanced dissociation of N_2 (see Figure 30).

The total N^+ loss rate is governed by reactions with both molecular and atomic oxygen (γ_{11}, γ_{12}, and γ_{13} in Table 2). The rate coefficients for loss via O_2 are more than two orders of magnitude greater than the reaction with O. This makes O_2 the dominant loss mechanism up to roughly $S = 2$, even as molecular oxygen is rapidly dissociated. Beyond $S = 2$, reactions with O
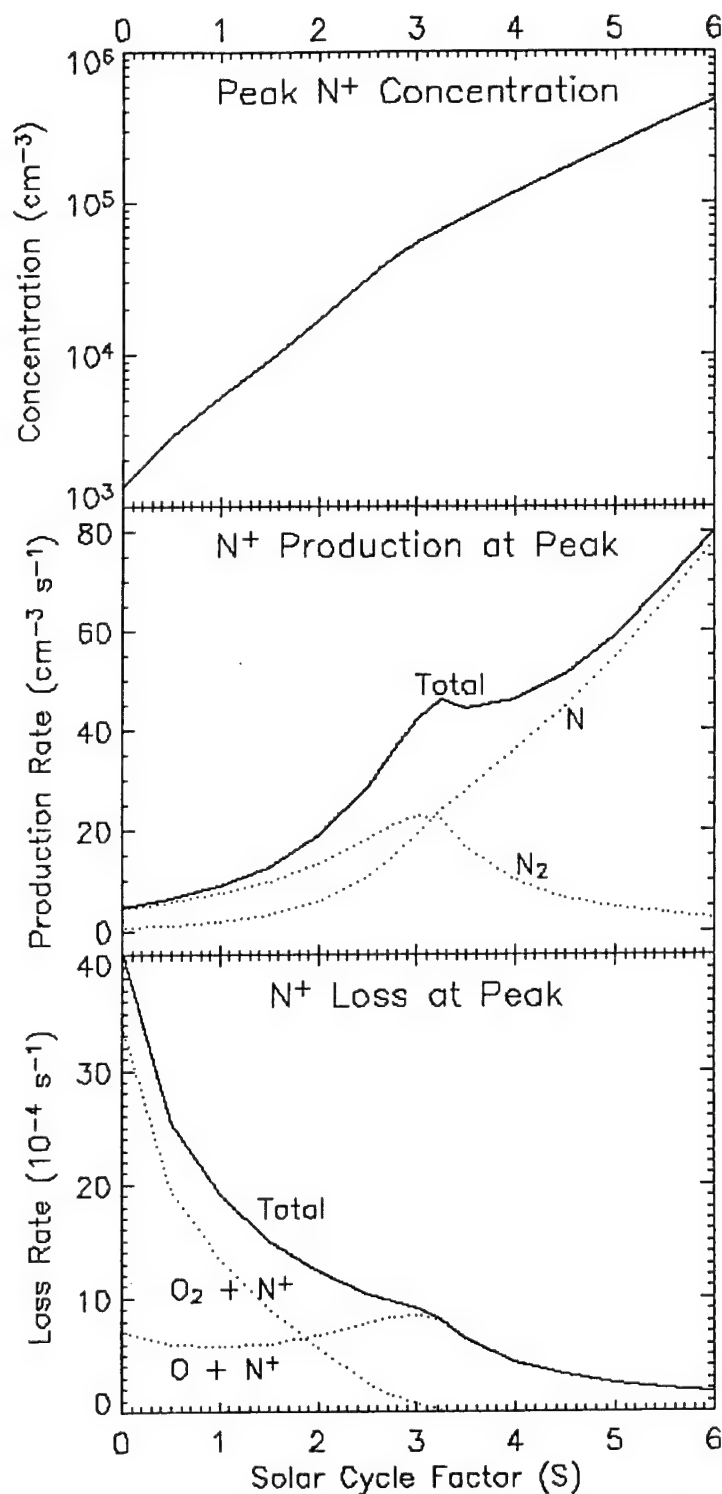
Figure 40. Three panels showing the concentration (top), production rate (middle), and loss rate (bottom panel) at the N$^+$ peak, as a function of the solar cycle factor. Dotted lines in the middle panel indicate the contribution of dissociative ionization (N$_2$) and direct ionization (N) to the total production rate. Dotted lines in the bottom panel indicate the contributions of two different chemical reactions to the total loss rate.

dominate, and the total loss rate is governed by the neutral oxygen concentration. It is important to note none of the rate coefficients for these minor chemical reactions are very well established, nor do they include any temperature dependence. A strong temperature dependence, such as is observed in the O^+ reactions, would alter the results shown in Figure 40.

Just as was the case for O^+, a rigorous calculation of the N^+ concentration must include the effects of transport; however, the simple balance of production and loss reproduces the peak N^+ concentration to within 20% over the full range of S. We can therefore understand the N^+ morphology in terms of the production and loss curves, and these curves are fairly straightforward to interpret. Neglecting a knee in the production rate near S = 3, the total production rate increases monotonically, while the total loss rate monotonically decreases. A convolution of these two trends produces the rapid increase to the peak N^+ concentration.

7.5. Impact of Extreme Solar Maximum Conditions

7.5.1. Neutral Mass Density

Recall from equation (14) the orbital decay rate for a satellite is directly proportional to the atmospheric mass density. Figure 41 displays a contour plot of the global mean mass density (kg/m^3) as a function of both altitude and solar cycle. Given the near exponential increase observed in the exospheric temperature (Figure 27), the thermospheric scale heights increase significantly. However, since the density at a given altitude is related to the scale height through an exponential, the mass density does not exhibit a similarly rapid increase with S. In addition, at high S values, compositional changes brought on by increased dissociation favor lighter atomic species over molecular ones. The result is a fairly slow rise in the mass density at a given altitude.

At 275 km, the mass density varies by a factor of 3.2 over the course of a normal solar cycle, S = 0 to 1. At S = 6 the mass density is only 18.5 times greater than S = 0, slightly less than that

Mass Density as a Function of Solar Cycle
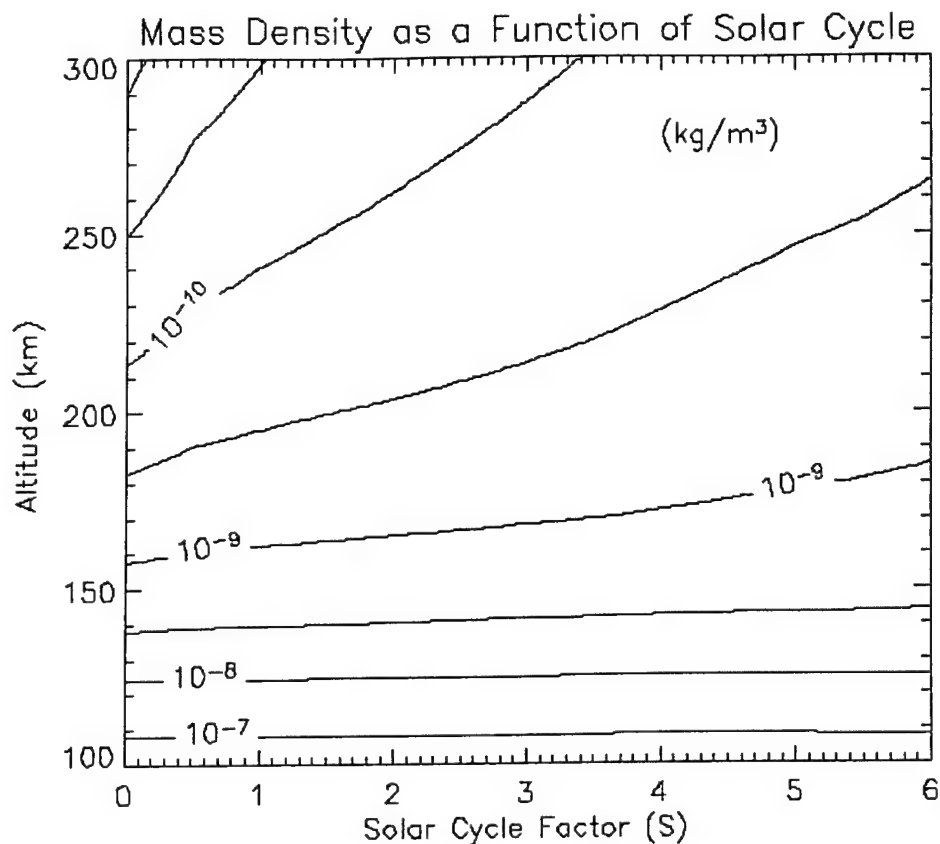
Figure 41. A contour plot of the global mean neutral mass density (kg/m^3), plotted as a function of the solar cycle factor, which ranges from normal solar minimum (S=0) to an extreme maximum (S=6).

predicted by simple linear extrapolation of the normal solar cycle variation. Compare this to the 30-fold decrease predicted over a much smaller S range under Maunder Minimum conditions (section 6.5.1). Satellites in low-Earth orbit would experience greater drag during extreme solar maximum conditions, just not as great as might be guessed from the change in the neutral gas temperatures.

At low altitudes, the neutral temperature, and hence the mass density, varies much less. At an altitude of 130 km, the mass density increases by only 18% between S = 0 and 6, as compared to 5% over the normal solar cycle range.

7.5.2. Operational Ionospheric Parameters

The critical frequency for ordinary wave reflection off the F-region ionosphere (f_oF_2) is

approximated by the expression

$$f_oF_2 (kHz) = 9\sqrt{n_e(cm^{-3})}\,,\qquad\qquad(15)$$

which gives the frequency in kHz as a function of the total electron density (cm^{-3}). Figure 42

displays both the critical frequency and total electron content (TEC) computed as a function of

the solar cycle factor. Since the frequency goes as the square root of the electron density, it

obviously reflects the plateau feature described previously in Figure 37 and Figure 38. TEC

shows an inflection near S = 2 as well, but continues to increases monotonically over the entire

range. We have previously described TEC as a convolution of the peak electron density (N_mF_2)

and a slab thickness. Based on the response of TEC versus f_oF_2, we can conclude the slab

thickness must increase rapidly with S.
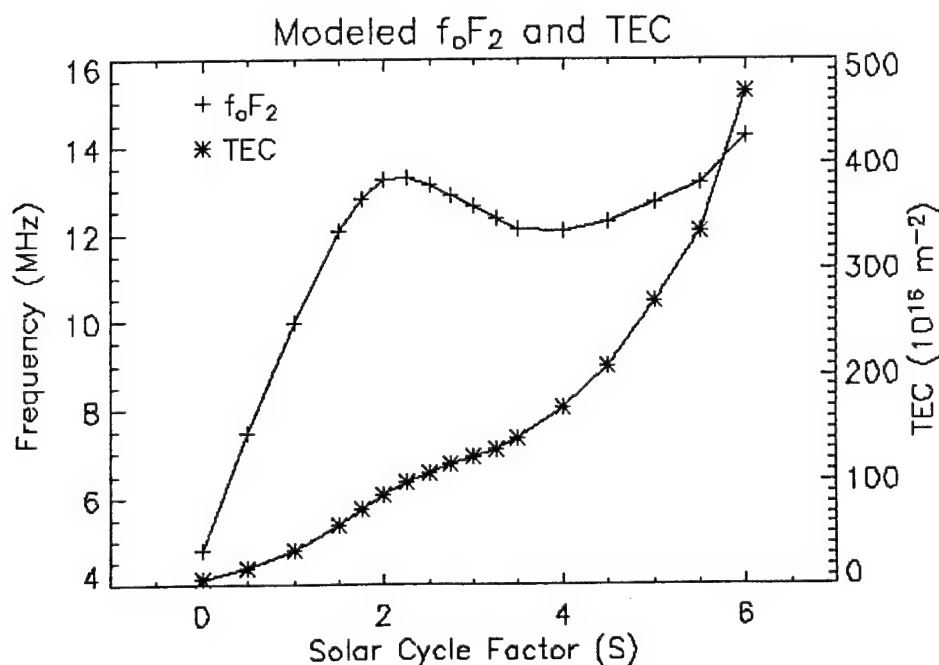
Figure 42. Plots of both the ionospheric F_2 region critical frequency (f_oF_2) and total electron content (TEC) as a function of the solar cycle factor, which ranges from normal solar minimum (S=0) to an extreme maximum (S=6).

In describing the relationship between the TEC and N_mF_2, it is common to derive an effective slab thickness as simply TEC divided by N_mF_2. The topside F-region electron density is, in fact, well approximated by an exponential decrease, governed by the plasma scale height. An estimate of TEC can thus be found by integrating this exponential from the height of peak electron density altitude, up to infinity. This results in the simple relationship TEC = $N_mF_2 \times H_p$, where H_p is the plasma scale height. Such an approximation neglects the contribution of the E-region and bottomside F-region, and assumes H_p is constant, but is a reasonable first order estimate to TEC. The effective slab thickness is then equivalent to the topside scale height. Since H_p goes as the plasma temperature (T_p), so should the slab thickness. This simple dependence merely reflects expansion and contraction of the slab with temperature.

Figure 43 gives the effective slab thickness as a function of temperature. Two curves are shown, one corresponds to using the exospheric plasma temperature (T_p) as the independent variable, the other uses the neutral gas temperature (T_n). Over the range of temperatures shown,
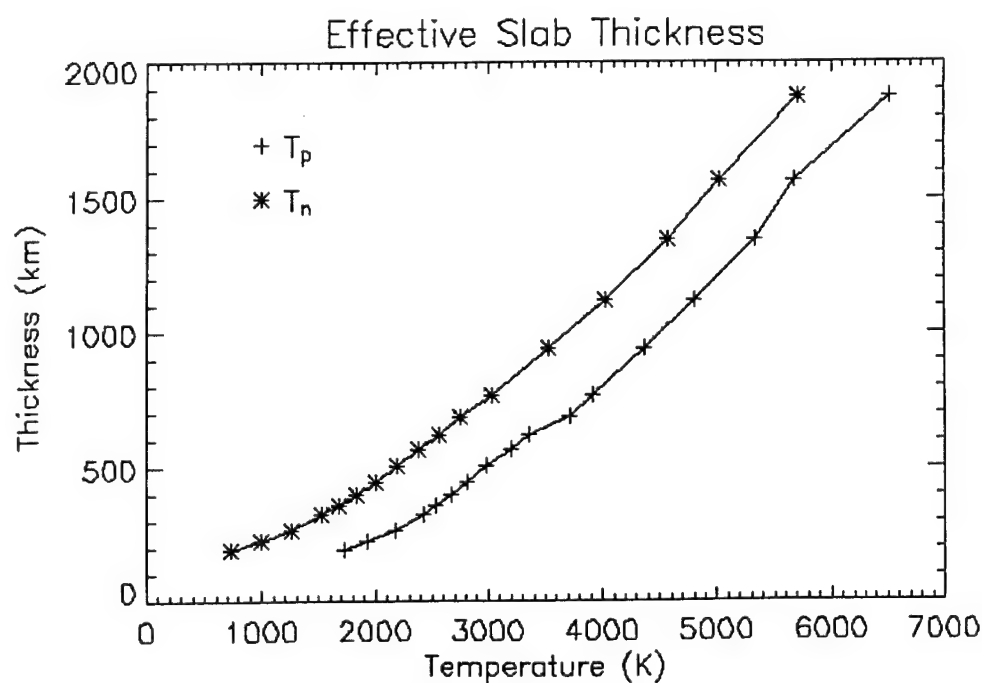
Figure 43. The effective slab thickness, found by dividing TEC by N_mF_2, plotted as a function of the exospheric temperature, both neutral (T_n) and plasma (T_p).

the slab thickness is relatively linear. Deviations from linearity can be attributed both to our neglect of the bottomside F-region contribution, as well as the variation of temperature with height. Note the difference between the two curves is merely an offset, reflecting the strong coupling between the neutral and plasma temperatures.

These relationships raise the possibility of using a combination of TEC and f_oF_2 measurements, which are routinely available at high time resolution, to infer exospheric temperatures. An extensive climatological study would be needed to calibrate the relationships, but this could be useful as a way to monitor temperatures during large solar flares and geomagnetic storms.

The height of the F-region also varies significantly with S, again due to the expansion of the thermosphere with temperature. In Figure 44 we plot the N_mF_2 altitude, H_mF_2, as a function of the solar cycle factor. The curve reflects the near exponential increase in temperature described
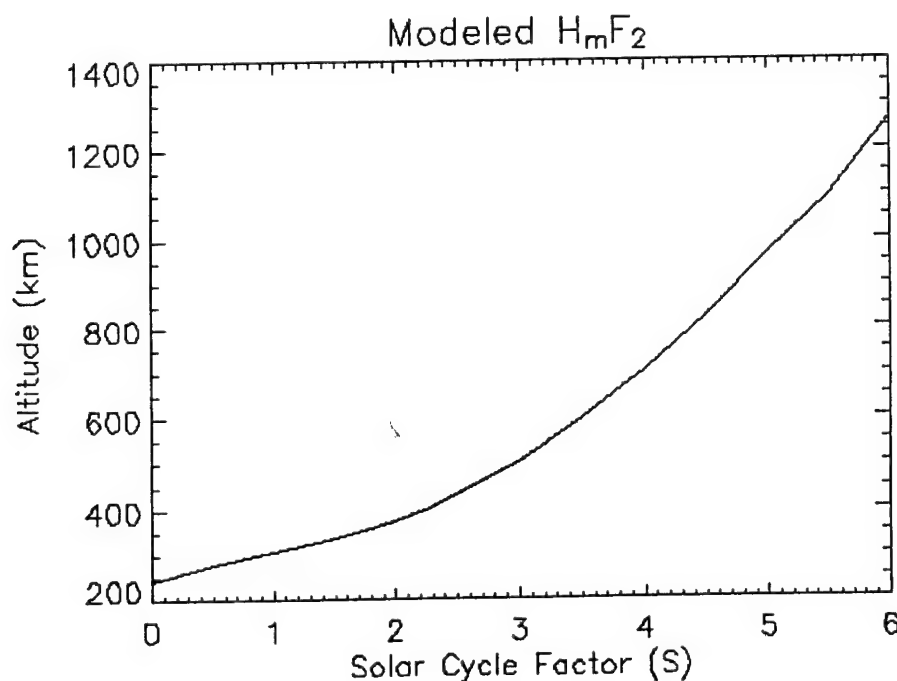
Figure 44. The height of the ionospheric F_2 region peak (H_mF_2) as a function of the solar cycle factor, which ranges from normal solar minimum (S=0) to an extreme maximum (S=6).

previously. The height of the layer is important in the propagation of high-frequency radio waves, since it controls not only the horizontal distance a signal can propagate, but also the strength of the signal reflected off the ionosphere. A doubling of H_mF_2 would reduce the returned signal strength by a factor of four. Assuming the peak height is near 300 km during normal solar cycle conditions, the solar cycle factor would only have to increase to $S \sim 3.5$ in order to double H_mF_2.

7.5.3. Pedersen and Hall Conductivities

In section 6.5.3, we noted the importance of the Hall and Pedersen conductivities to coupling of the magnetosphere and ionosphere. As described previously, the Hall current is generally restricted to a narrow effective altitude range in the lower ionosphere, while contributions to the Pedersen current can extend up through the F-region. Contour plots of the two conductivities as a function of altitude and the solar cycle factor highlight these differences.

Figure 45 displays a contour plot of the Pedersen conductivity, while the Hall conductivity is shown in Figure 46. The Pedersen conductivity exhibits a broad tongue near $S = 2$, corresponding to the electron density morphology described previously. Note even up to altitudes of 400 km, the Pedersen conductivity is within an order of magnitude of its low-altitude peak. Contributions to the Pedersen conductivity thus extend to fairly high altitudes, especially as the solar cycle factor increases. On the other hand, the Hall conductivity is confined to the lowest levels of the ionosphere, dropping an order of magnitude within roughly 20 km of its peak.

The top panel of Figure 47 presents the height-integrated Pedersen and Hall conductivities (conductance) as a function of S; in both cases the integration is over the full altitude range. At S = 0 the two values are roughly equal, but as S increases, the high-altitude contribution to the Pedersen conductance separates it from the Hall. By $S = 6$ the Hall conductance is only 30% of the Pedersen value.
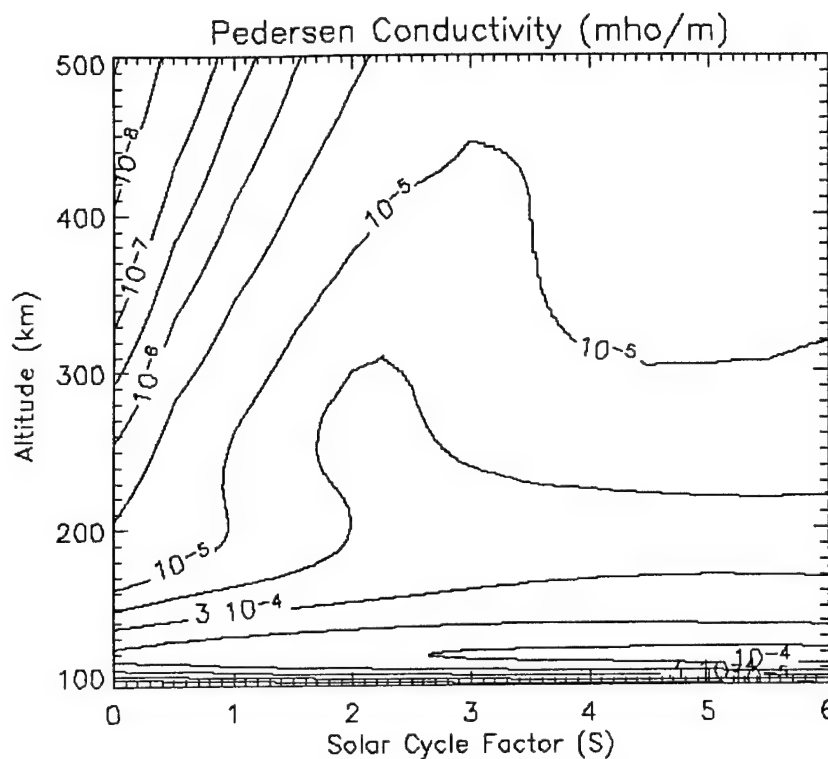
Figure 45. A contour plot of the Pedersen conductivity (mho/m), as a function of altitude (km) and the solar cycle factor.
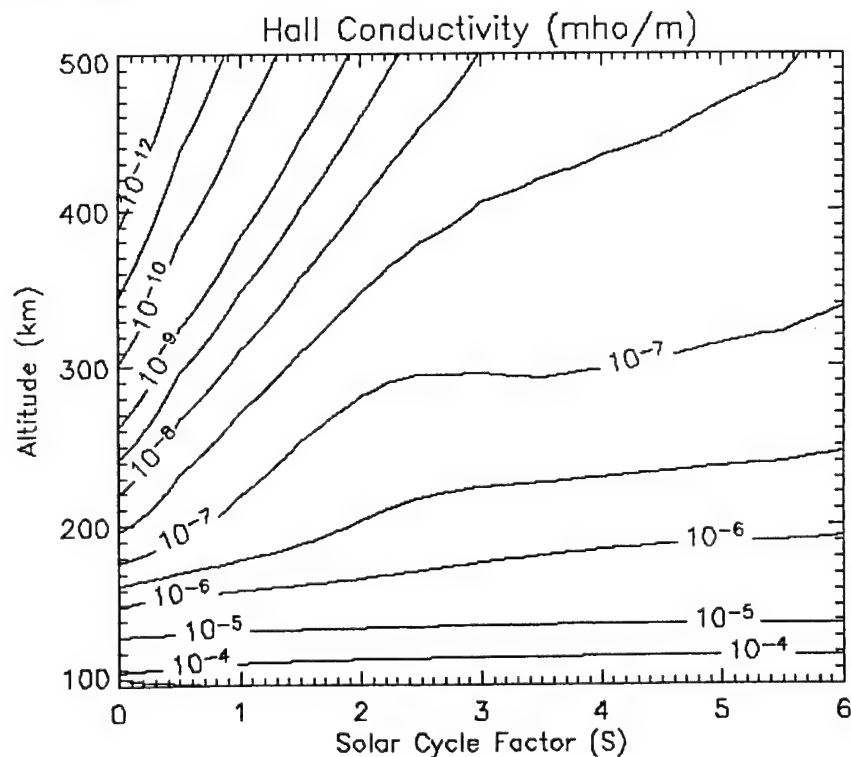
Figure 46. A contour plot of the Hall conductivity (mho/m), as a function of altitude (km) and the solar cycle factor.

Height Integrated Conductivities
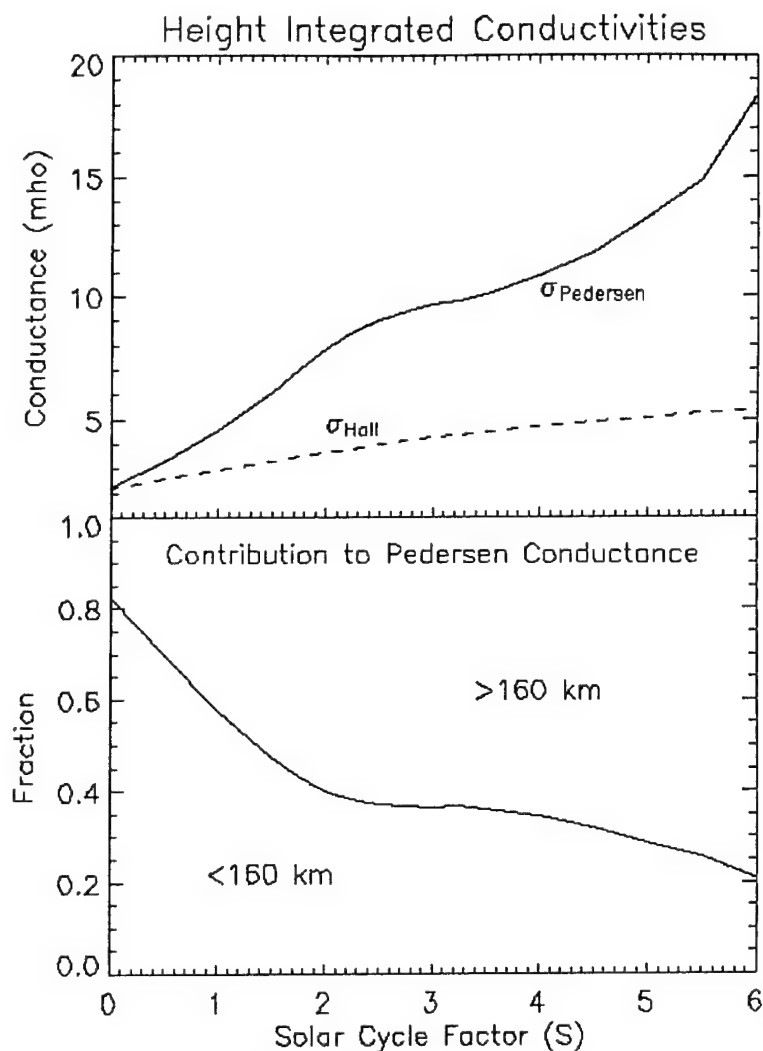
Figure 47. Height integrated conductivities as a function of the solar cycle factor, ranging from S = 0 to 6. The top panel shows the Pedersen (solid) and Hall (dashed) conductance. The bottom panel gives the relative importance of two broad altitude regions (<160 km and >160 km) to the total Pedersen conductance. Essentially all of the Hall conductance is found below 160 km.

In the lower panel of Figure 47, we quantify the importance of the high-altitude component to the total Pedersen conductance. In the panel, the curve delineates the fractional contribution to the total conductance from below 160 km and above 160 km. At S = 0, 80% of the Pedersen conductance comes from below 160 km, but as S increases to six this fraction reverses to roughly 20%. In the case of the Hall conductance, 98% or more of the contribution is from below 160 km, even at S = 6.

These differences have ramifications for the location of current closures. Most closure models currently use a thin-shell assumption, collapsing the entire Pedersen and Hall conductance to a narrow altitude region near 100 km. This assumption is reasonable for a normal solar cycle. During an extreme solar maximum period, the effective altitude range of Pedersen conductivity would expand, while the Hall conductivity would remain confined to the thin low-altitude shell. This would result not only in an increase to the effective altitude range, but a partial separation of the two closure mechanisms.

7.6. Discussion

Even though we examined the response of the thermosphere and ionosphere up to $S = 6$, the results obviously become more speculative as S increases. Fortunately we did not have to take S very far outside our normal solar cycle to find an interesting result – the saturation of O^+.

Corresponding to the saturation of O^+, the peak electron density exhibits an extended plateau beginning near $S = 2$, which equates to a P index of 390. Initial indications of this saturation should be evident at lower P values, especially if the ionospheric observations were made near local noon. However, in recent history the P index has rarely exceeded 300, the latest periods being January and February 1991 when P reached a maximum of 337. So there are likely few days currently available in the observational record to confirm this effect. The other complicating factor is that without coincident measurements of the solar irradiance, it would be difficult to separate saturation effects from the expected nonlinear relationship between F10.7 and EUV flux at high P [*Balan et al.*, 1994a; *Balan et al.*, 1994b; *Richards et al.*, 1994].

As we increase the solar cycle factor to high levels, we must be cognizant of the many assumptions inherent to the model and the possibility they may break down. One of the biggest assumptions is the lower atmosphere remains unaffected. We examined this question as it related to the direct transfer of energy, but there are other complications that were not addressed.

We noted previously the neutral atomic oxygen concentration increases by 60% at the lower boundary, for $S = 1$ to 6. This produces a similar increase in the downward flux of O atoms across the lower boundary. As these atoms recombine in the mesosphere they release 5.12 eV of energy; this additional chemical energy could disrupt our previous assumption of fixed neutral temperatures. Lowering the model boundary to roughly 30 km, as was done by *Roble* [1995], would resolve this and other related questions, but at the same time introduce new complications and assumptions.

The dramatic increase in temperatures can also have unforeseen consequences. As the temperatures increase we have to question many of the chemical reaction rate coefficients. Most of these coefficients have been fit over a narrow temperature window, if at all. Rate coefficients for the minor ions are particularly suspect, since they receive the least attention. And, as we have seen, the minor ion N^+ can become a major ion.

As the temperatures increase to 6000 K, we must also begin to think about the high-energy tail of the population. New reactions, which were previously not considered, might suddenly have a major impact for particles with a few eV of thermal energy. Another concern is the escape of this tail population into the plasmasphere. We have yet to investigate the importance of an O^+ escape flux as the temperatures increase.

CHAPTER 8

CONCLUSIONS AND FUTURE WORK

8.1. Conclusions

We have created a new model representing the coupled, global average ionosphere and thermosphere (GAIT). This model development followed closely the pioneering work of Roble and others [*Roble*, 1995; *Roble and Emery*, 1983; *Roble et al.*, 1987]. The distinction between the GAIT and earlier models is that our development effort focused on making the model independent of the input solar irradiance, and therefore able to accurately respond to different irradiance representations. Toward this end, the model contains an approximate treatment of photoelectrons based on the local equilibrium approach of *Richards and Torr* [1983]. Results from the GAIT model were compared to the empirical MSIS-90 model as well as earlier global average models [*Roble et al.*, 1987] and found to be in reasonable agreement with both.

Large uncertainties remain in several key chemical reaction rates, which, in turn, directly influence the thermospheric energy balance. We examined the sensitivity of the GAIT model to these uncertainties and found even the largest change, an 83% decrease in the excitation rate of CO_2 bending vibration, resulted in only a 12% increase to the exospheric temperature. Given the observed exospheric temperature varies by more than 70% over the course of the solar cycle, none of the known uncertainties fundamentally determines the final result.

We investigated the model's sensitivity to four different EUV irradiance representations. Figure 10 showed the total EUV energy flux predicted by each of the four irradiance models differed considerably. Consistent with the results of *Lean et al.* [2003] we found the NRLEUV model to predict the lowest total energy flux, it also had the smallest dynamic range. Figure 11 showed regardless of which irradiance model was used, the resulting exospheric temperature scaled linearly with the total EUV energy input over the normal solar cycle. This figure also

highlighted that the small dynamic range of the NRLEUV model resulted in non-physical temperatures. By changing just one or two of the parameters described in Table 3, we were able to bring the VUV, EUVAC, and S2000 models to within 2% of the MSIS-90 results. However, even after modifying all of the key rates and inputs, we were unable to get agreement to better than 9% at both solar minimum and maximum using the NRLEUV model. We concluded the dynamic range of the NRLEUV model is not large enough to support the observed temperature variation.

We next examined the response of the coupled thermosphere and ionosphere to extreme solar irradiance inputs. To do this we justified an extrapolation of the solar irradiance based on observations of Sun-like stars [*Baliunas and Jastrow*, 1990; *Radick*, 2003; *Radick et al.*, 1998; *White et al.*, 1992], as well as analysis of the cosmogenic isotope record [*Eddy*, 1976; *Webber and Higbie*, 2003]. We attempted to recreate Maunder Minimum type conditions by reducing normal solar minimum flux levels by an amount equal to a typical solar cycle variation. Our findings indicated a dramatic morphological change in which NO^+ replaced O^+ as the dominant F-region ion. These results were found to be largely independent of the choice of solar irradiance model. Figure 23 illustrated when the transition is plotted as a function of temperature, all four irradiance models give nearly identical results.

Similar arguments regarding Sun-like stars and cosmogenic isotopes were used to justify our exploration of significantly higher solar flux levels. In this case we had less guidance on a reasonable upper limit, and instead chose to increase the flux until the model broke. We found this breaking point at irradiance levels roughly six times the normal solar cycle variation. Within this range there were again a number of interesting ionospheric effects. The first was a plateau in the peak electron density; the plateau appeared when the irradiance reached twice the normal solar cycle variation and remained relatively steady up to $S = 6$. We attributed this plateau primarily to a corresponding peak in the O^+ production rate (section 7.4.1).

Over the range S = 0 to 6, the predicted concentration of N^+ showed a dramatic surge,
increasing more than two orders of magnitude, and coming within a factor of four of the O^+
concentration. This surge was attributed primarily to additional dissociation of N_2, resulting in
more $N(^4S)$ avaible for ionization. But we noted the rate coefficients for reactions involving N^+
are not well established and do not currently contain any temperature dependence. Updates to
these coefficients could alter these results.

A graphical summary of our findings is represented in Figure 48. Here we show the global
mean electron density over the range S = −1 to 6, with pressure as the vertical coordinate. A
dashed line indicates the pressure of the peak electron density. Similar figures have been shown
previously, but this one highlights the entire range we have explored. Although the F- and E-
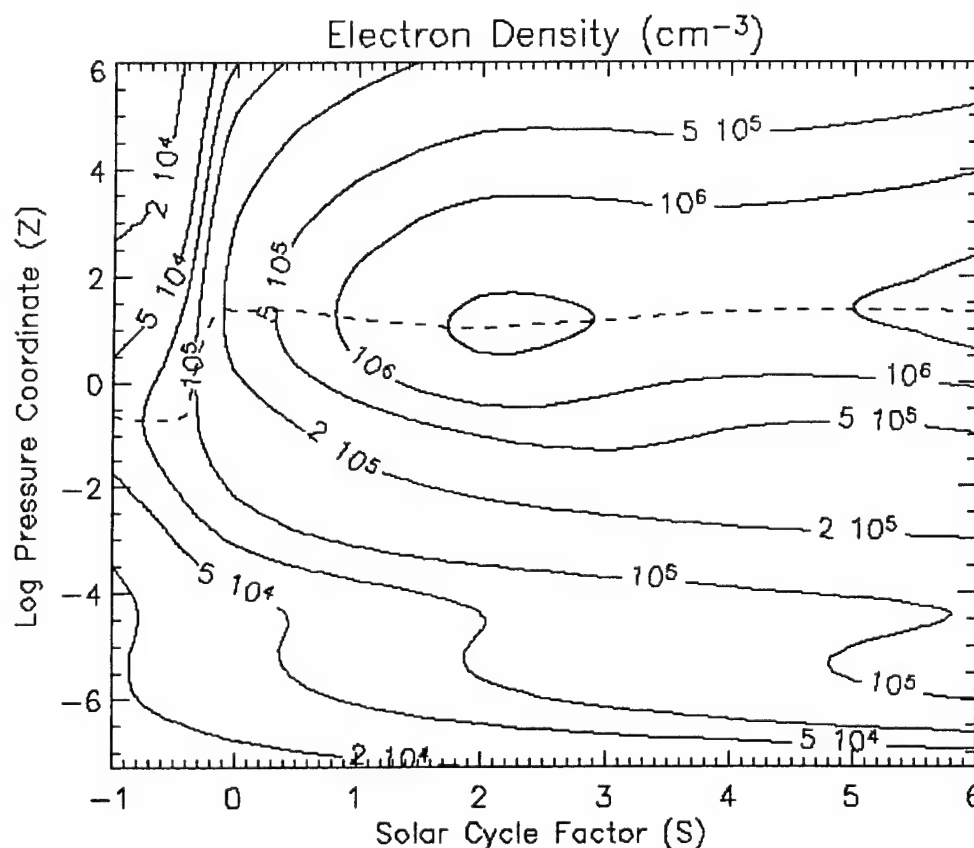
Figure 48. A contour plot of the global mean electron density (cm^{-3}), shown as a function of the solar cycle factor, which ranges from S= −1 to 6. The dashed line indicates the pressure of the peak electron density.

regions of the ionosphere scale fairly linearly over the normal solar cycle, it is apparent

from the figure interesting changes are predicted just outside these normal bounds. The solar

irradiance does not have to decrease much before we begin the transition to an ionosphere

dominated by molecular ions, rather than O^+. On the high end, evidence for a plateau in the

electron density should become apparent even before $S = 2$, although we will require coincident

measurements of the EUV irradiance to distinguish this plateau from the nonlinear behavior of

the F10.7 solar proxy.

There will of course remain the question of whether the GAIT model can realistically

represent the thermosphere and ionosphere under such extreme solar conditions. We have

already pointed out the issue of appropriate boundary conditions, as well as the possibility new

physical processes must be included. However, the fact we did not have to extrapolate too far

from the normal solar cycle to obtain these effects supports our belief the results are, in fact,

physically representative of the true response. We can only hope the Sun will oblige us with a

new Maunder Minimum or extreme maximum, in order to test these predictions.

8.2. Future Work

Having demonstrated the utility of the GAIT model as a predictive tool for both normal and

extreme solar conditions, we have opened a number of avenues for future research. Under

normal solar conditions, the GAIT model is useful for testing the impact of new rate coefficients

and chemical schemes. *Sharma and Roble* [2001] have already used their own global average

model for this purpose. As chemical reaction rates are updated, we can now use the GAIT model

in a similar fashion.

Another avenue of research is into the time-dependent behavior of the model. The results

reported so far reflect only steady-state solutions, but the internal equations are, in fact, time-

dependent. We know the time constants for recombination are much lower in the E-region than

in the F-region ionosphere. An interesting area of future work would be to run the model to

steady state, and then turn off the solar input. In the case of the Maunder Minimum ionosphere, it is possible once the solar input is turned off, the morphology could change from NO^+ dominated back to O^+ dominated, due to the fast recombination of NO^+.

Another approach would be to drop the global average in favor of a hemispheric or longitudinal average. We could then run the model on a 24-hour cycle, varying the effective solar zenith angle as the profile rotates in time. This approach obviously neglects important transport effects, but it would be interesting to see how the results compare to a full global average.

The GAIT model is also ideally suited to explore the time-dependent response to solar flares. Recent measurements by the Solar EUV Experiment (SEE) on the TIMED satellite have captured the irradiance changes that occur during moderate to major solar flares [*Woods et al.*, 2003]. This data can be used to generate a simple flare-time irradiance model. We have already used this approach in conjunction with the Time-Dependent Ionospheric Model (TDIM) [*Schunk*, 1988] to investigate the temporal flare response of the ionosphere [*Smithtro et al.*, 2003]. The TDIM does not include a self-consistent photoelectron model, and so in that study we were forced to make assumptions regarding secondary ionization and the heating of thermal electrons. We were also forced to neglect concomitant changes in the thermosphere, since the TDIM specifies the thermosphere using MSIS. *Solomon* [2003] suggested the neutral gas temperature increases significantly during major solar flares. This would, in turn, affect the structure of the underlying thermosphere and hence the ionospheric response. With the GAIT model, we are in a position to simultaneously investigate the large-scale response of the coupled thermosphere and ionosphere to these flares.

Of course, no model is ever complete, and we can envision a number of improvements to the GAIT model. Some modifications would be relatively straightforward, such as including more species, testing different chemical schemes, or treating species such as $N(^4S)$ as major constituents rather than minor ones. Others, such as lowering the model boundary into the

mesosphere, would require a major new effort. In each case, the important question is whether the effort is justified by new physical insights. But as we learned from this dissertation, we typically do not know the answer until the work is done.

DISCLAIMER: The views expressed in this dissertation are those of the author and do not necessarily reflect the official policy or position of the U.S. Air Force, the Department of Defense, or the U.S. Government.

REFERENCES

Allen, M., J. I. Lunine, and Y. L. Yung (1984), The vertical distribution of ozone in the mesosphere and lower thermosphere, *J. Geophys. Res., 89(D3)*, 4841-4872.

Bailey, S. M., C. A. Barth, and S. C. Solomon (2002), A model of nitric oxide in the lower thermosphere, *J. Geophys. Res., 107,* doi:10.1029/2001JA000258.

Bailey, S. M., T. N. Woods, C. A. Barth, and S. C. Solomon (2000), Measurements of the solar soft X-ray irradiance from the Student Nitric Oxide Explorer, *Geophys. Res. Lett., 105,* 27179.

Balan, N., G. J. Bailey, B. Jenkins, P. B. Rao, and R. J. Moffett (1994a), Variations of ionospheric ionization and related solar fluxes during an intense solar cycle, *J. Geophys. Res., 99(A2)*, 2243-2253.

Balan, N., G. J. Bailey, and R. J. Moffett (1994b), Modeling studies of ionospheric variations during an intense solar cycle, *J. Geophys. Res., 99(A9)*, 17467-17475.

Baliunas, S. L., and R. Jastrow (1990), Evidence for long-term brightness changes of solar-type stars, *Nature, 348,* 520-523.

Bates, D. R. (1951), The temperature of the upper atmosphere, *Proc. Phys. Soc. London, 64B,* 805-821.

Bougher, S. W., D. M. Hunten, and R. G. Roble (1994), CO_2 cooling in terrestrial planet thermospheres, *J. Geophys. Res., 99(E7),* 14609-14622.

Chapman, S., and T. G. Cowling (1952), *The Mathematical Theory of Non-Uniform Gases*, 423 pp., Cambridge Univ. Press, New York.

Clark, I. D., and R. P. Wayne (1970), Kinetics of the reaction between atomic nitrogen and molecular oxygen in the ground ($^3\Sigma_g$) and the first excited ($^1\Delta_g$) states, *Proc. R. Soc. London, Ser. A, A316,* 359.

Colegrove, F. D., F. S. Johnson, and W. B. Hanson (1966), Atmospheric composition in the lower thermosphere, *J. Geophys. Res., 71(9)*, 2227-2236.

Covington, A. E. (1947), Microwave solar noise observations during the partial eclipse of November 23, 1946, *Nature, 159,* 405-406.

Craig, R. A., and J. C. Gille (1969), Cooling of the thermosphere by atomic oxygen, *J. Atmos. Sci., 26,* 205-209.

Dickinson, R. E. (1984), Infrared radiative cooling in the mesosphere and lower thermosphere, *J. Atmos. Terr. Phys., 46(11),* 995-1008.

Duff, J., and R. D. Sharma (1997), Quasiclassical trajectory study of the relaxation of vibrationally excited NO by collisions with O atoms, *J. Chem. Soc. Faraday Trans., 93*, 2645.

Dodd, J. A., R. B. Lockwood, E. S. Hwang, S. M. Miller, and S. J. Lipson (1999), Vibrational relaxation of NO(v=1) by oxygen atoms, *J. Chem. Phys., 111(8)*, 3498-3507.

Durrance, S. T., and G. E. Thomas (1979), The 63 μm radiation field in the Earth's thermosphere and its influence on the atomic hydrogen temperature, *Planet. Space Sci., 27*, 795-800.

Eddy, J. A. (1976), The Maunder minimum, *Science, 192*, 1189-1202.

Fell, C., J. I. Steinfield, and S. Miller (1990), Quenching of N(^{2}D) by O(^{3}P), *J. Chem. Phys., 92*, 4768.

Fennelly, J. A., and D. G. Torr (1992), Photoionization and photoabsorption cross sections of O, N_2, O_2, and N for aeronomic calculations, *At. Data and Nucl. Data Tables, 51*, 321.

Fernando, R. P., and I. W. M. Smith (1979), Vibrational relaxation of NO by atomic oxygen, *Chem. Phys. Lett., 66(2)*, 218-222.

Fomichev, V. I., J. P. Blanchet, and D. S. Turner (1998), Matrix parameterization of the 15 μm CO_2 band cooling in the middle and upper atmosphere for variable CO_2 concentration, *J. Geophys. Res. 103(D10)*, 11505-11528.

Glenar, D. A., E. Bleuler, and J. S. Nisbet (1978), The energy balance of the nighttime thermosphere, *J. Geophys. Res., 83(A12)*, 5550-5562.

Gordiets, B. F., Y. N. Kulikov, M. N. Markov, and M. Y. Marov (1982), Numerical modeling of the thermospheric heat budget, *J. Geophys. Res., 87(A6)*, 4504-4514.

Green, A. E. S., and R. S. Stolarski (1972), Analytic models of electron impact excitation cross sections, *J. Atmos. Terr. Phys., 34*, 1703-1717.

Grossmann, K. U., and D. Offermann (1978), Atomic oxygen emission at 63 μm as a cooling mechanism in the thermosphere and ionosphere, *Nature, 276*, 594-595.

Grossmann, K. U., and K. Vollmann (1997), Thermal infrared measurements in the middle and upper atmosphere, *Adv. Space Res., 19*, 631-638.

Hargreaves, J. K. (1992), *The Solar Terrestrial Environment*, 420 pp., Cambridge Univ. Press, Cambridge.

Hedin, A. E. (1991), Extension of the MSIS Thermosphere Model into the Middle and Lower Atmosphere, *J. Geophys. Res., 96(A2)*, 1159.

Hinteregger, H. E., K. Fukui, and B. R. Gilson (1981), Observational, reference and model data on solar EUV, from measurements on AE-E, *Geophys. Res. Lett.*, 8, 1147.

Hoyt, D. V., and K. H. Schatten (1998a), Group sunspot numbers: A new solar activity reconstruction, part 1, *Sol. Phys., 179*, 189-219.

Hoyt, D. V., and K. H. Schatten (1998b), Group sunspot numbers: A new solar activity reconstruction, part 2, *Sol. Phys., 181,* 491-512.

Jackman, C. H., R. H. Garvey, and A. E. S. Green (1977), Electron impact on atmospheric gases I. Updated cross sections, *J. Geophys. Res., 82(32),* 5081-5090.

Jet Propulsion Laboratory (2003), Chemical kinetics and photochemical data for use in atmospheric studies, *JPL 02-25,* Evaluation 14.

Johnson, F. S., and B. Gottlieb (1970), Eddy mixing and circulation at ionospheric levels, *Planet. Space Sci., 18,* 1707-1718.

Klein, F. S., and J. T. Herron (1964), Mass-spectrometric study of the reactions of O atoms with NO and NO_2 , *J. Chem. Phys., 41,* 1285.

Kockarts, G. (1980), Nitric oxide cooling in the terrestrial thermosphere, *Geophys. Res. Lett., 7(2),* 137-140.

Kockarts, G., and W. Peetermans (1970), Atomic oxygen infrared emission in the Earth's upper atmosphere, *Planet. Space Sci., 18,* 271-285.

Lean, J. L. (2004), private communication.

Lean, J. L., G. J. Rottman, H. L. Kyle, T. N. Woods, J. R. Hickey, and L. C. Puga (1997), Detection and parameterization of variations in the solar mid and near ultraviolet radiation (200 to 400 nm), *J. Geophys. Res., 102,* 29939-29956.

Lean, J. L., H. P. Warren, J. T. Mariska, and J. Bishop (2003), A new model of solar EUV irradiance variability 2. Comparisons with empirical models and observations and implications for space weather, *J. Geophys. Res., 108(A2),* 1059, doi:10.1029/2001JA009238.

Lean, J. L., O. R. White, W. C Livingston, and J. M. Picone (2001), Variability of a composite chromospheric irradiance index during the 11-year activity cycle and over longer time periods, *J. Geophys. Res., 106(A6),* 10645-10658, doi:10.1029/2000JA000340.

Lee, J. H., J. V. Michael, W. A. Payne, and L. H. Stief (1978), Absolute rate of the reaction of $N(^4S)$ with NO from 196-400 K with DF-RF and FP-RF techniques, *J. Chem. Phys., 69,* 3069.

Lee, P. C., and J. B. Nee (2000), Detection of $O(^1D)$ produced in the photodissociation of O_2. I. Identification of the $^3\Sigma_u$ and $^3\Pi_u$ Rydberg states in 113-130 nm, *J. Chem. Phys., 112(4),* 1763-1768.

Lettau, H. (1951), Diffusion in the upper atmosphere, in *Compendium of Meteorology,* edited by T. Malone, pp. 320-335, AMS, New York.

Minschwaner K., R. J. Salawitch, and M. B. McElroy (1993a), Absorption of solar radiation by O_2: implications for O_3 and lifetimes of N_2O, $CFCl_3$, and CF_2Cl_2, *J. Geophys. Res., 98(D6),* 10543-10561.

Minschwaner K., and D. E. Siskind (1993b), A new calculation of nitric oxide photolysis in the stratosphere, mesosphere, and lower thermosphere, *J. Geophys. Res., 98(D11)*, 20401-20412.

Mlynczak, M. G., and S. Solomon (1993), A detailed evaluation of the heating efficiency in the middle atmosphere, *J. Geophys. Res., 98(D6)*, 10517-10541.

Nee, J. B., and P. C. Lee (1997), Detection of $O(^1D)$ produced in the photodissociation of O_2 in the Schumann-Runge continuum, *J. Phys. Chem. A, 101,* 6653-6657.

Nicolet, M. (1985), Aeronomical aspects of mesospheric photodissociation: processes resulting from the solar H Lyman-alpha line, *Planet. Space Sci.*, 33(1), 69-80, 1985.

Pollock, D. S., G. B. I. Scott, and L. F. Phillips (1993), Rate constant for the quenching of $CO_2(010)$ by atomic oxygen, *Geophys. Res. Lett., 20,* 727-729.

Radick, R. R. (2003), Variability of sunlike stars, *J. Atmos. Terr. Phys., 65,* 105-112.

Radick, R. R., G. W. Lockwood, B. A. Skiff, and S. L. Baliunas (1998), Patterns of variation among Sun-like stars, *Astrophys. J. Suppl. Ser., 118,* 239-258.

Rees, M. H. (1989), *Physics and Chemistry of the Upper Atmosphere*, 289 pp., Cambridge Univ. Press, Cambridge.

Rees, M. H., and R. G. Roble (1975), Observations and theory of the formation of stable auroral red arcs, *Rev. Geophys., 13(1)*, 201-242.

Richards, P. G., J. A. Fennelly, and D. G. Torr. (1994), EUVAC: A solar EUV flux model for aeronomic calculations, *J. Geophys. Res., 99(A5)*, 8981-8992.

Richards, P. G., and D. G. Torr (1983), A simple theoretical model for calculating and parameterizing the ionospheric photoelectron flux, *J. Geophys. Res., 88(A3)*, 2155-2162.

Richards, P. G., and D. G. Torr (1988), Ratios of photoelectron to EUV ionization rates for aeronomic studies, *J. Geophys. Res., 93(A5),* 4060-4066.

Richards, P. G., D. G. Torr, and M. R. Torr (1981), Photodissociation of N_2: A significant source of thermospheric atomic nitrogen, *J. Geophys. Res., 86(A3)*, 1495-1498.

Rishbeth, H., and R. Edwards (1989), The isobaric F2-layer, *J. Atmos. Terr. Phys., 51*, 321-338.

Roble, R. G. (1995), Energetics of the mesosphere and thermosphere, in *The Upper Mesosphere and Lower Thermosphere: A Review of Experiment and Theory, Geophys. Monogr. Ser.,* vol. 87, edited by R. M. Johnson and T. L. Killeen, pp. 1-21, AGU, Washington, D.C.

Roble, R. G., and B. A. Emery (1983), On the global mean temperature of the thermosphere, *Planet. Space Sci., 31(6)*, 597-614.

Roble, R. G., E. C. Ridley, and R. E. Dickinson (1987), On the global mean structure of the thermosphere, *J. Geophys. Res., 92(A8)*, 8745-8758.

Rodrigo, R., J. J. Lopez-Moreno, M. Lopez-Puertas, R. Moreno, and A. Molina (1986), Neutral atmospheric composition between 60 and 220 km: A theoretical model for mid-latitudes, *Planet. Space Sci.*, *34(8)*, 723-743.

Schunk, R. W. (1988), A mathematical model of the middle and high latitude ionosphere, *PAGEOPH*, *127*, 255-303.

Schunk, R. W., and A. F. Nagy (2000), *Ionospheres: Physics, Plasma Physics, and Chemistry*, 554 pp., Cambridge Univ. Press, Cambridge.

Sharma, R. D., and R. G. Roble (2001), Impact of the new rate coefficients for the O atom vibrational deactivation and photodissociation of NO on the temperature and density structure of the terrestrial atmosphere, *J. Geophys. Res.*, *106(A10)*, 21343-21350.

Sharma, R. D., and P. P. Wintersteiner (1990), Role of carbon dioxide in cooling planetary thermospheres, *Geophys. Res. Lett.*, *17(12)*, 2201-2204.

Sharma, R. D., B. Zygelman, F. von Esse, and A. Dalgarno (1994), On the relationship between the population of the fine structure levels of the ground electronic state of atomic oxygen and the translational temperature, *Geophys. Res. Lett.*, *21(16)*, 1731-1734.

Shemansky, D. E. (1972), CO_2 extinction coefficient 1700-3000 Å, *J. Chem. Phys.*, *56(4)*, 1582-1587.

Shved, G. M., L. E. Khvorostovskaya, I. Y. Potekhin, A. I. Demyanikov, A. A. Kutepov, and V. I. Fomichev (1991), Measurement of the quenching rate constant for collisions $CO_2(010)$-O: The importance of the rate constant magnitude for the thermal regime and radiation of the lower thermosphere, *Atmos. Oceanic Phys.*, *27*, 431-437.

Smith III, F. L., and C. Smith (1972), Numerical evaluation of Chapman's grazing incidence integral ch(X,χ), *J. Geophys. Res.*, *77(19)*, 3592-3597.

Smithtro, C. G., T. Berkey, D. Thompson, J. J. Sojka, and R. W. Schunk (2003), Observation and Modeling of Ionospheric Dynamics During Major Solar Flares, *Eos Trans. AGU, 84*(46), Fall Meet. Suppl., Abstract SA22B-07.

Solomon, S. C. (2003), Solar ultraviolet and x-ray energy deposition and partitioning in the MLT, *Eos Trans. AGU, 84*(46), Fall Meet. Suppl., Abstract SA31B-01.

Solomon, S. C., P. B. Hays, and V. J. Abreu (1988), The auroral 6300 Å emission: Observations and modeling, *J. Geophys. Res.*, *93(A9)*, 9867-9882.

St.-Maurice, J.-P., and D. G. Torr (1978), Nonthermal rate coefficients in the ionosphere: The reactions of O+ with N2, O2, and NO, *J. Geophys. Res.*, *83(A3)*, 969-977.

Stolarski, R. S. (1976), Energetics of the midlatitude thermosphere, *J. Atmos. Terr. Phys.*, *38*, 863-868.

Strobel, D. F. (1978), Parameterization of the atmospheric heating rate from 15 to 120 km due to O_2 and O_3 absorption of solar radiation, *J. Geophys. Res.*, *83(C12)*, 6225-6230.

Swartz, W. E., and J. S. Nisbet (1972), Revised calculations of F region ambient electron heating by photoelectrons, *J. Geophys. Res.*, *77(31)*, 6259-6261.

Titheridge, J. E. (1998), Temperatures in the upper ionosphere and plasmasphere, *J. Geophys. Res.*, *103(A2)*, 2261-2277.

Tobiska, W. K, T. Woods, F. Eparvier, R. Viereck, L. Floyd, D. Bouwer, G. Rottman, and O. R. White (2000), The SOLAR2000 empirical solar irradiance model and forecast tool, *J. Atmos. Terr. Phys., 62,* 1233-1250.

Torr, M. R., and D. G. Torr (1980), Solar flux variability in the Schumann-Runge continuum as a function of solar cycle 21, *J. Geophys. Res.*, *85(A11)*, 6063-6068.

Torr, M. R., and D. G. Torr (1985), Ionization frequencies for solar cycle 21: Revised, *J. Geophys. Res.*, *90(A7)*, 6675-6678.

Torr, M. R., D. G. Torr, and R. A. Ong (1979), Ionization frequencies for major thermospheric constituents as a function of solar cycle 21, *Geophys. Res. Lett.*, *6(10)*, 771-774.

Trinks, H., and K. H. Fricke (1978), Carbon dioxide concentrations in the lower thermosphere, *J. Geophys. Res.*, *83(A8)*, 3883-3886.

Usoskin, I. G., K. Mursula, and G. A. Kovaltsov (2001), Was one sunspot cycle lost in late XVIII century?, *Astron. Astrophys., 370,* L31-L34, doi:10.1051/0004-6361:20010319.

Vejby-Christensen, L., D. Kella, H. B. Pedersen, and L. H. Anderson (1998), Dissociative recombination of NO^+, *Phys. Rev. A, 57,* 3627.

Warren, H. P., J. T. Mariska, and J. Lean (2001), A new model of solar EUV irradiance variability 1. Model formulation, *J. Geophys. Res.*, *106(A8)*, 15745-15757.

Webber, W. R., and P. R. Higbie (2003), Production of cosmogenic Be nuclei in the Earth's atmosphere by cosmic rays: Its dependence on solar modulation and the interstellar cosmic ray spectrum, *J. Geophys. Res.*, *108(A9)*, 1355, doi:10.1029/2003JA009863.

Wennberg, P. O., J. G. Anderson, and D. K. Weisenstein (1994), Kinetics of reactions of ground state nitrogen atoms ($^4S_{3/2}$) with NO and NO_2, *J. Geophys. Res.*, *99(D9)*, 18839-18846.

White, O. R., A. Skumanich, J. Lean, W. C. Livingston, and S. L. Keil (1992), The Sun in a non-cycling state, *Publ. Astron. Soc. Pac., 104,* 1139-1143.

Wittmann, A. D., and Z. T. Xu (1987), A catalogue of sunspot observations from 165 BC to AD 1684, *Astron. Astrophys. Supp. Ser., 70,* 83-94.

Woods, T. N., S. M. Bailey, W. K. Peterson, S. C. Solomon, H. P. Warren, F. G. Eparvier, H. Garcia, C. W. Carlson, and J. P. McFadden (2003), Solar extreme ultraviolet variability of the X-class flare on 21 April 2002 and the terrestrial photoelectron response, *Space Weather, 1*(1), 1001, doi:10.1029/2003SW000010.

Woods, T. N., G. J. Rottman, S. M. Bailey, S. C. Solomon, and J. Worden (1998), Solar extreme ultraviolet irradiance measurements during solar cycle 22, *Solar Phys.*, *177*, 133-146.

Woods, T. N., and G. J. Rottman (2002), Solar ultraviolet variability over time periods of aeronomic interest, in *Atmospheres in the Solar System: Comparative Aeronomy*, edited by M. Medillo et al., pp. 221-233, AGU, Washington, D.C.

Yoshino, K., J. R. Esmond, Y. Sun, W. H. Parkinson, K. Ito, and T. Matsui (1996), Absorption cross section measurements of carbon dioxide in the wavelength region 118.7-175.5 nm and the temperature dependence, *J. Quant. Spectrosc. Radiat. Trans., 55(1)*, 53-60.

CURRICULUM VITAE

Christopher G. Smithtro
(July 2004)

EDUCATION:

B.S. in Physics, Harvey Mudd College, Claremont, California (1991).

Basic Meteorology Program, Florida State University, Tallahassee, Florida (1993).

M.S. in Applied Physics, Air Force Institute of Technology, Wright-Patterson Air Force Base, Ohio (1999).

Ph.D. in Physics, Utah State University, Logan, Utah (expected 2004).

EXPERIENCE:

Weather Officer, 28th Bomb Wing, Ellsworth Air Force Base, South Dakota (1993-1995).

Weather Station Commander, 16th Operational Support Squadron, Hurlburt Field, Florida (1995-1997).

Space Weather Forecaster and Liaison Officer, NOAA Space Environment Center, Boulder, Colorado (1999-2001).

PRESENTATIONS:

Smithtro, C.G., T. Berkey, D. Thompson, J.J. Sojka, and R.W. Schunk (2003), Observation and Modeling of Ionospheric Dynamics During Major Solar Flares, *Eos Trans. AGU, 84*(46), Fall Meet. Suppl., Abstract SA22B-07.

Smithtro, C.G., J.J. Sojka, J. Lean, and R.W. Schunk (2002), Ionospheric Sensitivity to Different Representations of EUV Spectra, *Eos Trans. AGU, 83*(47), Fall Meet. Suppl., Abstract SH21B-05.